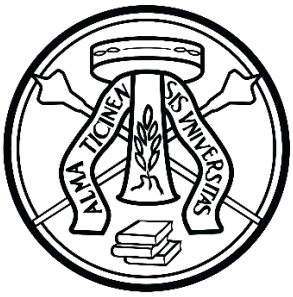

UNIVERSITÀ
DI PAVIA

DIPARTIMENTO DI SCIENZE DEL FARMACO

Direttore Chiar.ma Prof.ssa Simona Collina

LAUREA MAGISTRALE A CICLO UNICO IN FARMACIA

Evaluating the functional efficacy of the plant-derived extract A1 against Triple-Negative Breast Cancer aggressiveness.

Valutazione dell'efficacia funzionale dell'estratto vegetale A1 contro l'aggressività l'aggressività del TNBC.

Relatore: *Prof.ssa Erica Buoso*

Correlatore: *Prof. Marco Racchi*

Tesi di Laurea Magistrale a Ciclo Unico di
Veronica Giugnetti

Anno Accademico 2025/2026

Index

1. ABSTRACT

Triple-negative breast cancer (TNBC) is the most aggressive breast cancer subtype, accounting for 15-25% of all breast cancer cases. It is characterised by marked molecular heterogeneity, high metastatic potential, and the absence of effective targeted therapies due to the lack of estrogen receptor (ER), progesterone receptor (PR), and HER2 expression. Tumour progression is sustained by a dynamic bidirectional crosstalk between cancer cells and the tumour microenvironment (TME), while the scaffold protein RACK1 coordinates signalling pathways involved in tumour cell survival, migration, and invasion.

The anti-tumour activity of the plant-derived extract A1 was evaluated in the mesenchymal-like TNBC cell lines MDA-MB-231 and SUM-159PT, using complementary 2D and 3D *in vitro* models. Cell viability was assessed by MTT, CellTiter-Glo® and LIVE/DEAD assays, while wound healing, Transwell migration and Matrigel invasion assays were performed to evaluate migratory and invasive capacities. RACK1 protein expression was analysed by Western blotting. Tumour-immune crosstalk was investigated through Transwell assays measuring THP-1 monocytes recruitment toward tumour conditioned media.

A1 reduced TNBC cell viability in a dose-dependent manner and markedly impaired migration and invasion in both cell lines. These effects were associated with a significant downregulation of RACK1 expression. Moreover, conditioned media from A1-treated TNBC cells significantly reduced THP-1 monocytes recruitment, suggesting that A1 impairs tumour-derived paracrine signalling involved in TME communication. In 3D spheroids models, A1 effectively suppressed spheroids viability and markedly inhibited invasive outgrowth and branching structures, confirming its anti-invasive activity in a more physiologically relevant setting.

These findings demonstrate that A1 simultaneously targets multiple hallmarks of TNBC progression by reducing tumour cells survival, invasion, and TME crosstalk. The associated downregulation of RACK1 further supports its potential role as a molecular mediator of A1 activity. Overall, A1 emerges as a promising candidate for the development of novel adjuvant therapeutic strategies against TNBC, warranting further mechanistic studies and *in vivo* validation.

SOMMARIO

Il carcinoma mammario triplo-negativo (TNBC) rappresenta il sottotipo più aggressivo di carcinoma mammario, costituendo il 15-25% di tutti i casi di tumore al seno. È caratterizzato da una marcata eterogeneità molecolare, un elevato potenziale metastatico e dall'assenza di terapie mirate efficaci, a causa della mancata espressione del recettore per gli estrogeni (ER), del recettore per il progesterone (PR) e di HER2. La progressione tumorale è sostenuta da un dinamico crosstalk bidirezionale tra le cellule tumorali e il microambiente tumorale (TME), mentre la proteina scaffold RACK1 coordina diversi pathway di segnalazione coinvolti nella sopravvivenza, migrazione e invasione delle cellule tumorali.

L'attività antitumorale dell'estratto vegetale A1 è stata valutata nelle linee cellulari di TNBC a fenotipo mesenchimale MDA-MB-231 e SUM-159PT, utilizzando modelli *in vitro* 2D e 3D complementari. La vitalità cellulare è stata valutata mediante saggi MTT, CellTiter-Glo® e LIVE/DEAD, mentre i saggi di wound healing, migrazione in Transwell e invasione con Matrigel sono stati impiegati per valutare la capacità migratoria e invasiva. L'espressione della proteina RACK1 è stata analizzata mediante Western blot. La comunicazione tra tumore e sistema immunitario è stata indagata attraverso saggi Transwell per valutare il reclutamento di monociti THP-1 verso il terreno condizionato tumorale.

A1 ha dimostrato di ridurre la vitalità delle cellule TNBC in maniera dose-dipendente e ha marcatamente compromesso migrazione e invasione in entrambe le linee cellulari. Questi effetti sono stati associati ad una significativa downregulation dell'espressione di RACK1. Inoltre, il terreno condizionato proveniente da cellule di TNBC trattate con A1 ha ridotto in maniera significativa il reclutamento dei monociti THP-1, suggerendo che A1 alteri la segnalazione paracrina tumore-derivata

coinvolta nella comunicazione con il TME. Nei modelli di sferoidi 3D, A1 ha efficacemente soppresso la vitalità degli sferoidi e ha marcatamente inibito l'invasività e la formazione di strutture ramificate, confermando la sua attività anti-invasiva in un contesto più fisiologicamente rilevante.

Questi risultati dimostrano che A1 agisce simultaneamente su molteplici hallmark della progressione del TNBC, riducendo la sopravvivenza, l'invasione e il crosstalk con il TME delle cellule tumorali. La concomitante downregulation di RACK1 supporta ulteriormente il suo possibile ruolo come mediatore molecolare dell'attività di A1. Nel complesso, A1 emerge come un candidato promettente per lo sviluppo di nuove strategie terapeutiche adiuvanti contro il TNBC, meritando ulteriori studi meccanicistici e di validazione *in vivo*.

2. INTRODUCTION

2.1. Breast cancer

2.1.1. Epidemiology of breast cancer

Breast cancer (BC) is a heterogeneous disease with variable morphologic features, prognosis, and response to therapy. In females, BC is the most prevalent malignancy worldwide and has the greatest rates of cancer-related death (*Nascimento et al., 2020*). According to GLOBOCAN data, 2.3 million new cases and 670.000 deaths from BC occurred globally in 2022, representing 25% of new cases and 15.5% of BC-related deaths among women, which are expected to undergo an increase of respectively 38% and 68% within 2050 (*Kim et al., 2025*). Additionally, the highest incidence of BC is observed in women aged 50 to 69, with no difference between low-income, resource-limited nations, and high-income, developed ones, such as Canada, USA and some European nations (*Obeagu et al., 2024*).

2.1.2. Stratification of breast cancer

Advancements in oncology have led to the creation of diverse stratification systems designed to map the intricate drivers of breast malignancy. These systems aim to categorize tumours more precisely, thereby optimizing clinical trial designs and tailoring therapeutic interventions to individual patient needs (*Taherian-Fard et al., 2014*).

BC can involve every cell of the mammary gland and develop into different histopathological and morphological subtypes, which are characterized by different treatment strategies. Based on the histological patterns, namely origin, cellular morphology, and invasiveness, the tumour is classified into non-invasive forms, where malignant cells remain

restricted to the epithelial structures of the breast (carcinoma *in situ*), and invasive forms. In the latter, uncontrolled growth of cancerous cells enables them to breach the ductal boundaries and extend into the surrounding stromal tissue. Both *in situ* and invasive tumours are further divided into ductal or lobular types, depending on their site of origin within the breast. Ductal carcinoma *in situ* (DCIS) coincides with the malignant transformation of the epithelial cells within the milk ducts, which do not invade the surrounding stroma. The disease progresses to invasive ductal carcinoma (IDC) when the cells penetrate the tissue. More atypical is the lobular carcinoma *in situ* (LCIS), a malignancy arising within the lobules (collections of milk-producing glands), which can evolve into invasive or infiltrating lobular carcinoma (ILC) when the cancerous cells penetrate the lymphatic system and distant organs. Beyond these types, inflammatory BC (IBC) is characterized by the systemic involvement of the mammary lymphatic system and overlying skin, while metastatic BC (MBC) occurs when the disease spreads beyond the primary site to distant organs, most commonly lungs, liver, bones, and brain. It is important to highlight that almost 90% of cancer-related deaths are caused by the ability of the tumour to colonize distant organs and produce metastasis (**Figure 1**) (*Sarvari et al., 2022*).

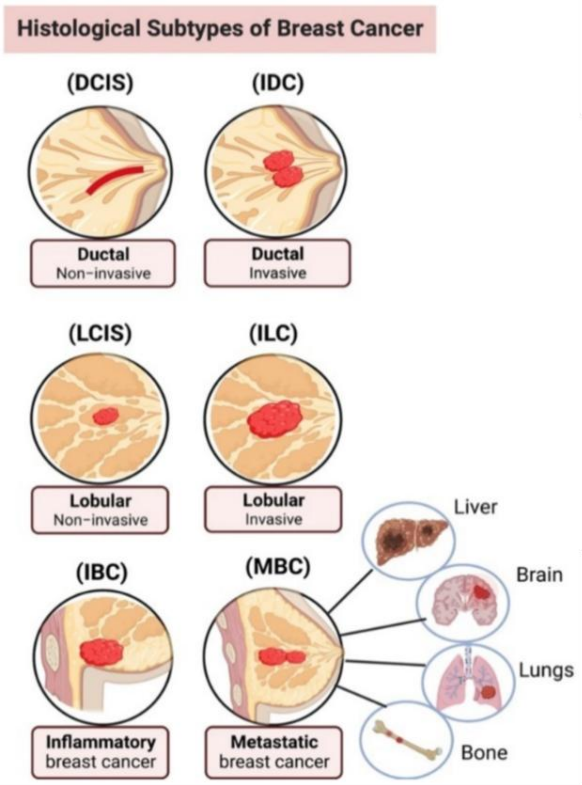

Figure 1. *Overview of BC subtypes based on histological features (Sarvari et al., 2022).*

It has been demonstrated that morphological characteristics and clinicopathological patterns are insufficient to predict the actual course of the disease. Improvement of prediction of an individual's response to therapy is, therefore, carried out studying molecular targets, which are functionally involved in some aspects of the malignancy. The identification of such markers enables a further classification of BC into Luminal A, Luminal B, HER2-enriched, Normal-like, Basal-like, and Claudin-low (*Guido et al., 2020*). The genes are responsible for the expression of estrogen receptor (ER), progesterone receptor (PR), HER2 (Human epidermal growth factor receptor 2), and cell proliferation regulator (Ki-67) (*Nascimento et al., 2020*).

Accounting for 40% of BC cases, Luminal A carcinomas are defined by ER/PR positivity, a lack of HER2 expression, and low levels of Ki-67.

Due to their low-grade nature and low expression of proliferation-related genes, these tumours typically offer the most favourable prognosis, with minimal relapse rates and maximal overall survival (OS) rates. Despite this, they are characterized by a vast landscape of genetic mutations, most notably involving PIK3CA (*Guido et al., 2020*). Luminal B tumours represent 25% of all BC diagnoses, and it can be further categorized into Luminal B (HER2-): ER+, PR-, HER2- and high levels of Ki-67, and Luminal B (HER2+): ER+, HER2+ and any levels of PR, and Ki-67 (*Nascimento et al., 2022*). From a genomic perspective, the mutational landscape shifts in this subtype: while PIK3CA mutations are less prevalent, there is a marked increase in TP53. However, Luminal B subtype is not only more proliferative but also carries a greater propensity for distant metastasis, in particular to bone, liver, and lungs (*Guido et al., 2020*).

Human Epidermal Growth Factor Receptor 2 (HER2) serves as a critical regulator of cellular growth, proliferation, and differentiation (*Guido et al., 2020*). 15% to 20% of newly diagnosed BC cases are represented by HER2-enriched subtype, with a genetic profile defined as: ER-, PR-, HER2+, and high levels of Ki-67 (*Nascimento et al., 2022*). This malignancy arises from the overexpression of HER2, resulting in more aggressive disease progression, greater likelihood of metastasis, and poorer survival outcomes (*Guido et al., 2020*).

Although the Normal-like subtype mimics the biomarker expression of Luminal A (specifically the ER+/PR+/HER2- phenotype with low Ki-67 levels), it represents a distinct clinical entity. In fact, data suggest a prognostic discrepancy between the two, where Normal-like tumours often exhibit slightly less favourable outcomes compared to the superior survival rates typical of the Luminal A subtype (*Sarvari et al., 2022*).

Basal-like BCs, which account for 10-20% of all cases, are characterized by the lack of ER, PR, and HER2 expression, and of their associated genetic signatures, resulting in a substantial overlap with Triple-negative BC (TNBC). However, it is important to note that "Basal-like" and "Triple-negative" are not strictly synonymous, as the two classifications do not always perfectly coincide; indeed, only 70-80% of TNBC cases are categorized as basal-like BCs (*Dass et al., 2021*). Various studies highlight that the basal phenotype is marked by a significantly accelerated metastatic onset and a shortened metastasis-free interval compared to non-basal cohorts, thus predicting an aggressive clinical course and poor prognostic indices. In this particular case, liver, brain and lung metastasis are related to a poorer prognosis, while bone and superficial nodes metastasis align with a better survival rate (*Luck et al., 2008*). At the molecular level, the genomic profile of Basal-like BC frequently reveals TP53 mutations, resulting in the loss of p53-mediated tumour suppression, alongside significant upregulation of the PI3K/Akt signalling pathway (*Guido et al., 2020*).

Lastly, Claudin-low BC is characterized by the absence of ER, PR, and HER2 expression, and can thus be categorized within TNBC. This subtype, however, is distinguished by low E-cadherin expression, as well as low expression of mucin-1, epithelial cell adhesion molecule (EpCAM), and claudins, in addition to minimal expression of proliferation-associated genes such as Ki-67 and luminal markers. On the other hand, these tumours are highly enriched in epithelial-mesenchymal transition (EMT)-associated genes, such as VIM and ZEB1. Moreover, they display an elevated expression of markers associated with immune cell infiltration (including CD14 and CD79b) and stem cell-like features, alongside a characteristic downregulation of tight junction proteins (*Dass et al., 2021*).

A summary of the histopathological and molecular classification of BC is provided in **Figure 2**.

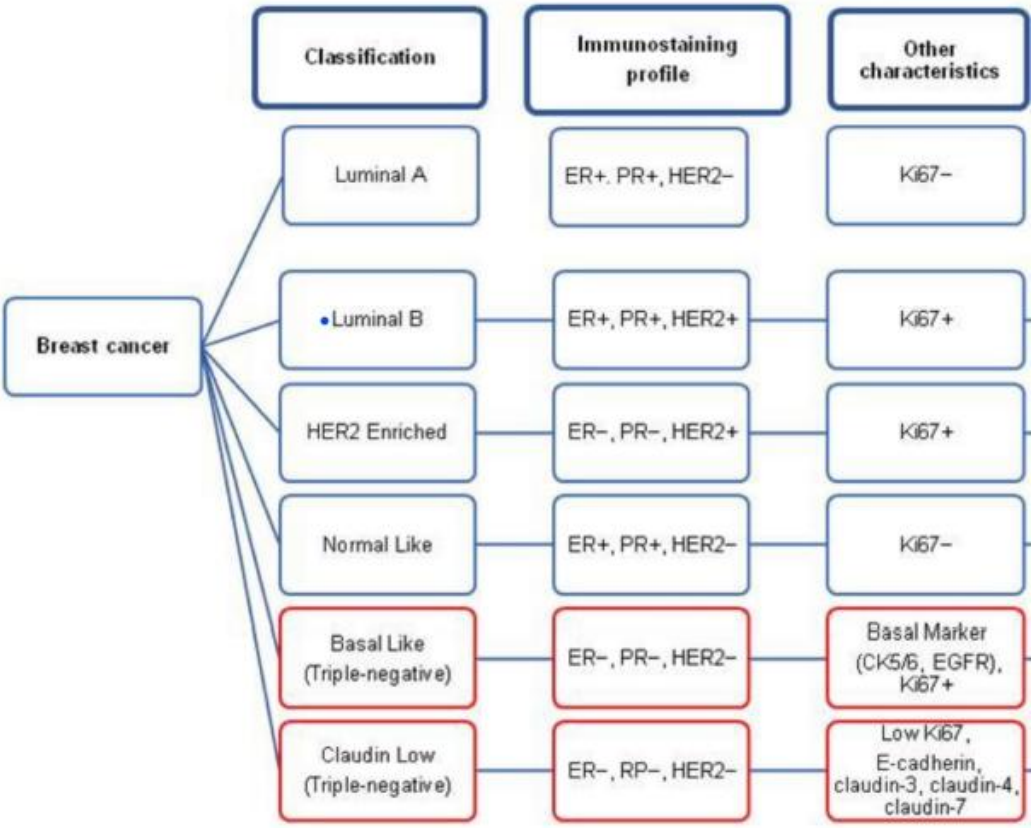

Figure 2. *Classification of BC into intrinsic molecular subtypes based on receptor expression and key biological features (Dass et al., 2021).*

Since 2018, the clinical staging of both DCIS and invasive carcinoma has been defined according to the TNM staging system, as revised in the 8th edition of the American Joint Committee on Cancer (AJCC) guidelines. This scheme categorizes BC based on the dimensions of the primary tumour (T0-T4), the extent of regional lymph node involvement (N0-N3), and the presence of distant metastases (M0-M1). These parameters are further synthesized to assign a global stage ranging from 0 to IV (**Figure 3**). Alongside TNM staging, histological grading further characterizes tumour aggressiveness (G1-G4) based on decrescent cellular differentiation, providing additional prognostic information (*Taherian-*

Fard et al., 2014). These staging methods are foundational tools for clinical assessment to establish a direct correlation between the physical progression of the disease and long-term survival outcomes, and to tailor therapeutic interventions to the specific needs of the patient (*Teichgraeber et al., 2021*).

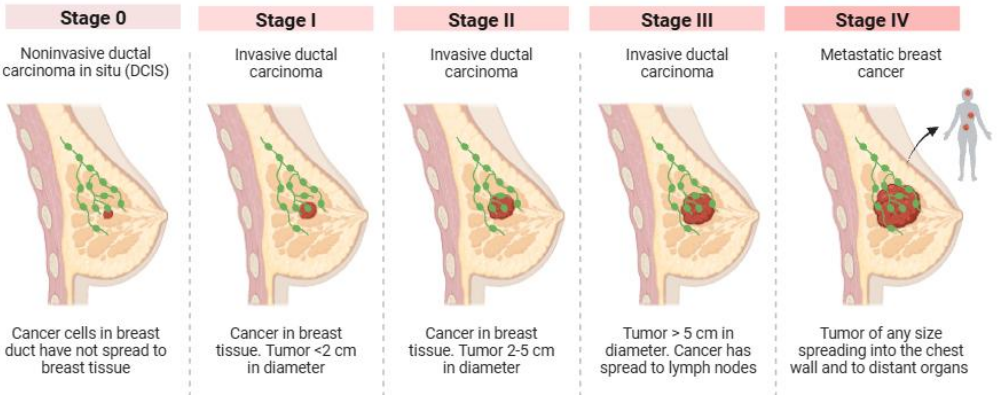

Figure 3. *Visual representation of TNM staging of BC (adapted from BioRender.com).*

2.1.3. Hallmarks and risk determinants of breast cancer

BC is defined by a distinct set of hallmarks, summarized in **Figure 4**, including chronic proliferative signalling, the evasion of growth suppressors, and resistance to programmed cell death (apoptosis). The malignancy is further driven by genomic instability, metabolic dysregulation, and the ability to bypass immune detection while inducing angiogenesis and tissue invasion. Central to this progression is the role of epigenetic alterations, which are foundational drivers that confer oncogenic properties across the entire spectrum of cancer hallmarks, influencing everything from metabolic reprogramming to inflammatory signalling (*Sarvari et al., 2022*).

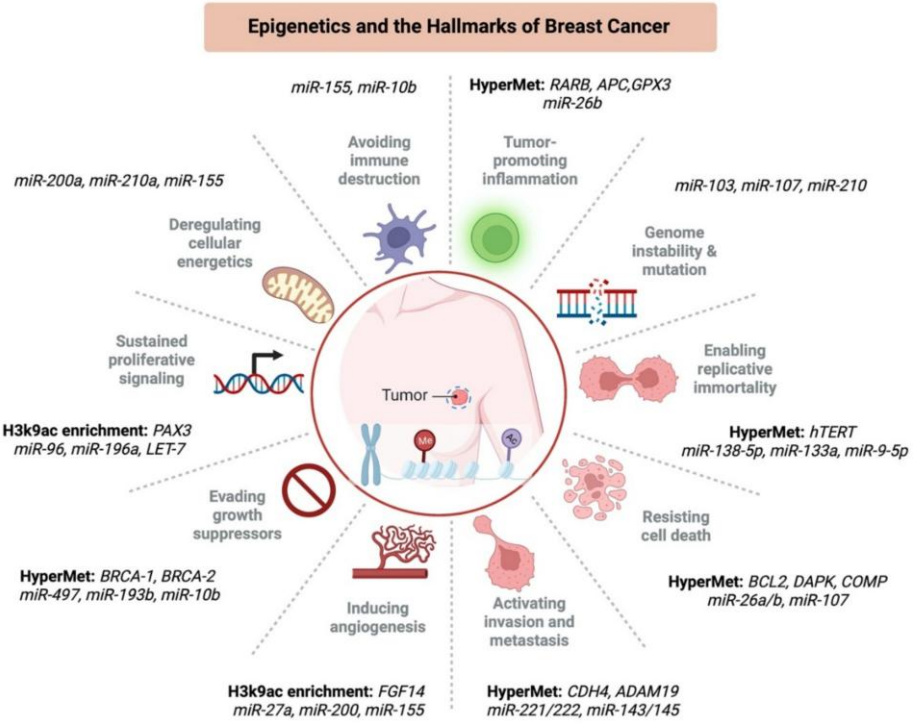

Figure 4. *Schematic overview of the major hallmarks of BC and their defining characteristics (Sarvari et al., 2022).*

BC is the result of various internal and external factors, which include genetic, environmental, and behavioural components. The comprehension of these risk factors is essential for the early detection of the malignancy, which is associated with a better prognosis. The individual's genetic predisposition to BC reflects a combination of personal and family history, which both lead to a higher likelihood to develop the disease. In addition, BRCA gene mutations further increase the risk, as BRCA1 and BRCA2 function as tumour suppressors; consequently, their alteration results in a loss of cancer regulation. However, only 5-10% of BC cases can be attributed to genetic mutations and family or personal history, and roughly 1 in 500 people overall experience BRCA mutations. Crucial for the development of BC is the personal exposure to both endogenous (e.g. hormonal replacement therapy – HRT) and exogenous estrogen (e.g. late menopause), which is known to stimulate breast cells proliferation,

thereby increasing the likelihood of malignant transformation. Additional risk factors worth mentioning include large breasts, which are denser and contain more milk ducts, glands and connective tissue that may be implicated in cancer, as well as overweight and obesity, which are characterized by increased estrogen production. In order to prevent and reduce the risk of BC, a healthy lifestyle – including a balanced diet and regular exercise, along with limiting alcohol consumption and smoking – as well as undergoing regular mammograms and screenings, is recommended (*Obeagu et al., 2024*).

2.2. Triple-negative breast cancer (TNBC)

Triple-negative BC (TNBC) stands out as the most aggressive and heterogeneous subtype of BC, representing 10-20% of new early diagnoses (*Nedeljković et al., 2019*). It disproportionately affects a younger demographic, specifically women under 40, and exhibits a notably higher incidence among African women (27% of diagnoses, *Dogan et al., 2012*). Moreover, TNBC is characterized by a poor differentiation, a high proliferative rate, high incidence of distant metastasis, mainly to the lung and the brain, and a poor OS (*Nedeljković et al., 2019*). In particular, the prognosis for TNBC remains particularly severe: within five years from the initial diagnosis, the mortality rate reaches 40%, reflecting a significantly shorter survival window compared to other subtypes. Furthermore, the clinical course is often characterized by high recurrence levels (affecting 25% of surgical patients) and a strong propensity for systemic spread. Indeed, nearly half of the patients develop distant metastases, after which median survival is typically restricted to just 13 months. Moreover, TNBC cases exhibit an earlier onset of relapse compared to non-TNBC cases, generally occurring within 19 to 40 months. Once a recurrence is identified, the prognosis becomes

exceptionally critical, with a 75% mortality rate observed just three months after the event (*Yin et al., 2020*).

2.2.1. TNBC classification

Characterizing the distinct molecular profiles and specific driver mutations – including oncogenes and tumour suppressors – within each subtype offers vital insights into the heterogeneous nature of TNBC, ultimately guiding the design of personalized therapeutic strategies. In fact, evidences suggest that TNBC cases are characterized by distinct response profiles when subjected to traditional neoadjuvant chemotherapy.

Based on the histological patterns, TNBC is classified into invasive ductal carcinoma of no special type (90%) and special histological types (10%), which include metaplastic, medullary, invasive lobular, apocrine, and adenoid cystic carcinoma (*Zhao et al., 2020*). From the genetic perspective, TNBC commonly shows mutations of the TP53 gene and the suppression of the BRCA1 gene, which results in an aggressive tumour biology and a poor prognosis. Hence, a low prevalence of DCIS is typically observed, consistent with a model of rapid tumour development that bypasses the *in-situ* stage (*Dogan et al., 2012*). However, the histological features are insufficient to establish an efficient treatment strategy (*Zhao et al., 2020*).

TNBC genetic profile allows the stratification of the disease into six distinct subtypes (**Figure 5**): basal-like 1 (BL-1), basal-like 2 (BL-2), mesenchymal (M), mesenchymal stem-like (MSL), immunomodulatory (IM), and luminal androgen receptor (LAR). This classification is the key for the identification and establishment of personalized and targeted treatment options for every TNBC individual (*Dass et al., 2021*).

BL-1 and BL-2 subtypes exhibit closely related gene expression profiles associated with cell division as well as cell cycle advancement. In particular, BL-1 cases share an abnormal expression of genes related to cell cycle and DNA-repair regulation (high amplification of PIK3CA and deletion of BRCA2, PTEN, TP53). BL2 subtype, instead, is characterized by an abnormal activation of growth factor signalling pathways, such as Wnt/β-catenin and EGFR (*Yin et al., 2020*).

M and MSL subtypes, instead, are characterized by an elevated expression of genes associated with extracellular receptor interaction, cell motility and cell differentiation pathways. In particular, the M subtype is characterized by the upregulation of several crucial signalling pathways, including those governing cell motility (actin-regulated) and extracellular matrix interactions. Additionally, it exhibits significant activation of differentiation pathways, such as Wnt, and TGF-β. Due to these unique features, this subtype is frequently identified as metaplastic BC. Conversely, the MSL subtype shows a low expression of proliferation-related genes, while high levels of stemness-related genes and angiogenesis-related receptors PDGFR and VEGFR are detected.

The elevated expression of immune cell-associated genes and signal transduction pathways sets the IM subtype apart from the rest, closely resembling medullary carcinoma. Specifically, the Th1/Th2, NK cell, B-cell receptor, and T-cell receptor signalling pathways are consistently upregulated in this subgroup, reflecting the dense infiltration of immune cells (TILs – Tumour Infiltrating Lymphocytes) within the tumour microenvironment (TME).

Lastly, the LAR subtype is significantly distinct from other TNBC subtypes; in fact, despite the absence of ER, this subgroup exhibits high expression of hormone-related signalling pathways, including steroid synthesis and androgen/estrogen metabolism. In this case, the mutational

landscape is characterized by frequent mutations in PIK3CA, PTEN and TP53 genes, which are under investigation as candidate therapeutic targets (*Yin et al., 2020*).

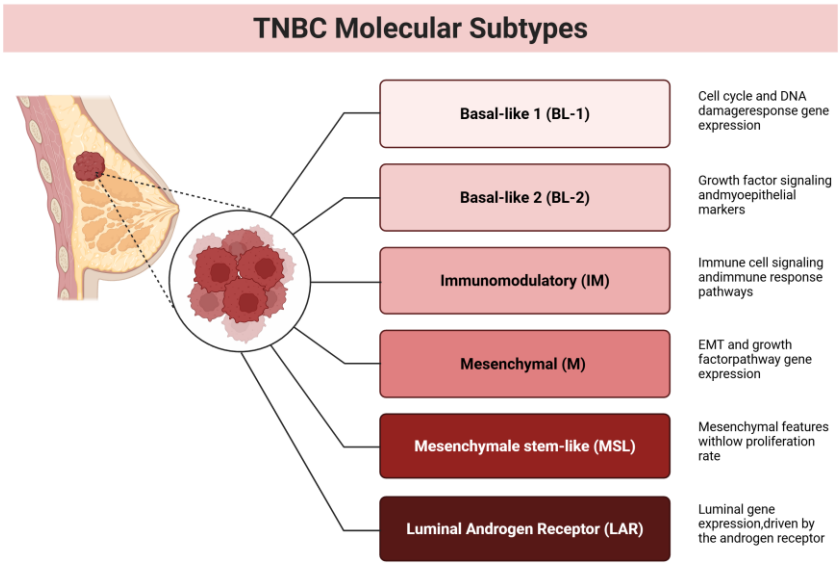

Figure 5. *Schematic representation of the original molecular classification of TNBC by Lehman et al., 2011 (created with BioRender.com).*

2.2.2. TNBC treatment strategies

The currently available treatment options for TNBC – chemotherapy, surgery, and radiotherapy – expose patients to considerable side effects, high resistance rates, and frequent recurrence (*Emara et al., 2025*). Standard regimens are typically based on anthracyclines and taxanes, though anthracycline-free protocols may be preferred in lower-risk patients or where cardiotoxicity is a concern. Bisphosphonates are additionally recommended for operable BC patients with low estrogen levels, particularly those at higher risk of relapse or therapy-induced bone loss (*Pinilla et al., 2022*). Although approximately 20% of patients achieve a pathologic complete response (pCR) following neoadjuvant

chemotherapy, OS in TNBC remains significantly lower than in non-TNBC cases (*Nedeljković et al., 2019*).

Recent clinical efforts have focused on targeting specific kinases, including non-RTKs (non-receptor tyrosine kinases) such as mTOR, PI3K, and AKT, and RTKs such as EGFR and VEGFR (*Emara et al., 2025*), with individual gene aberrations grouped according to relevant signalling pathways including PDGF/VEGF, PI3K/AkT/mTOR, and JAK/STAT3. Among these, the PI3K/AkT/mTOR pathway stands out as one of the most promising therapeutic targets, being commonly upregulated across TNBC subtypes. Clinical evidence indicates that adding the AKT inhibitor ipatasertib to paclitaxel extends OS from 16.2 to 23.1 months and progression-free survival (PFS) from 4.9 to 9 months, while capivasertib shifts median PFS from 3.7 to 9.3 months in biomarker-positive patients. Regarding EGFR, the integration of panitumumab into anthracycline/taxane regimens increased pCR rates by over 25%, and a comparable improvement was observed with the anti-VEGF antibody bevacizumab, although the latter failed to provide an OS benefit and was associated with a higher incidence of severe adverse events. In contrast, results for JAK/STAT3 and MEK inhibitors have been largely disappointing in clinical settings, despite promising preclinical activity. More encouraging outcomes have been achieved by incorporating immunotherapy – particularly agents targeting PD-1 and PD-L1 – into neoadjuvant regimens (*Zhao et al., 2020*), a topic explored in greater detail in the following sections. Finally, natural compounds such as curcumin have also shown broad inhibitory activity against tumour progression, acting simultaneously on RTK activation, expression, and ligand production, as well as on downstream non-RTK signalling cascades (*Emara et al., 2025*). **Table 1** provides an overview of the novel targeted

agents currently being explored for each TNBC subtype, based on the characterizing genetic alterations.

TNBC subtype	Molecular and genetic featuers	Therapeutic strategies	Treatment options
BL1	Abnormal expression of cell cycle and DNA-repair regulation genes	↓ Cell proliferation ↓ DNA damage response	**Mitosis inhibitors** (Paclitaxel, Docetaxel, Nab-Paclitaxel) **Cytostatics** (Carboplatin, Cisplatin) **PARP inhibitors** (Olaparib) **DNA synthetic inhibitors** (Doxorubicin)
BL2	Abnormal activation of signalling pathways	↓ TP63 ↓ EGFR ↓ MET	**Cytostatics** (Carboplatin, Cisplatin) **PARP inhibitors** (Olaparib) **Growth Factor inhibitors** (Bevacizumab, Trastuzumab) **mTOR inhibitors** (Rapamycin)
IM	Elevated expression of immune cell-associated genes and signal transduction pathways	↓ Immune signalling	**Cytostatic** (Carboplatin, Cisplatin) **PARP inhibitors** (Olaparib) **Immune checkpoints inhibitors** (Ipilimumab)
M	Upregulation of cell motility pathways (actin-regulated) and extracellular matrix interactions	↓ EMT ↓ Wnt ↓ PI3K ↓ mTOR ↓ Scr ↓ TGFβ ↓ IGF1R ↓ Notch	**Growth Factor inhibitors** (Bevacizumab, Trastuzumab) **mTOR inhibitors** (Rapamycin) **PI3K inhibitors** (Idelasilib) **Scr inhibitors** (Dasatinib)
MSL	Low expression of proliferation-related genes, high levels of stemness-related genes, overexpression of angiogenesis-related receptors PDGFR and VEGFR	↓ EMT ↓ Wnt ↓ MAPK ↓ Rac ↓ PI3K ↓ mTOR ↓ Scr ↓ PDGF	**Growth Factor inhibitors** (Bevacizumab, Trastuzumab) **mTOR inhibitors** (Rapamycin) **PI3K inhibitors** (Idelasilib) **MAPK inhibitors** (Trametinib) **Scr inhibitors** (Dasatinib)
LAR	High expression of hormone-related signalling pathways, steroid synthesis and androgen/estrogen metabolism	↓ AR signalling ↓ FOXA1 ↓ ERBB4	**Nonsteroidal antiandrogens** (Bicalutamide) **mTOR inhibitors** (Rapamycin) **PI3K inhibitors** (Idealisib)

Table 1. *Comprehensive overview of therapeutic approaches and their corresponding molecular targets according to BC subtype (created with Canva.com).*

Despite these advances, approximately one-third of early-stage patients show limited response to initial treatment and experience poor long-term outcomes. TNBC cells tend to develop alternative molecular pathways that render RTK and non-RTK inhibitors largely ineffective as monotherapies, underscoring both the insufficiency of currently available options and the urgent need for subtype-specific biomarker identification and personalized therapeutic strategies (*Pinilla et al., 2022; Emara et al., 2025*).

2.3. Tumour microenvironment (TME)

As previously described, the clinical management of TNBC remains a significant challenge due to its resistance to conventional cytotoxic therapies. This has shifted therapeutic interest toward the stromal compartment, particularly focusing on the role of the innate immune system within the TME (*Steenbrugge et al., 2018*). In fact, growing evidence suggests that BC onset and progression are closely linked to inflammatory processes, which drive the recruitment of both innate and adaptive immune cells – including B cells, T cells, eosinophils, and macrophages – into malignant tissue (*Stewart et al., 2012*). This diverse cellular landscape further allows for the categorization of BC into three distinct spatial patterns: "cold" tumours which lack an immune infiltrate, "hot" tumours where immune and malignant cells are integrated, and "compartmentalized" tumours where the immune population remains spatially sequestered from the cancerous tissue (*Zhao et al., 2020*). However, the immune landscape of TNBC is far from uniform. Based on immunogenomic profiling of 386 TNBC patients, Xiao and colleagues (2019) identified three distinct microenvironment phenotypes: the "immune-desert" cluster, characterized by low immune cell infiltration; the "innate immune-inactivated" cluster, dominated by resting innate immune cells and non-immune stromal cells; and the "immune-inflamed"

cluster, defined by abundant adaptive and innate immune cell infiltration. Whereas the latter is regarded as a "hot tumour" phenotype, the first two are collectively classified as "cold tumours" (*Xiao et al., 2019*). Thus, rather than being uniformly hot or cold, TNBC encompasses a spectrum of immune phenotypes, a distinction with direct implications for the design of immunotherapeutic strategies (*Zhu et al., 2021*).

The TME is a multifaceted network composed of immune cells, cancer-associated fibroblasts, cytokines, blood vessels, and other stromal components, which collectively orchestrate conditions that favour tumour initiation, progression, immune evasion, and treatment response (*Zhang et al., 2025*). Among the diverse immune populations residing within the TME, tumour-associated macrophages (TAMs) represent the predominant infiltrating immune cell type and have been closely associated with poor prognosis and drug resistance in BC. TAMs largely originate from bone marrow-derived monocytes that are recruited to the TME through inflammatory cytokines secreted by cancer cells, where they differentiate into macrophages under the influence of colony-stimulating factor 1 (CSF-1) (*Wang et al., 2021*). Macrophages are now recognized as highly plastic cells involved in a broader range of functions, including clearance of senescent cells, tissue remodelling, wound healing, promotion of cell proliferation and angiogenesis, and immunosuppression (*Espinoza-Sánchez et al., 2017*). Moreover, high CD68 expression – a marker of macrophage infiltration – was significantly associated with reduced recurrence-free survival, higher tumour grade, and lymph node involvement, confirming macrophages as an independent indicator of disease aggressiveness (*Ward et al., 2015*). Consistent with this expanded understanding, several BC studies demonstrated that preventing immune cells recruitment to the tumour site results in reduced tumour size and decreased metastatic dissemination (*Espinoza-Sánchez et al., 2017*).

In the context of oncogenesis, TAMs are generally categorized into two divergent phenotypes: classically activated (M1) and alternatively activated (M2) macrophages. M1 macrophages mediate potent anti-tumour responses through robust phagocytic activity and the secretion of pro-inflammatory cytokines, including TNF-β, IL-1α, and IL-1β. Typically stimulated by lipopolysaccharides (LPS) and IFN-γ and phenotypically identified by CD80 and CD86 expression, they activate other immune cells and promote immune-mediated tumour destruction *(Zhang et al., 2025*). Conversely, the M2 phenotype – driven by IL-4 and IL-13 – promotes an immunosuppressive and pro-tumourigenic milieu through the expression of CD206 and CD163 and the production of arginase-1, IL-10, and TGF-β (*Xu et al., 2022*) (**Figure 6**). These mediators suppress T cell activity, promote tumour growth and metastasis, reduce drug efficacy, and impair immune surveillance, ultimately enabling tumour cells to evade immune detection (*Zhang et al., 2025*).

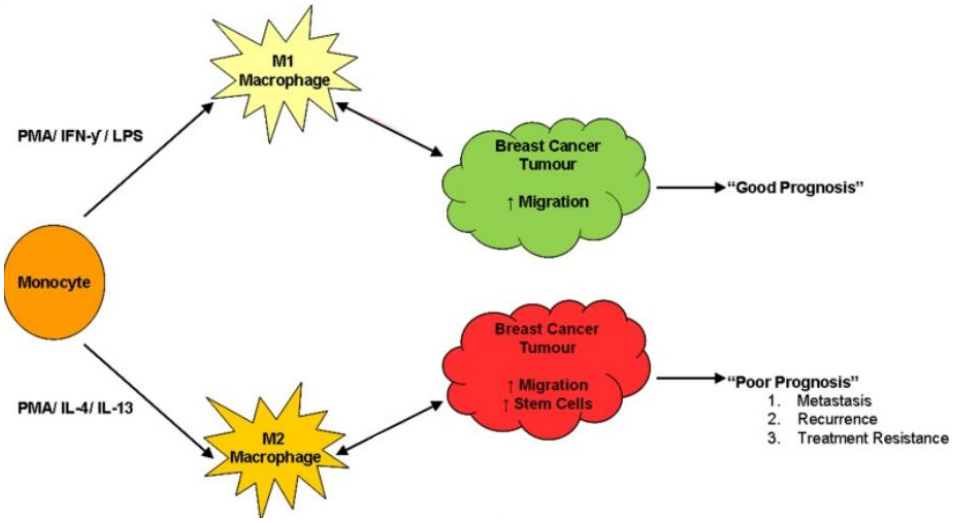

Figure 6. *Schematic diagram distinguishing M1 and M2 macrophage polarization states and their respective functions within the tumour microenvironment (TME) (Ward et al., 2015).*

To exploit this dynamic, tumour cells have developed two main strategies. The first relies on the upregulation of "do not eat me" signals – such as CD47 and CD24 – which engage inhibitory receptors on macrophages and suppress phagocytosis. The second involves the active reprogramming of macrophages toward the M2 phenotype through immunosuppressive cytokines such as IL-10 and CSF-1. In TNBC, this latter mechanism is particularly prominent: TNBC cells display a stronger capacity to induce M2 differentiation compared to non-TNBC cells, and these tumours exhibit greater TAMs infiltration correlating with poorer survival. Notably, the oncogene MCT-1, highly expressed in TNBC, stimulates IL-6 secretion, which in turn drives M2 polarization. Once established, TAMs actively contribute to tumour growth, angiogenesis, invasion, and immune suppression (*Hao et al., 2023*).

The spatial organization of immune cells within the TME adds a further layer of complexity, representing one of the most clinically relevant dimensions of TNBC heterogeneity. Multiple studies confirm that the spatial architecture of the TME – rather than the mere presence of immune cells – ultimately determines the functional outcome of the anti-tumour immune response and the likelihood of benefit from immune checkpoint inhibition. Building on this complexity, the local TME exerts a strong influence on macrophage behaviour, influencing their polarization and functional output in a manner dictated by tumour type, tissue context, and surrounding stromal cells. Within the TNBC microenvironment, cytokine-mediated communication operates through both autocrine and paracrine circuits, often intertwined in self-reinforcing bidirectional loops between neoplastic cells and TAMs (*Valeta-Magara et al., 2019*). Cancer cells autonomously sustain their mesenchymal and stem-like phenotypes through autocrine signalling mediated by IL-8, GRO-α, GRO-β, and IL-1α, while simultaneously shaping macrophage behaviour via paracrine

release of IL-6, M-CSF, and CCL2. Reciprocally, TAM-derived factors such as TGF-β, IL-10, and IL-1β act on TNBC cells in a paracrine manner, promoting EMT, immune evasion, and metastatic dissemination (*Pe et al., 2022*).

Among the soluble mediators driving these circuits, IL-6, IL-8, and IL-1 family members occupy a central position. IL-6 production is markedly elevated in TNBC compared to hormone receptor-positive lines and has been broadly associated with unfavourable prognosis, stemness, and chemoresistance. Its signalling is inherently self-reinforcing: macrophage-derived IL-6 amplifies cytokine release from neighbouring tumour cells, which in turn drives further M2 polarization through STAT3 activation, consolidating a pro-tumorigenic feedforward loop. Interestingly, IL-6 also suppresses CCL22 expression in cancer-conditioned macrophages – a chemokine that would otherwise attract Tregs through CCR4 engagement, thereby limiting anti-tumour immunity (*Pe et al., 2022*). In parallel, IL-8 and GRO chemokines – produced by both cancer cells and activated macrophages – collectively sustain mesenchymal and CSC-like phenotypes via JAK/STAT3 activation, with GRO-α and GRO-β emerging as the most potent inducers of these programmes. M2-polarized macrophages further amplify this axis by secreting elevated levels of IL-8 and GRO chemokines, establishing an IL-8/GRO/STAT3 feedforward loop that operates through both cell-intrinsic hyperactivation and TAM-derived paracrine signals (*Valeta-Magara et al., 2019).* Crosstalk between TNBC cells and macrophages additionally triggers an early ROS elevation within tumour cells, which activates NF-κB and drives upregulation of IL-1α, IL-1β, and IL-8. IL-1α acts as a central node within this network: secreted IL-1α engages IL-1R1 in autocrine and paracrine manners, activating MAPKs/AP-1, NF-κB, PI3K/Akt, and JAK/STAT3 cascades and promoting metastasis through the ERK1/2-ZEB1-VIM pathway,

while NF-κB further amplifies IL-1α, IL-1β, and IL-8 expression in a self-sustaining loop. Hence, these findings delineate a bidirectional crosstalk in which macrophage-induced cytokine upregulation enhances TNBC metastatic potential, while tumour-derived signals reciprocally shape macrophage polarization and infiltration (*Hao et al., 2023; Espinoza-Sánchez et al., 2017*).

A second major axis governing the TNBC-TAM crosstalk converges on CCL2 and STAT3 signalling. TNBC cells constitutively secrete elevated levels of CCL2, CCL5, and G-CSF, driving monocyte recruitment and activation. In the context of tumour dissemination, CCL2 acts as a central orchestrator of a pro-metastatic immune axis. In particular, tumour and stromal cells at the target organ create a chemokine gradient that selectively attracts CCR2-high inflammatory monocytes toward pulmonary metastatic sites, where they facilitate tumour cell extravasation through local VEGF release and subsequent endothelial destabilization, before differentiating into metastasis-associated macrophages that sustain colonization (*Qian et al., 2011*). Upstream, STAT3 directly binds the CCL2 promoter to drive its transcription, and is itself activated by IL-6/STAT3 signalling, which simultaneously polarizes macrophages toward an immunosuppressive M2 phenotype secreting IL-10 and TNF-β. Beyond CCL2 regulation, STAT3 intersects with NF-κB, Akt, and p38 to further amplify tumour-promoting signals, establishing a complex feedforward network in which TAM-derived factors enhance EMT, stemness, and macrophage recruitment, while TNBC cell-derived signals reciprocally shape macrophage behaviour (*Zhang et al., 2025*). To better illustrate this regulatory network, the main pathways governing JAK/STAT3 signalling in the TME are summarized in **Figure 7**.

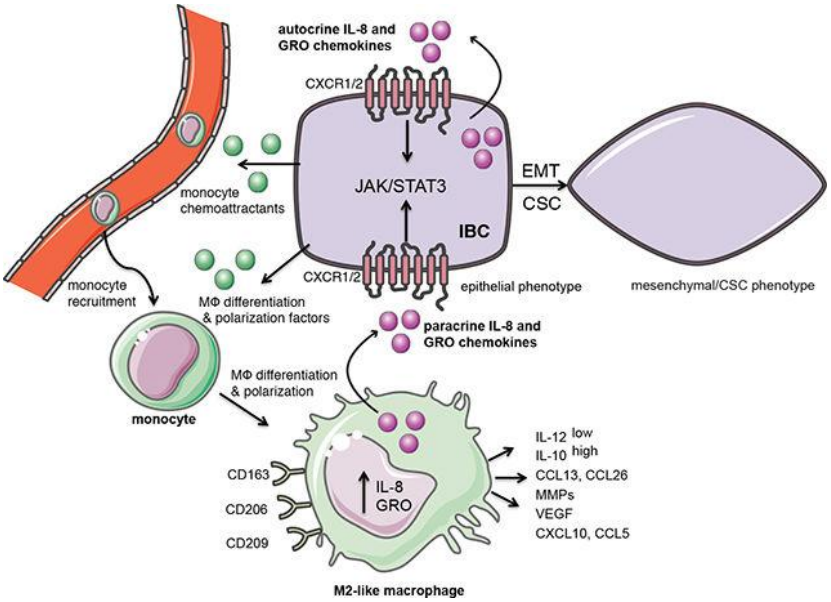

Figure 7. *Schematic representation of JAK/STAT3 pathway regulation in the TME, highlighting the key upstream activators and downstream effectors (Valeta-Magara et al., 2019).*

Finally, within TNBC the infiltration of TAMs is closely linked to the upregulation of HIF-1α under hypoxic conditions, which promotes angiogenesis, immunosuppression, and Treg recruitment within the TME. Targeting HIF-1α in combination with standard chemotherapy is currently being explored as a strategy to improve clinical outcomes in TNBC patients (*Padzińska-Pruszyńska et al., 2024*). Taken together, these observations confirm that cancer aggressiveness is strongly shaped by tumour-stroma communication, with M2-polarized TAMs representing key contributors to the aggressive features and poor prognosis of BC. Given the considerable intra- and inter-tumoral genetic heterogeneity that has limited effective therapeutic strategies, the mechanisms governing this crosstalk may represent a consistent set of prognostic and therapeutic targets for TNBC treatment (*Espinoza-Sánchez et al., 2017*).

2.4. Immunotherapy

The ineffective outcomes associated with standard interventions underscore the urgent necessary of developing new targeted therapies. A major medical breakthrough has been achieved with the introduction of targeted immunotherapy in patients exhibiting programmed cell death ligand 1 (PD-L1) expression (roughly 20% of cases), where combining immune checkpoint inhibitors with chemotherapy has markedly improved prognostic outcomes. The expression of PD-L1 within the TME is subject to complex, reciprocal regulation between neoplastic cells and macrophages, where TAMs undergo functional reprogramming and polarization shifts driven by PD-1/PD-L1 signalling. In TNBC, key inflammatory mediators, including IFN-γ, TGF-β, and prostaglandin E2 (PGE2), trigger different signalling pathways including PI3K/Akt/mTOR cascade, which significantly upregulate PD-L1 expression on the surface of TAMs. Simultaneously, the pharmacological inhibition of PD-L1 via αPD-L1 therapy effectively impairs the polarization of TAMs into the M2 phenotype, while further suppressing the EMT and the acquisition of stemness features in TNBC cells. This multi-level inhibition ultimately results in reduced tumour migration and attenuated angiogenesis. Within this therapeutic landscape, pembrolizumab has emerged as a central agent, and clinical evidence indicates that it significantly improves both pCR and event-free survival (EFS) – by 13.6% and 7.7%, respectively – whether administered as a monotherapy or in combination with standard chemotherapy across early and advanced TNBC stages. Notably, the combination of pembrolizumab with niraparib (a PARP inhibitor) has demonstrated encouraging anti-tumour efficacy in the metastatic TNBC setting, with particular regard for patients carrying BRCA mutations (*Zhao et al., 2020*). Based on these outcomes, both the EMA and FDA have approved pembrolizumab in combination with chemotherapy as a

neoadjuvant regimen, followed by continued adjuvant pembrolizumab for patients with high-risk, early-stage TNBC (*Padzińska-Pruszyńska et al., 2024*). Similarly, the anti-PD-L1 monoclonal antibody atezolizumab, when combined with nab-paclitaxel, demonstrated significant activity, particularly in the subgroup of patients with PD-L1-positive immune cell infiltration (*Zhao et al., 2020*).

Likewise, the inhibition of the CCL2/CCR2 axis can effectively reduce monocyte influx. Clinical interest has focused on agents like carlumab, a human monoclonal antibody designed to deplete TAM populations and decrease post-chemotherapy recurrence. Furthermore, the CSF-1/CSF-1R signalling pathway plays a critical role in the differentiation, migration, and survival of the monocyte-macrophage lineage. In TNBC, where elevated CSF-1 levels correlate with higher histological grades, pharmacological blockade of this pathway offers a valid therapeutic route to suppress TAM-mediated immune evasion. However, CSF-1R targeted therapy with lacnotuzumab in co-administration with carboplatin and gemcitabine did not demonstrated better results than chemotherapy alone.

An alternative and promising therapeutic approach focuses on the direct depletion of TAMs within the TME. In this context, bisphosphonates – most notably clodronate – have demonstrated significant efficacy in reducing tumour progression, angiogenesis, and metastatic spread, by selectively inducing macrophage apoptosis. Similarly, current research is focused on strategies to enhance the phagocytic activity of macrophages. In BC, malignant cells frequently circumvent this immune mechanism by overexpressing anti-phagocytic molecules, such as CD47 protein, which allow them to evade detection by M1 macrophages. The use of anti-CD47 antibodies, particularly when conjugated with chemotherapy, has demonstrated significant efficacy in inhibiting tumour progression and in

restoring the capacity of macrophages to identify and eliminate neoplastic cells.

Another explored therapeutic strategy involves disrupting the signalling pathways that drive M2-like macrophage differentiation. In TNBC, this phenotypic shift can be achieved through the administration of Toll-like receptor (TLR-3 and TLR-7) agonists, which act as potent immunomodulators that promote the repolarization of macrophages toward a pro-inflammatory M1 phenotype, thereby restoring their anti-tumour activity. Furthermore, the induction of the M1 profile can be facilitated by targeting the PI3K/Akt/mTOR axis. The use of specific PI3K inhibitors effectively disrupt this signalling cascade, which is a key driver of M2-associated immunosuppression.

A critical consideration in the development of these therapies is the physiological role of macrophages in maintaining tissue homeostasis. Consequently, the non-selective or uncontrolled depletion of TAMs risks disrupting the broader immune ecosystem, potentially compromising the overall efficacy of the host's immune response. Thus, targeting TAMs as a monotherapy is often insufficient to achieve a robust anti-tumour effect, because neoplastic cells frequently activate compensatory signalling pathways to bypass therapeutic pressure and foster drug resistance. Therefore, a comprehensive understanding of the TME equilibrium is essential to optimize the clinical efficacy of immunotherapies while minimizing off-target toxicity and associated risks (*Padzińska-Pruszyńska et al., 2024*).

2.5. RACK1

RACK1 (Receptor for Activated C Kinase 1) is a 317-amino acid scaffolding protein encoded by the GNB2L1 gene, with an apparent

molecular weight of 36 kDa on SDS-PAGE. It belongs to the WD-repeat protein family, conserved across prokaryotes and eukaryotes, characterized by peptide motifs of 40-60 amino acids terminating with a Tryptophan-Aspartate (WD) dipeptide. These repeats fold into a β-propeller structure that serves as a versatile docking platform for multiple protein complexes. Given the centrality of WD-repeat proteins in signal transduction, structural modifications to this scaffold can destabilize essential regulatory pathways with significant clinical consequences. RACK1's three-dimensional architecture (**Figure 8**) is closely related to that of Gβ subunits, organized as a seven-bladed β-propeller in which each blade consists of a four-stranded antiparallel β-sheet. Multiple binding surfaces arise from this arrangement, enabling RACK1 to engage molecular partners through both constitutive and stimulus-dependent interactions. This structural versatility underlies its primary role as a scaffolding protein involved in cell proliferation, transcription, protein synthesis, and neuronal function. Beyond platform assembly, RACK1 actively shuttles binding partners to specific intracellular compartments and modulates the enzymatic activity of its interactors, either promoting or suppressing their function (*Adams et al., 2011*). Given this functional diversity, RACK1 expression levels carry particular biological and clinical relevance (*Buoso et al., 2017*).

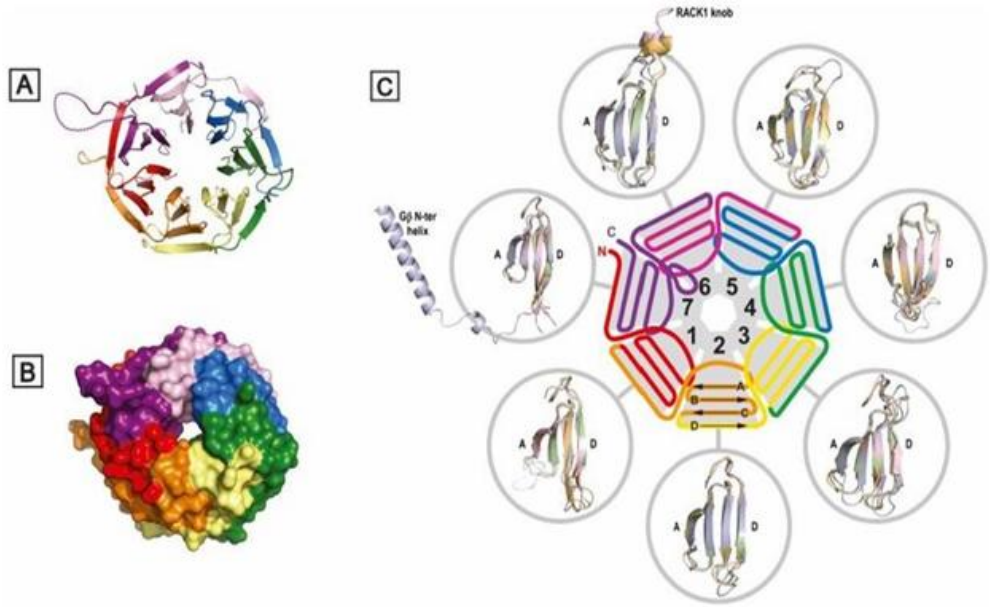

Figure 8. Structure of Human RACK1. *The 317-amino acid sequence is organised to illustrate the seven canonical WD40 repeats (WD1–WD7), each characterised by conserved flanking dipeptide motifs beginning with GH (Glycine-Histidine) and terminating with WD (Tryptophan-Aspartic acid). Individual repeats are colour-coded to reflect their corresponding domains within the established three-dimensional structure of the protein (Adams et al., 2011).*

2.5.1. RACK1 in breast cancer

In oncology, RACK1 expression is dysregulated across multiple cancer types – including pulmonary adenocarcinoma, hepatocellular carcinoma, and metastatic melanoma – promoting proliferation, invasion, and metastasis in breast and prostate cancer models (*Buoso et al., 2017*). In BC specifically, a direct correlation exists between aberrant RACK1 expression and high tumour proliferation rates, supported by its strong positive association with Ki67 and HER-2, the latter aligning RACK1 with more aggressive, high-grade disease phenotypes (*Buoso et al., 2020; Cao et al., 2010*). Large-scale evidence from a systematic review and meta-analysis encompassing 22 studies and over 3,000 patients confirmed that RACK1 overexpression associates with reduced OS, disease-free survival, and recurrence-free survival across multiple malignancies. Critically, high

RACK1 expression was also significantly linked to lymph node involvement – a finding of particular relevance in BC, where lymphatic invasion represents a primary driver of metastatic spread (*Wang et al., 2023*). Stable overexpression of RACK1 in low-invasiveness BC cell lines accelerates proliferation, reduces cell doubling time, and enhances migratory and invasive capacity *in vitro*, while *in vivo* evidence further connects RACK1 to the development of paclitaxel chemoresistance (*Buoso et al., 2020*). Collectively, these findings position RACK1 as an active contributor to BC aggressive behaviour, with potential utility in risk stratification and prognostic assessment.

2.5.2. RACK1 as a signalling scaffold

Beyond its structural roles, RACK1 operates through two functionally distinct but interconnected mechanisms that collectively sustain tumour cell proliferation and invasive capacity. As an integral component of the 40S ribosomal subunit, RACK1 governs cap-dependent mRNA translation by recruiting PKCβII to the translational machinery, enabling the ribosome to respond directly to PKC-Raf-ERK1/2 signals and linking growth factor stimulation to accelerated protein synthesis (*Adams et al., 2011; Buoso et al., 2020*). Outside the ribosome, RACK1 functions as a cytosolic scaffold that assembles multiprotein complexes integrating extracellular stimuli across several oncogenic pathways (**Figure 9**). (*Adams et al., 2011*). Through its constitutive association with PKCβII, RACK1 facilitates proximity-based phosphorylation of downstream substrates including JNK, while its recruitment of PDE4D5 to the FAK complex enables spatially restricted cAMP hydrolysis near focal adhesions, coordinating their turnover during directional migration (*Yarwood et al., 1999*). Critically, RACK1 also suppresses Src-family kinase activity under basal conditions, stabilizing E-cadherin-mediated

intercellular junctions. At the same time, IGF-1-driven dissociation of RACK1 from Src restores kinase activity, triggering downstream PI3K/Akt signalling and the cytoskeletal remodelling associated with the transition to a migratory, mesenchymal phenotype (*Neasta et al., 2016*). These dual roles position RACK1 as a central node linking translational reprogramming, PKC-mediated signalling, and PI3K/Akt-driven invasion – providing the mechanistic rationale for investigating its downstream effectors, including pAkt, vimentin, and E-cadherin, as readouts of RACK1-dependent invasive behaviour in TNBC cells (*Yang et al., 2026*).

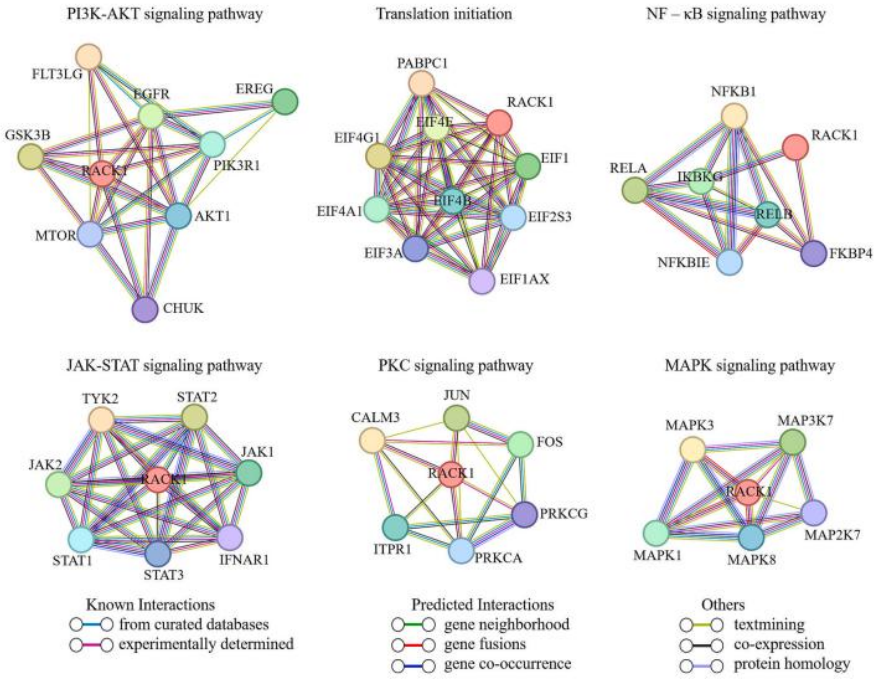

Figure 9. *Schematic representation of RACK1-related core signalling interaction network (Yang et al., 2026).*

2.5.3. RACK1 in migration, focal adhesions and EMT

RACK1 acts as a key integrative scaffold linking extracellular matrix-derived signals with growth factor-mediated pathways to regulate adhesion, migration, and metastatic progression. The pro-migratory capacity of this complex is further amplified through downstream

effectors: RACK1 overexpression significantly increases the pool of active GTP-bound RhoA without altering its total levels, placing the RhoA/Rho kinase pathway as a principal effector of RACK1-mediated motility (*Adams et al., 2011*). Simultaneously, RACK1 engages the PI3K p110α catalytic subunit, activating the PI3K/Akt/Rac1 axis, enhancing FAK phosphorylation, and triggering downstream cascades critical for tumour cell survival and invasion (*Buoso et al., 2020; Cao et al., 2010*).

RACK1 promotes FAK autophosphorylation at Tyr397 upon integrin clustering, generating a docking site for Src-family kinases; efficient Src recruitment additionally requires RACK1 phosphorylation at Y246 by Src itself, establishing a feed-forward loop of mutual activation. The resulting phospho-RACK1-Src-FAK trimeric complex drives targeted substrate phosphorylation at focal adhesions and invadopodia, promoting filopodia and lamellipodia extension at the leading edge that characterize directional cancer cell migration (*Buoso et al., 2020; Ullah et al., 2021*). Upstream of this signalling complex, RACK1 additionally coordinates early focal adhesion assembly through sequential interaction with vinculin and paxillin at spreading initiation centres (SICs), transient structures that precede focal adhesion maturation. This process displays clear phenotypic heterogeneity: in mesenchymal-like cells, SIC-mediated adhesion depends on localized protein translation and RhoA activity, whereas in epithelial cells RACK1 functions predominantly as a ribosomal translational regulator (**Figure 10**). This distinction reflects the broader translational shift associated with EMT, in which RACK1 relocates from the ribosome to focal adhesion complexes where it scaffolds invasion-competent signalling (*Buoso et al., 2020*). Consistent with this, RACK1 extends its pro-invasive influence through stabilization of the vimentin-FAK association required for three-dimensional invasion, and directly facilitates EMT by modulating the expression of mesenchymal markers –

including N-cadherin, vimentin, MMP-2, and MMP-9 – while suppressing E-cadherin (*Ullah et al., 2021*). The hormonal regulation of RACK1 provides an additional layer of control over this migratory programme: in TNBC cells, NF-κB and GR act synergistically at the RACK1 promoter, where the co-presence of a GRE and a c-Rel binding site allows cortisol to suppress and androgen signalling to induce RACK1 transcription, thereby modulating the amplitude of downstream FAK/Src and PI3K/Akt-driven invasion (*Masi et al., 2020*). Taken together, these mechanisms establish RACK1 as a multifunctional regulator of the cytoskeletal remodelling, phenotypic plasticity, and transcriptional reprogramming that underlie the invasive and metastatic behaviour of TNBC cells.

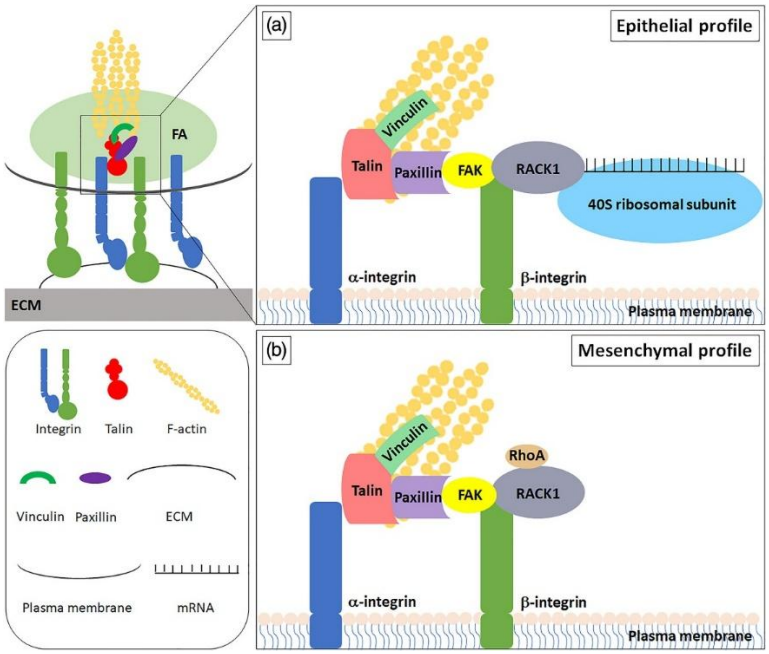

Figure 10. Context-dependent roles of RACK1 at the focal adhesion complex in epithelial and mesenchymal cancer cells. *(A) In the epithelial profile, RACK1 associates with the 40S ribosomal subunit within the FA complex reflecting its predominant function as a translational regulator in this cellular context. (B) In the mesenchymal profile, RACK1 dissociates from the ribosome and instead engages RhoA at the focal adhesion, coordinating cytoskeletal remodelling and directional invasion (Buoso et al., 2020).*

2.5.4. RACK1 in TNBC

Within the TNBC context, elevated RACK1 expression negatively correlates with OS and contributes to the establishment of multiple BC hallmarks. RACK1 intersects with integrin/Src/FAK, PI3K/AKT, ERK/MAPK, and RhoA/Rho signalling cascades, collectively shaping the invasive phenotype of TNBC (*Tian et al., 2023*). Its expression is positively regulated by the PI3K/Akt/NF-κB axis, which sustains the transcription of pro-tumourigenic cytokines and chemokines, including IL-2, IL-4, IL-6, and IL-12 *(Masi et al., 2020*). More broadly, EMT also represents a particularly relevant downstream programme, with RACK1 facilitating mesenchymal transition by modulating N-cadherin, vimentin, MMP-2, and MMP-9 expression while suppressing E-cadherin (*Cao et al., 2009*). In TNBC, RACK1 overexpression further upregulates CD147, amplifying MMP-2 activity and invasiveness *in vitro* and *in vivo*.

At the receptor level, RACK1 bridges IGF-1R and β1 integrin signalling to promote migratory and proliferative responses (*Duff et al., 2017*). Consistent with the centrality of this axis in TNBC, IGF-1 and IGF-2 represent the most potent inducers of mammosphere formation and cancer stem cell (CSC) maintenance in TNBC cells (**Figure 11**) (*Lee et al., 2022*). Stable RACK1 knockdown across TNBC cell lines – including MDA-MB-231 – consistently reduces colony-forming capacity, contracts the CD44(high)/CD24(low) stem-like subpopulation, impairs mammosphere formation, and diminishes tumourigenic capacity *in vivo*, establishing RACK1 as a determinant of the chemoresistant BCSC compartment (*Jia et al., 2025*). In sum, these observations imply that RACK1 targeting would be most impactful in the most aggressive, treatment-resistant TNBC phenotypes (*Ullah et al., 2021*).

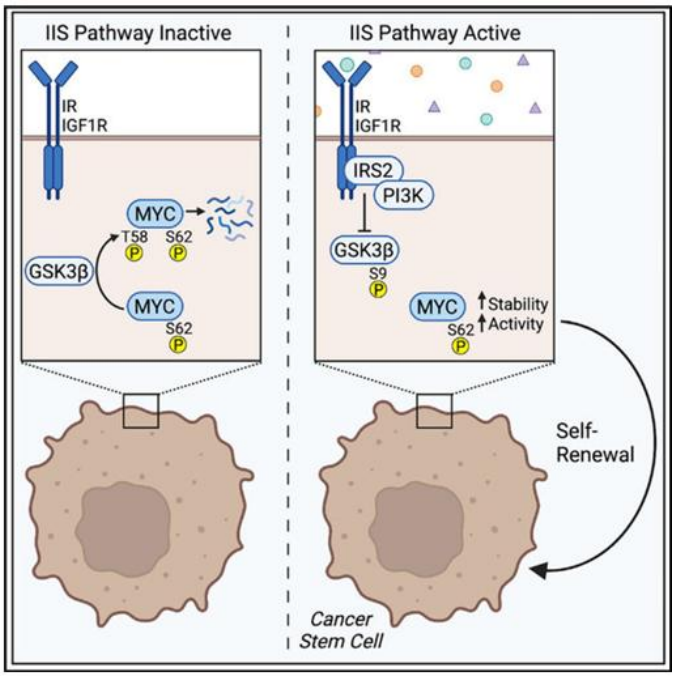

Figure 11. Regulation of cancer stem cell self-renewal by the insulin/IGF signalling pathway in TNBC. *Upon pathway activation (right panel), ligand binding to the insulin receptor (IR) and IGF1R triggers IRS2-mediated PI3K recruitment. The resulting shift in MYC phosphorylation status increases MYC stability and transcriptional activity, sustaining the self-renewal programme of the cancer stem cell compartment. This mechanism identifies the IIS/PI3K/GSK3β/MYC axis as a key determinant of stemness maintenance in TNBC (Lee et al., 2022).*

2.5.5. RACK1 in TME

RACK1 also functions as a molecular interface between innate immune regulation and TME dynamics, with its expression in monocytes and macrophages controlled by the opposing actions of glucocorticoids and androgens. In monocytes, DHEA-derived androgens upregulate both RACK1 and the dominant-negative GRβ isoform, amplifying the release of pro-inflammatory cytokines including TNF-α and IL-8. With physiological ageing, declining DHEA and rising cortisol progressively suppress RACK1 transcription, impairing PKCβII anchoring and blunting cytokine responses – establishing a molecular substrate for endocrine-

driven immunosenescence. In the TME, disruption of androgenic balance similarly dismantles the RACK1-PKCβII signalling required for anti-tumour macrophage activation, shifting the balance toward an immunosuppressive, tumour-permissive state (*Corsini et al., 2016; Racchi et al., 2017*). TAMs represent the primary cellular context through which this immune dysregulation manifests, supporting cancer cell invasion through ECM-remodelling enzymes such as MMP-2 and MMP-9 and pro-inflammatory mediators (**Figure 12**) (*Buoso et al., 2020*).

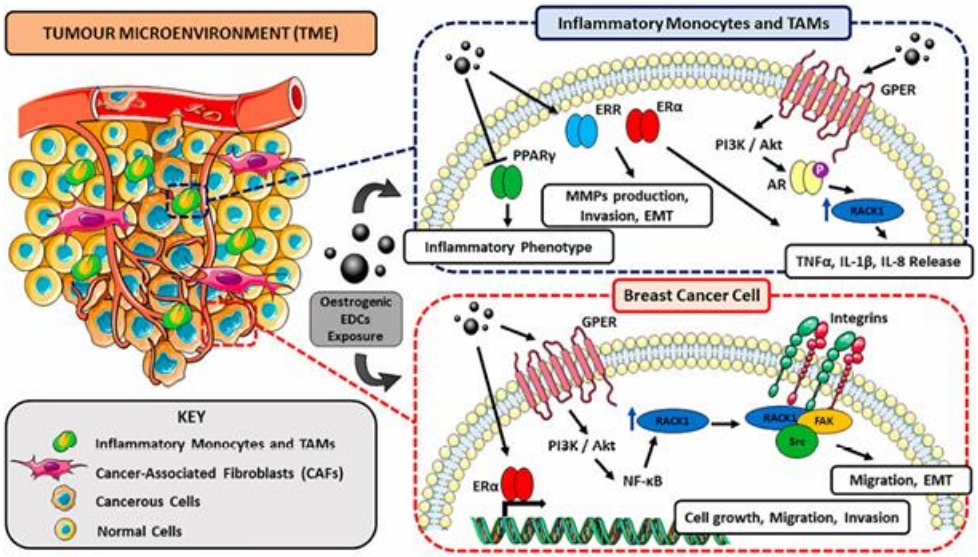

Figure 12. *Schematic representation of the involvement of RACK1 in BC-related TME and tumour progression, where RACK1 favours proliferation and EMT (adapted from Buoso et al., 2020).*

Clinical evidence from oral squamous cell carcinoma demonstrated a strong positive correlation between tumour RACK1 expression and stromal M2 macrophage density, with a high M2/M1 ratio significantly associating with worse OS. Mechanistically, high RACK1 sustains phospho-NF-κB p65 levels that control transcription of IL-6, CSF2, CXCL10, and CXCL2, limiting monocyte infiltration while promoting progressive M2 polarization. RACK1 depletion conversely upregulates

both M1 (phospho-ERK, c-Jun, phospho-NF-κB) and M2 (PPARγ, STAT3) pathway components simultaneously (*Dan et al., 2020*). At the molecular level, RACK1 directly binds the AF1 domain of PPARγ, preventing its proteasomal degradation. This RACK1-PPARγ axis is particularly relevant in TNBC, where PPARγ independently exerts antiproliferative and pro-apoptotic effects, suggesting that RACK1-mediated PPARγ stabilization may influence tumour biology in both immune and malignant cell compartments (*Jiang et al., 2025; Gionfriddo et al., 2020*). Finally, RACK1 directly engages the common β subunit (βc) of the IL-3/IL-5/GM-CSF receptor family, bridging cytokine stimuli to intracellular enzymatic machinery. The stability of these complexes depends on the RACK1-Src interaction, whose dysregulation within the TME amplifies the aberrant cytoskeletal remodelling and hyperactivated Src signalling associated with metastatic dissemination (*Cox et al., 2002*). Collectively, RACK1 exerts a dual function in the TME, simultaneously limiting macrophage infiltration and promoting M2 polarization, thereby establishing a chronically immunosuppressive microenvironment permissive to tumour progression (*Dan et al., 2020*). This positions RACK1 as a multidimensional regulator spanning macrophage polarization, cytokine signalling, and antigen presentation – making it a compelling target for precision cancer immunotherapy (*Yang et al., 2026*).

3. AIM OF THE THESIS

The present work aims to investigate the potential anti-tumour activity of the plant-derived extract A1 against triple-negative breast cancer (TNBC), an aggressive breast cancer subtype characterised by a high metastatic propensity and a well-documented resistance to standard therapeutic strategies.

The study was initially directed towards assessing the anti-tumoral potential of A1 in MDA-MB-231 and SUM-159PT cell lines in both 2D and 3D models, the latter better reproducing the architecture and microenvironment of solid tumours. Accordingly, the effects of A1 on cell viability and migration were evaluated, as these represent key processes involved in TNBC progression and metastasis. The anti-metastatic properties of A1 were subsequently examined using 3D spheroid invasion assays. Within this context, the role of the scaffold protein RACK1 was also explored, given its established involvement in signalling pathways governing cell motility and invasiveness.

Finally, this work intended to extend the investigation beyond the tumour cell compartment, addressing the role of A1 within the tumour microenvironment (TME). Specifically, we assessed whether this extract could modulate immune cell recruitment and macrophage polarization, two processes that critically shape the pro- or anti-tumour nature of the TME.

4. MATERIALS AND METHODS

4.1. Cell culture

In vitro experiments were carried out on MDA-MB-231 and SUM-159PT TNBC cell lines (ATCC and Biovit respectively) and THP-1 monocytes (ATCC).

MDA-MB-231 cells (**Figure 13**) belong to the Mesenchymal molecular subtype and are widely regarded as a prototypical model of highly glycolytic BC. In fact, they display elevated extracellular acidification rates (ECAR) and reduced oxygen consumption rates (OCR) relative to luminal cell lines, a pattern consistent with a predominant reliance on aerobic glycolysis for ATP production (*Farhadi et al., 2022; Urra et al., 2018*). Despite this predominantly glycolytic phenotype, mitochondria retain an essential functional role in MDA-MB-231 cells, particularly in supporting migration and metastasis through mechanisms that involve overexpression of PGC-1α, increased mitochondrial biogenesis, and fatty acid oxidation (FAO)-driven Src signalling. Indeed, OXPHOS activity has been shown to increase concomitantly with metastatic potential in BC, and invasive metastatic cells specifically favour mitochondrial respiration to elevate ATP levels. Taking advantage of the metabolic plasticity of MDA-MB-231 cells, Urra et al. (2018) demonstrated that glucose substitution with galactose generates oxidative subpopulations that rely predominantly on OXPHOS, with glutaminolysis as the principal route for mitochondrial respiration. This suggests that these cells retain the capacity to flexibly reprogram their energy metabolism in response to nutrient availability (*Urra et al., 2018*). Consistent with a pro-metastatic metabolic profile, MDA-MB-231 lactate secretion is particularly prominent and reflects not only high glycolytic flux but also the capacity of MDA-MB-231-conditioned medium to drive pro-tumorigenic reprogramming of TAMs in the TME, including enhanced VEGF secretion (*Dias et al., 2023*).

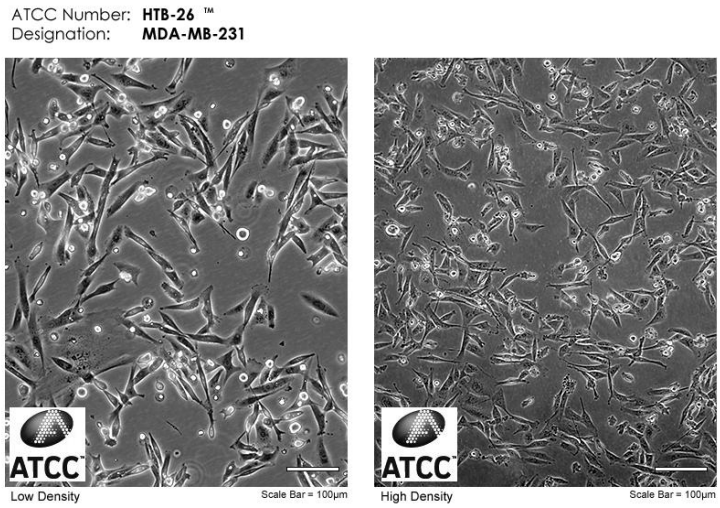

Figure 13. *Phase-contrast micrograph of MDA-MB-231 cells grown in a monolayer culture. The cell line exhibits a typical spindle-shaped, mesenchymal morphology with elongated cytoplasmic extensions, which aligns with its classification as a Mesenchymal TNBC subtype. Image courtesy of ATCC (HTB-26™). (Retrieved from https://www.atcc.org/products/htb-26).*

SUM-159PT (**Figure 14**) is a TNBC cell line established from the primary tumour of a 71-year-old patient diagnosed with anaplastic carcinoma, classified within the Mesenchymal molecular subtype and exhibiting a spindle-like morphology in culture (*Barnabas & Cohen, 2013; Conner et al., 2023*). The line harbours a mutant p53, a heterozygous PIK3CA mutation resulting in an H1047L substitution in the kinase domain of p110α, and a G12D activating mutation in KRAS, placing SUM-159PT among those lines with constitutively active RAS/PI3KCA signalling. Aligned with its origin, the cell line is ER and PR negative, and the p16 gene is deleted, consistent with loss of a key brake on CDK4-mediated Rb phosphorylation and consequent uncontrolled cell cycle progression (*Barnabas & Cohen, 2013*). From a proliferative standpoint, SUM-159PT cells display significantly higher proliferation rates compared to MDA-MB-231, while with regard to migratory behaviour, SUM-159PT cells migrate rapidly in 2D assays at speeds comparable to MDA-MB-231.

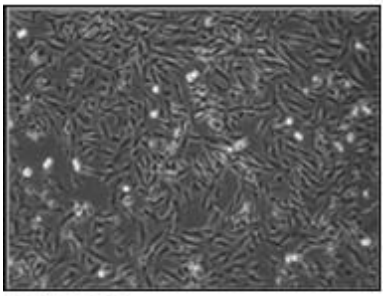

Figure 14. *Phase-contrast micrograph of SUM-159PT cells in a high-confluency monolayer culture. This TNBC cell line displays a predominantly mesenchymal phenotype, characterized by spindle-shaped cells with elongated cytoplasmic extensions alongside minor clusters of rounder, epithelial-like cells (Barnabas & Cohen, 2013).*

Despite this pronounced migratory and invasive activity *in vitro*, SUM-159PT xenografts display only intermediate tumorigenicity in immunocompromised mice and poor spontaneous metastatic dissemination to both the lungs and the liver. This discrepancy underscores the limited predictive value of single *in vitro* motility metrics for *in vivo* metastatic outcome (*Conner et al., 2023*). Morphologically, the study carried out by Westcott and colleagues (2015) demonstrates that the SUM-159PT cell line is an intrinsically heterogeneous population comprising both "trailblazer" and opportunist subpopulations. Particularly, only the "trailblazer" subpopulation possesses the autonomous capacity to initiate collective invasion by extending long cellular protrusions into the extracellular matrix, while the opportunist majority remains non-invasive unless physically guided by trailblazer-led channels (**Figure 15**). Critically, none of the TNBC cell lines tested by Westcott and colleagues contained a 100% pure population of invasive spheroids, meaning that in SUM-159PT culture a significant fraction of spheroids will be composed predominantly of opportunist cells incapable of autonomous invasion (*Westcott et al., 2015*). In contrast, MDA-MB-

231 cells are classified as a constitutively mesenchymal line, characterized in 3D culture by a pronounced invasive behaviour, which may account for their more robust collective invasion across the spheroid population phenotype (*Holliday & Speirs, 2011; Chavez et al., 2010*).

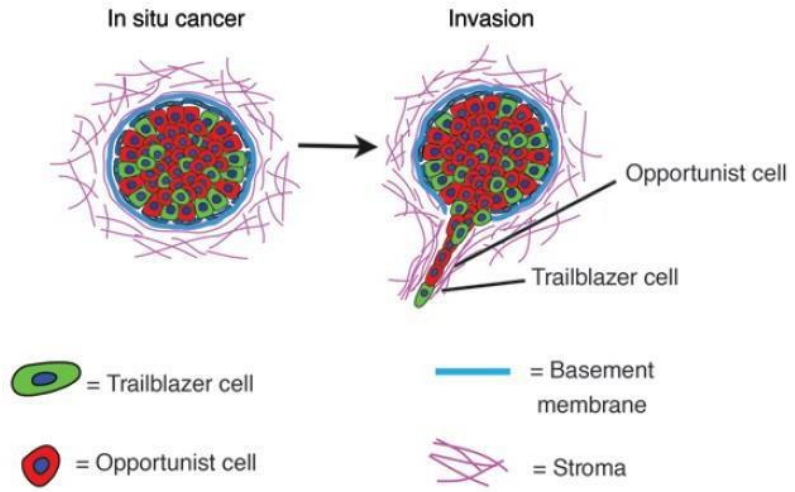

Figure 15. Model of the commensal interplay between "trailblazer" and opportunist subpopulations. *This diagram highlights a cooperative invasion strategy where a small fraction of "trailblazer" cells (green) breaks through the basement membrane. By doing so, they carve out pathways that pave the way for the collective migration of non-invasive opportunist cells (red) into the surrounding stroma (Westcott et al., 2015).*

The THP-1 cell line (**Figure 16**) is a human acute monocytic leukemia cell line originally isolated from the peripheral blood of a one-year-old male patient, which has been extensively adopted as an *in vitro* model to study monocyte and macrophage functions, signaling pathways, and responses to immunomodulatory stimuli. In the undifferentiated state, THP-1 cells display morphological and functional properties resembling primary human monocytes, including expression of pattern recognition receptors such as Toll-like receptors and responsiveness to LPS-induced NF-κB activation (*Chanput et al., 2014*).

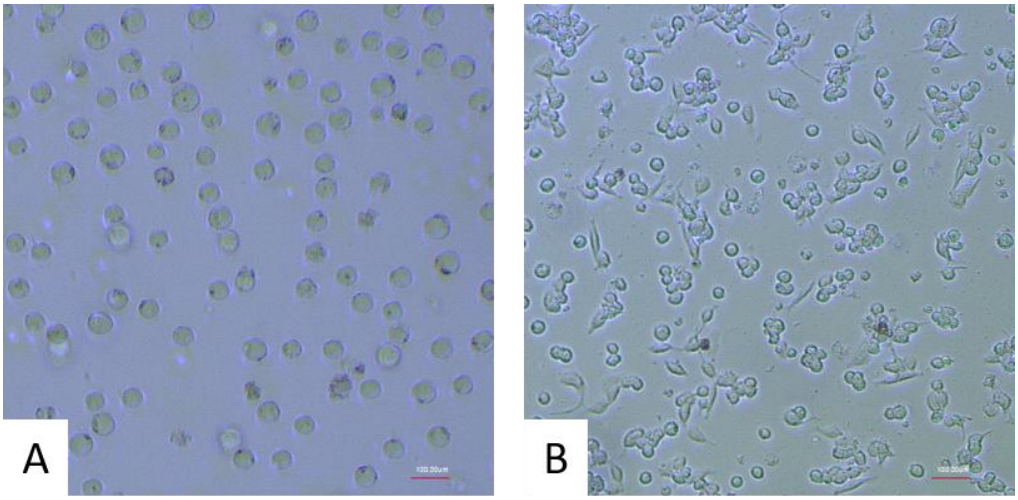

Figure 16. Morphological changes of THP-1 cells during PMA-induced differentiation. *(A) Untreated, wild-type THP-1 human monocytes maintained in suspension culture, exhibiting their characteristic round, non-adherent morphology. (B) THP-1 cells following PMA treatment (M0 macrophages). The cells show a distinct shift toward an adherent phenotype, characterized by cell flattening, spreading, and the extension of cytoplasmic processes (images captured with Motic® AE2000 Series Inverted Microscope equipped with a Moticam 1080 BMH digital camera, 4x objective).*

Differentiation into a macrophage-like phenotype is most commonly achieved through stimulation with phorbol-12-myristate-13-acetate (PMA), enabling the acquirement of a range of features characteristic of primary monocyte-derived macrophages, including cell adherence, increased phagocytic capacity, and surface expression of differentiation-dependent markers such as CD14, CD36, TLR-2, and CR3. Importantly, PMA-differentiated THP-1 macrophages are capable of polarization toward both M1-like and M2-like phenotypes (**Figure 17**) using the same stimuli applied *in vivo*, with IFN-γ combined with LPS driving M1 activation and IL-4 driving M2 polarization, confirming that this model recapitulates the plasticity of primary macrophages (*Chanput et al., 2014*).

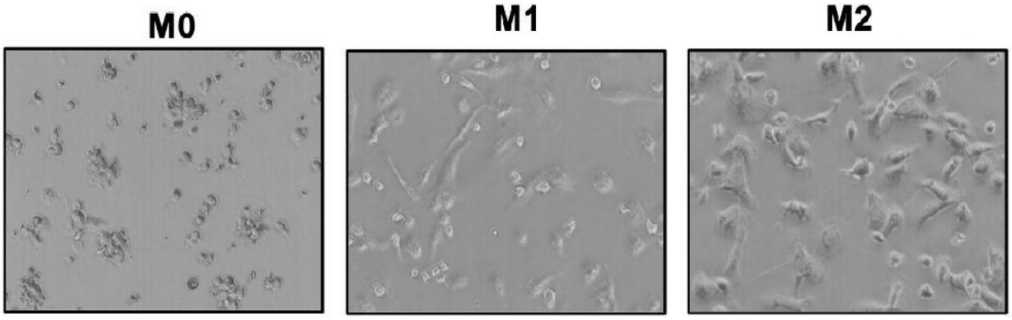

Figure 17. Representative images of THP-1 cells differentiated into M0, M1 and M2 macrophage subsets. *M0 macrophages were generated via PMA treatment alone, serving as a baseline for subsequent polarization into the elongated, pro-inflammatory M1 state and alternatively activated M2 phenotype (adapted from Mazan et al., 2024).*

Specific culture media were employed to meet the nutritional requirements of each cell line. MDA-MB-231 cells were cultured in DMEM high glucose (#D5671, Sigma-Aldrich) enriched with 10% Fetal Bovine Serum (FBS, #ECS5000L, Euroclone), Penicillin and Streptomycin 100 µg/mL (#P0781, Sigma-Aldrich) and L-glutamine 100 µg/mL (#G7513, Sigma Aldrich). The SUM-159PT line, instead, was maintained in DMEM/F12 medium (#D8437, Sigma-Aldrich) enriched with 10% FBS, 5 µg/mL Insulin (#SLCN8992, Sigma-Aldrich), 5 µg/mL Hydrocortisone (#H0888, Sigma-Aldrich), 100 µg/mL Penicillin/Streptomycin, and 25 mM HEPES (#H3375, Sigma-Aldrich) to ensure stable pH buffering. Finally, THP-1 cell line was cultured in RPMI (#R8758, Sigma-Aldrich) enriched with 10% FBS, Penicillin and Streptomycin 100 µg/mL and L-glutamine 100 µg/mL. Phenol red was present in all media as a pH indicator to monitor metabolic acidification. All cultures were kept at 37°C in a humidified 5% CO2 atmosphere to simulate physiological conditions.

Both SUM-159PT and MDA-MB-231 cells were detached from the flask using 1 mL of Trypsin/EDTA 0.05% (#T3924, Sigma-Aldrich), counted using a Bürker chamber, and seeded in a different vessel based on

experiments at density of 90-95% confluence within 24 hours. To generate 3D spheroids, both SUM-159PT and MDA-MB-231, were detached and 1 x 10^4 cells were seeded in 100 µL/well onto a dedicated *Nunclon Sphera 96-U* bottom plate (Thermo Scientific, #174925). To promote cell aggregation, the plate was centrifuged at 200 xg for 15 minutes at 25°C and subsequently incubated for 72 hours in a 5% CO_2 atmosphere.

4.2. A1 preparation

The powder was weighed using an *OHAUS Pioneer*™ analytical balance (OHAUS Corporation, Parsippany, NJ, USA) with a readability of 0.0001 g, and then resuspended in culture media for MDA-MB-231 or SUM-159PT to obtain a final concentration of 3.96 mg/mL. The resulting mixture was vortexed for 2 minutes to ensure complete homogeneity, and subsequently sonicated in a pre-heated ultrasonic water bath (*Emerson Branson 1800 ultrasonic bath*) at 35°C and 30 Hz for 5 minutes. The sample was then placed on a tube rotator for 30 minutes, followed by centrifugation (*Centrifuge NEYA 16R*) for 10 minutes at 4500 rpm at room temperature (RT). Finally, the supernatant was filtered through a 0.22 µm PVDF syringe filter (#9913-2504, Whatman Uniflo™, Cytiva) and adequately diluted in fresh medium to obtain the desired final treatment concentrations.

4.3. MTT assay for cell viability (2D)

The MTT (3-(4,5-dimethylthiazol-2-yl)-2,5-diphenyltetrazolium bromide) assay is a colorimetric method widely employed to assess cell viability and proliferation. The MTT dye undergoes an enzymatic reaction within the mitochondria, where it is reduced to formazan, a water-insoluble compound that precipitates as violet crystals. Since formazan

formation depends on cellular metabolic activity, the absorbance of the dissolved crystals is directly proportional to the number of viable cells. In particular, bot MDA-MB-231 and SUM-159PT were seeded in a 96-well plate at a confluence of 80%, and treated with crescent A1 concentrations (0.028, 0.074, 0.22, 0.66 and 1.98 mg/mL) for 24 and 72 hours.

Stock aliquots of MTT (5 mg/mL; Sigma-Aldrich) were prepared in 1X PBS and stored at -20°C protected from light. For each assay, medium was vacuumed and a 1 mg/mL MTT working solution was added to each well, then cells were incubated at 37°C for 1 hour in the dark. Subsequently, 70 µl of DMSO (#D8418, Sigma-Aldrich) was added to each well to solubilize the formazan crystals. Absorbance was measured at 570 nm using a *Synergy LTEK WNO-Microplate reader* (BioTek® Instruments, Winooski, VT, USA).

4.4. Wound healing assay

The wound-healing assay was performed to evaluate the capacity of A1 treatment to inhibit the *in vitro* migration of MDA-MB-231 and SUM-159PT cells. Every plate was dedicated to a specific time point; t24 hours, t48 hours and t72 hours. On the next day, the confluence was checked and A1 treatment was prepared as described in the previous section. The monolayer of cell was mechanically scratched using a sterile 200 µL pipette tip, and each well was washed twice with sterile 1X PBS to remove cellular debris and non-adherent cells. Then, two wells were dedicated to control groups (CTRL1 and CTRL2) and 750 µL of fresh medium were added. The remaining wells were dedicated to the six treatment conditions (0.028, 0.074, 0.22, 0.44, 0.66 and 1.98mg/mL), and the correct A1 dilution was added in each of them, in a final volume of 750 µL. At 0 hours, three representative fields of view were captured using a *Motic*®

AE2000 Series Inverted Microscope equipped with a *Moticam 1080 BMH* digital camera, 4x objective for each scratch. Plates were then incubated at 37°C in a humidified atmosphere containing 5% CO2. After 24 hours, the dedicated plates were removed from the incubator, placed into ice, and the wells were washed with 400 µL of 1X PBS and then blocked with 400 µL of ice-cold methanol 8% for 30 minutes. A schematic workflow of the assay is provided by **Figure 18**. Subsequently, each well was stained using 400 µL of 1% *Crystal Violet* (#V5265, Sigma-Aldrich) for 20 minutes at room temperature on the bench, and finally rinsed with H_2O to remove excess dye. The same process was replicated with the other plates once 72 hours treatment time-point was reached. At last, three representative images for each scratch were acquired to evaluate wound closure and, consequently, the migratory capacity of the cells. Image analysis was conducted using *ImageJ* software (NIH, Bethesda, MD, USA). To ensure precision, the scratch area was manually delineated with the Freehand Selection tool, and the area was quantified using the Measure function. For each well, the area was calculated as the average of three representative fields. The migration rate was expressed as the percentage of wound closure, calculated using the following formula:

$$\%\, Wound\ closure = \frac{(Area_{to} - Area_{tx})}{Area_{to}} x\ 100$$

Where tx represents the 24 or 72-hour time point. This normalization allowed for a comparative analysis of migration efficiency between control groups and A1-treated SUM-159PT and MDA-MB-231 cells.

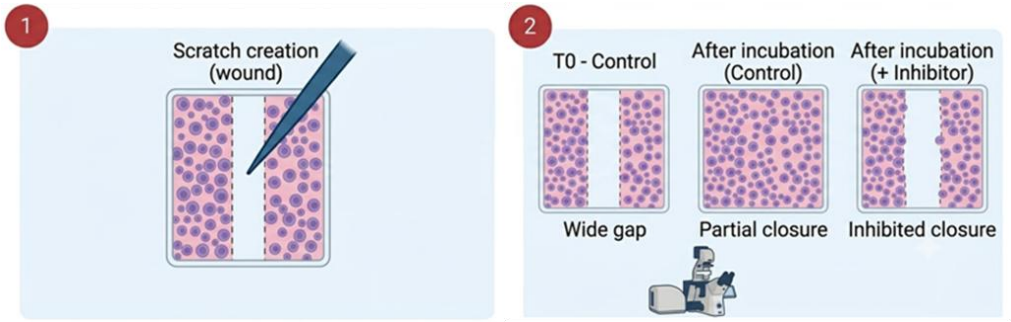

Figure 18. *Schematic representation of the wound healing assay used to evaluate cell migration. (A) A scratch is created in a confluent cell monolayer, and (B) wound closure is monitored over time in control and A1-treated cells (created with BioRender.com).*

4.5. *Transwell*® invasion assay

To investigate the ability of A1 to inhibit cell invasion, a *Transwell*® invasion assay was performed using both SUM-159PT and MDA-MB-231 cells. A schematic representation of the assay mechanism is provided by **Figure 19**, outlining the process from cell seeding to invasion through the protein matrix.

On day 0, 24-well cell culture inserts (8 µm pore size, PET membrane, #PTEP24 hours48, Merck/Millipore) were placed into a 24-well plate under sterile conditions. The invasion barrier was prepared using *Corning® Matrigel® High Growth Factor Basement Membrane Matrix* (#356237, Corning®). After completely defrosting on ice at 4°C, Matrigel was diluted with ice-cold sterile water to obtain a final working solution with a concentration of 0.2 mg/mL. To avoid premature polymerization, all handling steps were performed on ice using pre-cooled pipette tips. A volume of 50 µL of the diluted Matrigel was applied to each insert, ensuring a uniform coating and preventing air bubble formation. The coated inserts were then stored at 4°C overnight.

On day 1, A1 solution was prepared and appropriately diluted in free-serum SUM-159PT and MDA-MB-231 media supplemented with 0.1% of bovine serum albumin (BSA, #A6588, PanReac AppliChem), in order to achieve the final concentration of 0.22 mg/mL and 0.66 mg/mL. At this point, equilibration of the Matrigel layer was achieved by adding 40 µL of incomplete SUM-159PT and MDA-MB-231 media supplemented with 0.1% of BSA to each insert of the control groups, and 40 µL of diluted A1 to the target inserts. The plate was subsequently incubated for 1 hour at 37°C to ensure complete solidification of the matrix.

After the incubation period, SUM-159PT and MDA-MB-231 cells were detached using 1mL of Trypsin/EDTA 0.05%, which was then neutralized using 5mL of respective incomplete media supplemented with 1% of BSA. Cells were then centrifugated at 200 xg for 5 minutes at room temperature, and resuspended in their respective incomplete media containing 0.1% of BSA. Accordingly, the entire procedure was conducted using free-serum media containing BSA, so as to avoid introducing exogenous growth factors from FBS that might interfere with the directionality of the chemotactic gradient. Moreover, a serum-free medium is required in the upper chamber to drive chemotaxis toward the lower chamber.

Cell invasion was initiated by seeding 1 x 10^5 cells in 100 µL per insert in duplicate. To stimulate migration, the lower chamber was filled with 600 µL of conditioned medium (CM), which served as a chemoattractant due to its high concentration of cell-secreted growth factors. This medium was previously collected from SUM-159PT and MDA-MB-231 cultures at 80% confluence (48 hours post-feeding), filtered (0.45 µm), and stored at -20°C. The MW24 was incubated for 5 hours at 37°C in a 5% CO_2 atmosphere to promote invasion.

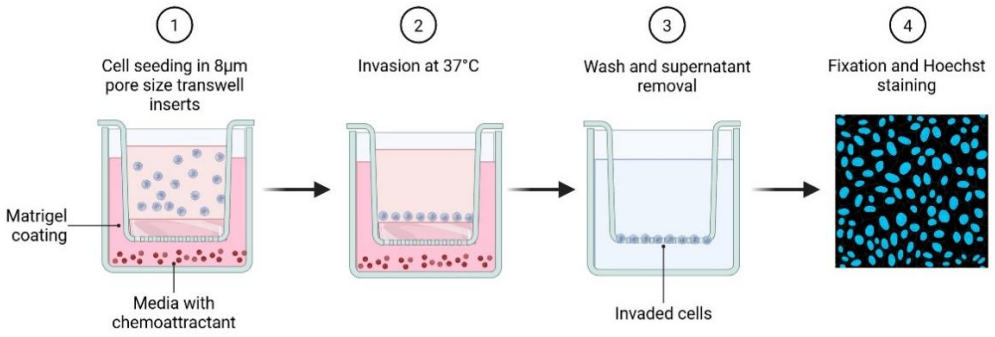

Figure 19. *Schematic workflow of the Transwell® Invasion Assay (created with BioRender.com).*

Following the 5-hour incubation, the plate was placed in an ice bath, and non-invading cells and residual Matrigel were meticulously removed from the upper surface of the membrane using cotton-tipped applicators to ensure the exclusive quantification of invaded cells. The inserts were then rinsed by immersion in 1 mL of 1X PBS. For fixation, the membranes were fixed with ice-cold 70% ethanol for 15 minutes, followed by air-drying. Finally, the inserts were immersed in 600 µL of Hoechst solution 1 µg/mL (3334233258, Sigma-Aldrich, #14530) in 1X PBS for 10 minutes, maintained under dark conditions to prevent photobleaching. Excess dye was removed through three sequential washes in 1mL of 1X PBS. Invaded cells lying on the lower surface of the membrane were imaged using a *Zeiss Axio Vert2 A1* fluorescence microscope with a 10x objective (Carl Zeiss, Oberkochen, Germany). To ensure a statistically robust representation of the invasive process, 14 independent fields of view (FOVs) were systematically captured per insert. As depicted in **Figure 20**, the acquisition pattern integrated 4 central, 5 left, and 5 right frames. This comprehensive mapping strategy was employed to achieve full membrane coverage, thereby minimizing sampling bias and ensuring an accurate assessment of invasive potential across experimental groups.

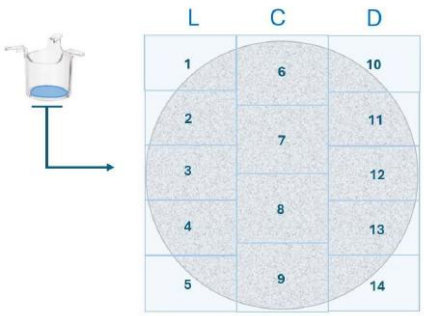

Figure 20. Schematic representation of the field of view (FOV) acquisition strategy*. All acquired frames maintain identical dimensions despite their schematic representation for layout clarity.*

Fluorescence images of Hoecst-stained nuclei were analysed using *ImageJ* software. For each image, a threshold was applied to isolate nuclei from the background, and automatic nuclei counting was performed using the "Analyze Particles" function. Counts from all fields were summed to obtain a total nuclei count (ΣN) per condition. This value was normalised to the corresponding control, and the percentage of invasion (or migration, for THP-1-derived macrophages; see following sections) was calculated as follows:

$$Invasion\ (or\ Migration)\ Index\ (\%) = \left(\frac{\Sigma N_{condition}}{\Sigma N_{CTRL}}\right) x\ 100$$

The protocol was subsequently adapted and applied to THP-1 cells to assess the migratory and invasive behaviour of monocytes toward tumour cells, and to investigate whether treated tumour cells exhibited a reduced secretion of chemoattractant factors, thereby impairing their ability to recruit monocytes. Since THP-1 cells differ from SUM-159PT and MDA-MB-231 cells in terms of invasive and migratory potential, the protocol was adjusted accordingly, with changes primarily concerning the migration timeframe, which was extended from 5 to 24 hours. Moreover, 150,000 cells were seeded in a final volume of 200 µL, including

Matrigel's fraction, without the addition of any treatment in the upper chamber. Prior to seeding in the inserts, cells were serum-starved for 24 hours in serum-free medium to minimize background migration and ensure that the observed chemotactic response was solely attributable to the stimuli present in the conditioned medium placed in the lower chamber, which was collected from tumour cells 24 hours after treatment with 0.22, 0.44, and 0.66 mg/mL. This timepoint was chosen to balance the presence of treatment-modulated secreted factors against the potential confounding contribution of apoptosis-derived mediators, which are known to independently influence immune cell recruitment (*Schimek et al., 2022*). Before use, all collected media were centrifuged at 2000 xg for 5 minutes at 4°C to remove cellular debris. A conditioned medium from untreated tumour cells was included as a control group to establish baseline chemotactic activity. Additionally, to exclude the possibility that serum components present in the collected medium could drive monocyte migration, fresh medium supplemented with 0.66 mg/mL of treatment was included as an additional control, without prior cell exposure. Cell fixation with ethanol, Hoechst staining, and image acquisition and analysis were performed following the same procedure described for the preceding *Transwell*® invasion assay.

In a complementary experimental setup, the lower chamber was instead loaded with MDA-MB-231 cells seeded directly (1.2×10^5 cells in 800 µL in each well of the MW24 plate) and exposed to the same treatment concentrations (0.22, 0.44 and 0.66 mg/mL). This approach was intended to capture a more dynamic secretory environment, as opposed to the static condition provided by pre-collected medium, while also minimising potential artefacts arising from medium collection and storage.

The same assessment was employed to evaluate the migratory capacity of PMA-induced M0 macrophages towards MDA-MB-231 conditioned

medium. To this end, THP-1 cells were seeded in P60 Petri dishes and treated with PMA (#27924, PubChem) at a concentration of 10 ng/mL for 24 hours to induce their differentiation into M0 macrophages. On the following day, differentiated macrophages were detached with Trypsin/EDTA 0.05%, counted, and resuspended in serum-free culture medium to eliminate any confounding chemotactic signals derived from serum components. Cells were then seeded directly into 24-well *Transwell*® inserts (8 µm pore size), and 800 µl of conditioned medium was added to the lower chamber as chemoattractant. Three experimental conditions were tested: one well received conditioned medium from untreated MDA-MB-231 cells; a second well received conditioned medium derived from MDA-MB-231 cells previously treated with A1 at a concentration of 0.44 mg/mL; and a third well served as a positive control (CTRL+), in which LPS from *Escherichia coli* (O127:B8) at a concentration of 1 µg/mL (#L3129, Sigma-Aldrich) was added to the lower chamber as a known macrophage chemoattractant. The final steps, including insert washing, cell fixation and staining, and image acquisition and analysis, were performed as previously described.

4.6. CellTiter-Glo® 3D assay

Cell viability was assessed using the ATP-based *CellTiter-Glo® 3D Cell Viability Assay* (Promega, Madison, WI, USA), a bioluminescent method specifically designed for 3D culture models. This assay relies on the quantification of intracellular ATP, a marker of metabolically active cells whose levels are directly proportional to the number of viable cells present in the sample.

The CellTiter-Glo® 3D reagent was stored at -30 to -10°C, aliquoted to avoid repeated freeze-thaw cycles, and thawed overnight at 4°C before

use, followed by equilibration at room temperature for 30 minutes. The assay was performed according to the manufacturer's instructions. Briefly, following treatment eight spheroids per condition (untreated spheroids and treated ones with 0.028, 0.074, 0.22, 0.66 and 1.98 mg/mL for 24 and 72 hours) were pooled into a single tube, centrifuged at 200 xg for 5 minutes, and washed once in 1X PBS before being transferred to a 96-well plate. An equal volume of CellTiter-Glo® 3D reagent relative to the PBS was then added to each well. The plate was protected from light and gently agitated for 25 minutes at room temperature to induce spheroid lysis and release of intracellular ATP. Under these conditions, the luciferase enzyme contained in the reagent catalyses the oxidation of luciferin in the presence of ATP, generating a luminescent signal proportional to the amount of ATP present, and therefore to the number of viable cells (**Figure 21**). Following an additional 25-minute incubation at room temperature to stabilise the luminescent signal, luminescence was recorded using a *Synergy LTEK WNO-Microplate reader*.

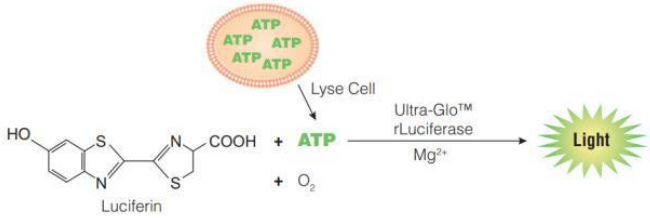

Figure 21. *Scheme of the bioluminescent reaction's mechanism (adapted from CellTiter-Glo® 3D Cell Viability Assay technical manual).*

4.7. Cell Viability Assessment by LIVE/DEAD Staining (3D)

After spheroid formation (described in section 4.1.), cell viability was evaluated using the *LIVE/DEAD™ Cell Imaging Kit* (Thermo Fisher Scientific), based on Calcein AM and propidium iodide (PI) staining, following the manufacturer's protocol. In this case, spheroids were stained

after a 72 hours treatment with A1 at 0.22 and 0.66 mg/mL. After the addition of the staining solution, spheroids were imaged after a 20-minute incubation using a *Zeiss Axio Vert2 A1 fluorescence microscope*. To quantify cell death, fluorescence signals for Calcein AM (Ex = 485 nm, Em = 530 nm) and PI (Ex = 535 nm, Em = 620 nm) were measured using a *Synergy Multi-Mode Microplate Reader* with an integration time of 10 seconds. Cell death was expressed as the PI/Calcein AM fluorescence ratio.

4.8. 3D spheroids invasion assay

To investigate whether A1 treatment reduces cell invasion, a 3D spheroid invasion assay was performed within a complex protein matrix, as this model closely mimics the structural and microenvironmental architecture of a solid tumour, providing a more physiologically relevant context compared to traditional 2D assays. An overview of the experimental workflow, from spheroid formation to imaging, is provided in **Figure 22**.

Spheroids from both MDA-MB-231 and SUM-159PT cell lines were generated as previously described in Section 4.1. After the 72-hour incubation, the A1 treatment was prepared, and two spheroids per condition were selected for treatment. Starting from a stock solution of 3.96 mg/mL, A1 was diluted in fresh medium and subsequently mixed with ice-thawed Corning Matrigel using cold tips on ice, at a ratio of 55 µL of diluted treatment to 45 µL of Matrigel, so as to reach a final concentration of 3 mg/mL in the mixture. From each well to be treated, 50 µL of medium were removed, and 100 µL of the Matrigel + treatment mixture was added, bringing the final volume to 150 µL per well. Treatment concentrations were calculated accounting for all dilution steps, including the Matrigel addition and the residual medium in the well, yielding the following final concentrations in the well: 0.028, 0.074, 0.22,

0.44, 0.66, and 1.98 mg/mL. Two control groups were also included in the experiment design. Plates were then centrifuged at 200 xg for 15 minutes at 25°C. Images were acquired at T0 and T72 using a *Motic® AE2000 Series Inverted Microscope equipped with a Moticam 1080 BMH digital camera*.

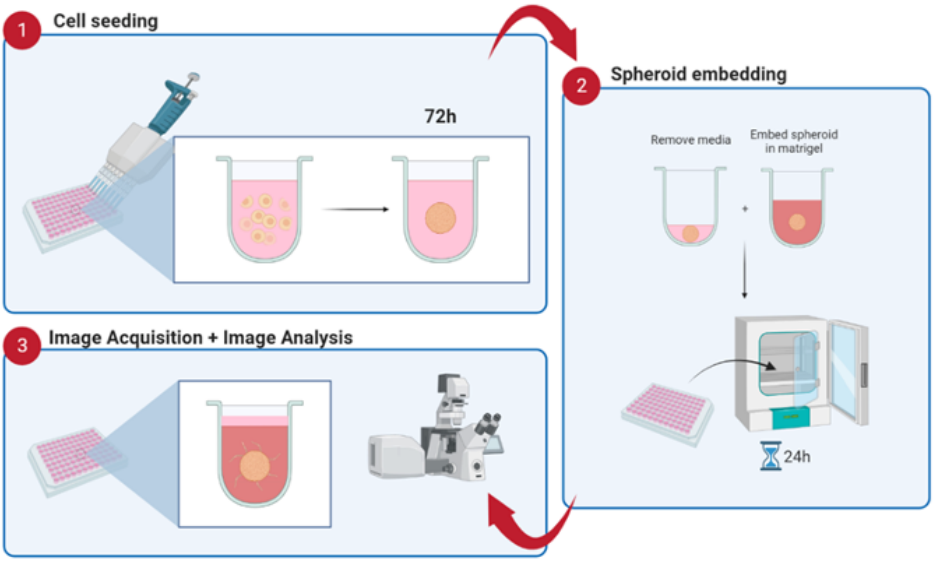

Figure 22. *Schematic overview of the 3D spheroid invasion assay protocol (adapted from cellomaticsbio.com).*

The images were then analysed with *ImageJ* software, where manual segmentation with the Freehand Selection tool in *FIJI* was chosen over automated thresholding algorithms to achieve maximum precision. In particular, the net invasive area of each spheroid was determined by measuring both the Core Area (the compact central body at 72 hours) and the Total Area (the entire surface covered by the spheroid at 72 hours, inclusive of all peripheral invasive protrusions). **Figure 23** shows the manually traced contours used to delineate the Core Area and Total Area of spheroids at 72 hours.

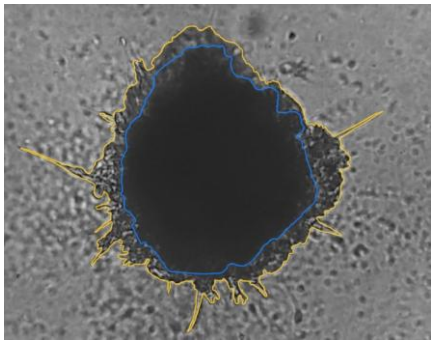

Figure 23. *Representative image of a spheroid showing the boundaries used to define the Core Area (blue) and the Total Area (yellow), which includes the peripheral invasive protrusions.*

The Invasive Area was then determined by subtracting the Core Area from the Total Area, thereby isolating the surface area covered only by the invasive protrusions. Finally, the Invasion Index (%) was calculated using the following equation:

$$Invasion\ Index\ (\%) = \left(\frac{Invasion\ Area\ _{tx}}{Total\ Area\ _{t0}}\right) x\ 100$$

Where tx represents the 72-hour timepoint. These quantitative parameters allowed for a precise comparison between treated and untreated spheroids, effectively determining the potential of A1 to impair tumour cell invasion *in vitro*. Following treatment, spheroids were collected and centrifuged at 200 xg for 10 min at 4°C using a *Thermo Scientific MicroCL 17R centrifuge* to obtain a pellet for subsequent western blot analysis.

4.9. Apricell Technology (3-in-1 Plate)

The *Apricell 3-in-1 Plate* (Apricell Biotechnology) is a hydrogel-based microfluidic-integrated culture device specifically designed for 3D cell culture. Its hydrogel inserts are fabricated by replica molding of 3D-printed microfeatures and incorporate U-shaped microwells that ensure

efficient and reproducible spheroid formation. Each well is subdivided into four distinct quadrants, each containing six microstructures, allowing the simultaneous generation of six spheroids per quadrant (**Figure 24**). Both MDA-MB-231 and SUM-159PT cells were seeded into the Cell/ECM Loading Zone of each insert compartment. Unattached cells remaining in the channel after seeding were washed out by adding medium at the Cell/ECM Loading Zone and removing it from the Secondary Reservoir, repeating the procedure three times. Spheroid formation was subsequently monitored by inverted microscopy.

Following 72 hours of treatment (A1 at a concentration of 0.22 mg/mL), the medium was gently aspirated from the Media Reservoir and an ECM hydrogel solution (Corning®) was introduced into the Cell/ECM Loading Zone. The plate was then incubated for 2-5 minutes under a laminar flow hood to allow the hydrogel to fill the entire microchannel network and microwells of each compartment. After cross-linking, pre-warmed fresh culture medium was added to both the Media Reservoir and the Cell/ECM Loading Zone. Once embedded within the ECM hydrogel, cells at the spheroid periphery began to invade through the interconnecting microchannels. Invasion was monitored daily under bright-field microscopy and invasion length within the ECM was tracked longitudinally over time. Images were acquired using a *Zeiss Axio Vert2 A1 inverted microscope*, and spheroid volume was quantified with *ImageJ* software.

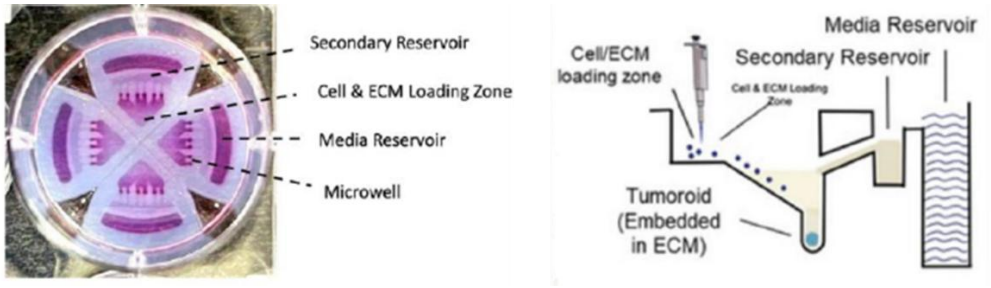

Figure 24. Microfluidic-integrated culture plate for 3D tumoroid array generation in MDA-MB-231 and SUM-159PT TNBC cells. *(A) Top-view of the microwell arrays and homogenous size of the tumoroids within a quadrant. (B) Side-view schematic of the tumoroid generation insert. Each insert includes the tumoroid formation and drug delivery modules (adapted from Seyfoori et al., 2025).*

4.10. Evaluation of THP-1 Cell Health Status upon LPS Treatment by Western Blot Analysis

To evaluate THP-1 cell health status upon LPS treatment, monocytes were seeded in 6-well plates at a density of 1.5 x 10^6 cells per well in a final volume of 1.3 mL. The following day, an LPS (#L3126, Sigma-Aldrich) stock solution was prepared at 1 mg/mL in sterile Milli-Q water, from which an intermediate working solution at 10 µg/mL was obtained. Cells were stimulated with LPS at final concentrations of 10 ng/mL or 100 ng/mL. For each condition, cells were harvested at two time points after LPS stimulation, 1.5 and 3 hours, alongside untreated and DMSO controls.

Samples fractionation:

At each time point, cells were collected and subjected to subcellular fractionation to separate cytosolic and nuclear compartments. Briefly, cell suspensions were centrifuged at 100 xg for 5 min at room temperature, and the resulting pellet was washed once in 1 mL of cold 1X PBS before a second centrifugation under the same conditions. Pellets were then resuspended in 150 µL of fractionation buffer supplemented with protease

inhibitors (1:1000, #PCC1010, Sigma-Aldrich) and homogenized in a glass-glass Dounce homogenizer with approximately 20 strokes on ice. Homogenates were centrifuged at 400 xg for 5 minutes at 4 °C; the resulting supernatant, corresponding to the cytosolic fraction, was collected, while the pellet (nuclear fraction) was resuspended in 100 µL of fractionation buffer with protease inhibitors (1:1000). Both fractions were sonicated twice at 30 Hz for 10 seconds, with a 5 seconds rest interval on ice between pulses to prevent sample overheating, and stored at -20 °C until further processing. Western blot analysis was then carried out as described in Section 4.12.

4.11. Indirect Co-culture of MDA-MB-231 and THP-1 cells for Macrophage Polarization Assessment by Flow Cytometry

To model the paracrine crosstalk between tumour cells and macrophages, an indirect co-culture system was employed, in which MDA-MB-231 cells and THP-1-derived macrophages were physically separated by a 0.4 µm pore *Transwell*® polycarbonate membrane cell culture inserts in 6-well plates (#3412, Costar, Corning Inc.), allowing exclusively soluble factor-mediated communication while preventing direct cell-to-cell contact. In particular, this assay was carried out to assess the ability of TNBC cell-secreted signals to influence the polarization of M0 macrophages into M1 and M2 subtypes.

On day 1, 3 x 10^5 MDA-MB-231 cells were seeded onto a 6-well plate (#30006, SPL Life Sciences) in a final volume of 2.5 mL. Subsequently, 6 x 10^5 THP-1 cells were seeded in a final volume of 1.2 mL into 0.4 µm *Transwell*® polycarbonate membrane cell culture inserts in 6-well plates, and 2.5 mL of fresh medium were added to each well. Following the protocol described by Mazan and colleagues (2023), THP-1 cells were

immediately treated with PMA at a final concentration of 10 ng/mL to induce their differentiation into M0 macrophages. Both plates were then incubated for 24 hours (**Figure 25**).

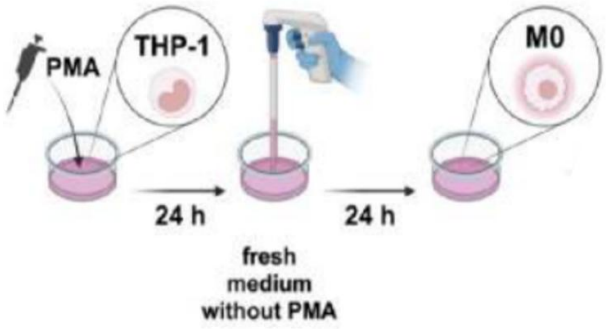

Figure 25. *Schematic overview of the PMA-induced differentiation of THP-1 monocytes into M0 macrophages (adapted from Mazan et al., 2023).*

On day 2, an A1 stock solution was prepared at a final concentration of 3.96 mg/mL, and three wells containing MDA-MB-231 cells was treated at a final concentration of 0.44 mg/mL in 2.5 mL, following a wash with 1X PBS. At this point, differentiation of THP-1 cells into M0 macrophages was considered complete, and the medium containing PMA was aspirated from the inserts and replaced with 1.2 mL of fresh medium. The inserts were then transferred into the wells in which MDA-MB-231 cells had been previously seeded, establishing the indirect co-culture. The plate was then incubated for a further 24 hours.

On day 3, the plate was removed from the incubator, the supernatant collected from each well, centrifuged at 1200 xg for 5 minutes at 4°C to remove cellular debris, and stored at -80°C for subsequent analysis.

Sample preparation for flow cytometric analysis:

Each insert was washed with 500 µL of 1X PBS, and adherent M0 macrophages were detached by incubation with 400 µL of Trypsin/EDTA 0.05% for one minute. Trypsin/EDTA was then inactivated by the addition of 1 mL of fresh medium, and the cells were centrifuged using a *Thermo Scientific MicroCL 17R centrifuge* at 150 xg for 5 minutes. The supernatant was discarded and the pellet resuspended in 100 µL of 1X PBS, followed by a second centrifugation under the same conditions. After discarding the supernatant, the pellet was resuspended in 10 µL of *Fc blocker solution* (#553142, Fc Block™ clone 2.4G2, BD Biosciences) at 0.5 µg/µL using filtered pipette tips, and incubated on ice for five minutes to minimise non-specific antibody binding.

Subsequently, 50 µL of antibody/FACS buffer mix was added to each sample for extracellular surface marker staining. BB700-conjugated rat anti-mouse CD86 (#742145, clone PO3, BD OptiBuild™) and PE-conjugated rat anti-mouse CD206 (#568273, clone Y17-505, BD Pharmigen) antibodies were each diluted 1:100 (0.5 µL per antibody) in a mix composed of equal volumes of FACS buffer and *Brilliant Stain Buffer* (#566349, BD Biosciences), to a final volume of 50 µL. Five staining conditions were prepared: one sample of unstained and one double-stained (CD86 + CD206) cells from the control group, one sample of double-stained cells from the treated group, and single-stained samples for CD86 and CD206 individually from two additional treated samples. In addition, an unstained wild-type THP-1 sample (undifferentiated monocytes) was included as a reference control to allow gating discrimination between monocytes and macrophages based on their distinct scatter profiles, and to confirm that PMA-induced differentiation had been successfully achieved. All samples were incubated for 30 minutes on ice.

Cells were then fixed: samples were centrifuged at 200 xg for five minutes at 4°C, the supernatant discarded, and the pellet resuspended in 100 µL of FACS buffer supplemented with 1% paraformaldehyde (PFA, #P6148 Sigma-Aldrich) resuspended in Milli-Q H_2O. Samples were incubated for 15 minutes on ice, after which 300 µL of FACS buffer were added to each tube to achieve an optimal cell concentration for cytofluorimetric acquisition.

4.12. Western blot (WB) analysis

Sample preparation:

Following treatment, spheroids were collected and centrifuged at 200 xg for 10 min at 4°C using a *Thermo Scientific MicroCL 17R centrifuge*. The resulting pellets were lysed in homogenization buffer containing 50 mM Tris-HCl (pH 7.4), 150 mM NaCl, 5 mM EDTA, and 1% Triton X-100, supplemented with a protease and phosphatase inhibitor cocktail (#PCC1010, Sigma-Aldrich) at a 1:1000 dilution.

Cell lysates were incubated on ice for 20 minutes and subsequently sonicated three times at 30 Hz for 10 seconds using an *Emerson Branson 1800 ultrasonic bath*. Total protein concentration was determined using the Bradford assay (Quick Start™ Bradford 1X Dye Reagent, Bio-Rad, #5000205), with BSA used as standard. Absorbance was measured at 595 nm using a *Synergy LTEK WNO-Microplate reader*. To prepare samples for Western blotting, cell lysates were mixed with 4X sample buffer (#1610747, Bio-Rad) supplemented with 10% β-mercaptoethanol (#M3148, Sigma-Aldrich), followed by heat denaturation at 95°C for 2 minutes.

Sodium Dodecyl Sulphate – PolyAcrylamide Gel Electrophoresis (SDS-PAGE):

Protein analysis was carried out via Sodium Dodecyl Sulfate-Polyacrylamide Gel Electrophoresis (SDS-PAGE). The gel was prepared in two distinct sections:

10% Running Gel (10 mL final volume):

- 4.6 mL Ultrapure water (Milli-Q H_2O)
- 2.6 mL, 40% Acrylamide/Bis-acrylamide solution (#A7168, Sigma-Aldric)
- 2.5 mL, 1.5 M Tris-HCl (pH 8.8)
- 0.1 mL, 10% Sodium Dodecyl Sulfate (SDS)
- 0.1 mL, 10% Ammonium Persulfate (APS)
- 30 μL TEMED (#T9281, Sigma-Aldrich)

5% Stacking Gel (6 mL final volume):

- 3.79 mL Ultrapure water (Milli-Q H_2O)
- 1.33 mL, 40% Acrylamide/Bis-acrylamide solution
- 0.75 mL, 1.0 M Tris-HCl (pH 6.8)
- 0.06 mL, 10% Sodium Dodecyl Sulfate (SDS)
- 0.06 mL, 10% Ammonium Persulfate (APS)
- 15 μL TEMED

After the addition of TEMED, the resolving gel solution was poured between the glass plates and allowed to polymerize. To obtain a flat gel surface, a layer of propan-2-ol was carefully added to the top of the gel. Polymerization was carried out between two glass plates separated by a 1

mm spacer and assembled in a *Mini-PROTEAN II system* (Bio-Rad). Once polymerization of the resolving gel was complete, the propan-2-ol was removed and TEMED was added to the stacking gel solution, which was subsequently poured on top of the resolving gel. An appropriate comb was inserted to create the sample wells. After complete polymerization, the gel was mounted in the electrophoresis apparatus and the comb was carefully removed. Protein samples (10-20 μg per lane) were then loaded into the wells. Electrophoresis was performed for approximately 1.5 hours using a *PowerPac™ Basic Power Supply* (Bio-Rad, Hercules, CA, USA). Samples were initially run at 100 V through the stacking gel and subsequently at 130 V once they entered the resolving gel.

Protein transfer to membrane:

Following electrophoretic separation, proteins were transferred onto a nitrocellulose (NC) membrane using the *Trans-Blot Turbo System* (Bio-Rad, Hercules, CA, USA). Protein transfer was performed with the Trans-*Blot Turbo Midi Transfer Pack* (#1704159, Bio-Rad), a pre-assembled system optimized for rapid and efficient semi-dry blotting. The transfer sandwich was assembled inside the cassette in the following order, from cathode to anode: a transfer buffer-soaked sheet, the NC membrane pre-equilibrated in transfer buffer, the gel, and a second transfer buffer-soaked sheet. Transfer was carried out using the Mixed Molecular Weight program (1.3 A, 25 V) for 7 minutes, following the manufacturer's recommendations.

Membrane blocking and protein incubation:

Following protein transfer, membranes were rinsed with Milli-Q water and stained using *Ponceau S solution* (AdvanStain Ponceau, #R-03021-D050,

Advansta) for total protein normalization, according to the manufacturer's instructions. After staining, membranes were blocked for 30 minutes at room temperature (RT) in 1X TBS-T containing either 5% BSA or 3% milk, depending on the target protein. Following the blocking step, membranes were cut according to the molecular weights of the proteins of interest and incubated overnight at 4°C with the appropriate primary antibodies. The following primary antibodies were used:

- Mouse monoclonal anti-RACK1 antibody (B-3) (#sc-17754, Santa Cruz Biotechnology), diluted 1:1000 in 5% BSA.
- Anti-Lamin A/C primary antibody (4C11, #4777S, Cell Signaling Technology), diluted 1:1000 in 3% milk.
- Anti-NF-κB p105/p50 primary antibody (D4P4D, #13586S, Cell Signaling Technology), diluted 1:1000 in 5% BSA.

After primary antibody incubation, membranes were washed three times for 10 minutes each with 1X TBS-T and subsequently incubated for 1 hour at RT with species-specific horseradish peroxidase (HRP)-conjugated secondary antibodies diluted in 1X TBS-T. In particular, the following secondary antibodies were used:

- Anti-mouse secondary antibody (#1706516, Bio-Rad), diluted 1:2000 in 5% BSA (RACK1), and 1:3000 in 3% milk (Lamin A/C).
- Anti-rabbit secondary antibody (#1706515, Bio-Rad), diluted 1:10000 in 5% BSA (NF-κB p50).

Following secondary antibody incubation, membranes were washed three times for 10 minutes each with 1X TBS-T prior to signal detection.

Immunoblot image acquisition:

Antigen-antibody complexes were visualized by chemiluminescence by incubating the membranes with the *WesternBright Enhanced Chemiluminescence (ECL) HRP substrate* (Advansta Inc., San Jose, CA, USA) for 1 minute, and the resulting chemiluminescent signal was captured using a *ChemiDoc™ MP Imaging System*. Band intensities were quantified using *ImageJ* software (W. Rasband, Research Service Branch, National Institute of Mental Health, National Institutes of Health, Bethesda, MD, USA) and normalized to the corresponding loading controls.

Statistical analysis:

Statistical analyses were performed using *GraphPad Prism* version 10 (GraphPad Software, San Diego, CA, USA). Differences among experimental groups were evaluated by analysis of variance (ANOVA) followed by the appropriate post hoc tests, while comparisons between two groups were assessed using a Dunnett's test when applicable. A p-value < 0.05 was considered statistically significant. All experiments were conducted in three independent biological replicates to ensure the reproducibility and reliability of the results.

5. RESULTS

5.1. Impact of A1 on cell viability, migration, and invasion in 2D TNBC models

The cytotoxic potential of natural extract A1 was evaluated in TNBC cellular models using the MDA-MB-231 and SUM-159PT cell lines. The MTT assay revealed a marked reduction in cell viability in both cell lines **(Figure 26A, B**) thus identifying 0.22 mg/mL as the first concentration to exhibit relevant cytotoxic activity. Specifically, A1 treatment at a concentration of 0.22 mg/mL led to a decrease in viability of 35-40% in MDA-MB-231 cells after 24 hours (**Figure 26A**), whereas SUM-159PT cells showed a smaller reduction of 20-30% under the same conditions (**Figure 26B**). At a concentration of 0.66 mg/mL, both cell lines displayed a comparable degree of cytotoxicity at 24 hours, with viability decreasing to approximately 60. This effect was markedly more pronounced after 72 hours in both lines, with viability dropping below 20% in MDA-MB-231 cells and below 30% in SUM-159PT cells. This indicates that, the cytotoxic effect of A1 is potentiated over time in indicating a time-dependent potentiation of the cytotoxic effect of A1 across both TNBC models.

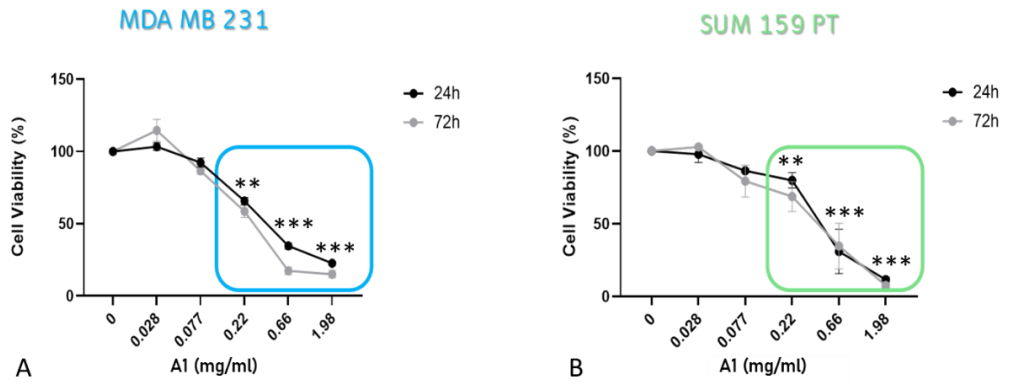

Figure 26. Effect of A1 on cell viability in TNBC cell lines analysed with MTT assay. *Cell viability of 2D (A) MDA-MB-231 and (B) SUM-159PT TNBC cells after treatment with increasing concentrations of A1 (0.028-*

*1.98 mg/mL) at 24 hours (black lines) and 72 hours (grey lines), expressed as percentage of viable cells normalized to untreated controls (0 mg/mL). Significant reductions in viability were observed from 0.22 mg/mL concentration (blue and green rectangles). Data represent mean ± SEM from three independent experiments performed in quadruplicate; Statistical analysis was performed with one-way ANOVA followed by Dunnett's multiple comparisons test (**p < 0.01, ***p < 0.001).*

To investigate the anti-migratory capacity of A1, a 2D wound healing assay using both MDA-MB-231 and SUM-159PT cell lines was performed. A1 exhibited a strong inhibition of cellular migration in both cell lines (**Figures 27A and 28A**). The two lowest concentrations tested (0.028 and 0.077 mg/mL) did not affect wound closure area compared to controls, whereas 0.22 mg/mL was identified as the lowest effective concentration capable of significantly impairing wound closure already at 24 hours post-treatment. Higher concentrations exerted a markedly more pronounced inhibitory effect.

However, a 72-hour endpoint was also included to assess whether the inhibitory effect was sustained over time. In MDA-MB-231 cell line 0.22 mg/mL reduced wound closure to 50% after 24 hours (**Figure 27B**). By 72 hours, the wound had closed by 85%, indicating that, while 0.22 mg/mL delays cell motility, complete and persistent inhibition of migration requires higher concentrations. A marked difference was observed between the 0.22 and 0.66 mg/mL conditions, with 0.66 mg/mL almost completely preventing wound closure, whereas cells treated with 0.22 mg/mL retained a substantial migratory capacity by 72 hours. A similar significant reduction was observed with 0.44 mg/mL A1, whereas the highest concentration tested (1.98 mg/mL) significantly arrested migration, resulting in wound closure of 4% and 0% at 72 hours, respectively. Importantly, this impaired wound closure strongly correlates with the marked reduction in cell viability and density observed at these

higher concentrations (**Figure 26A**), which is also visually reflected by the sparse monolayer in the brightfield images (**Figure 27A**).

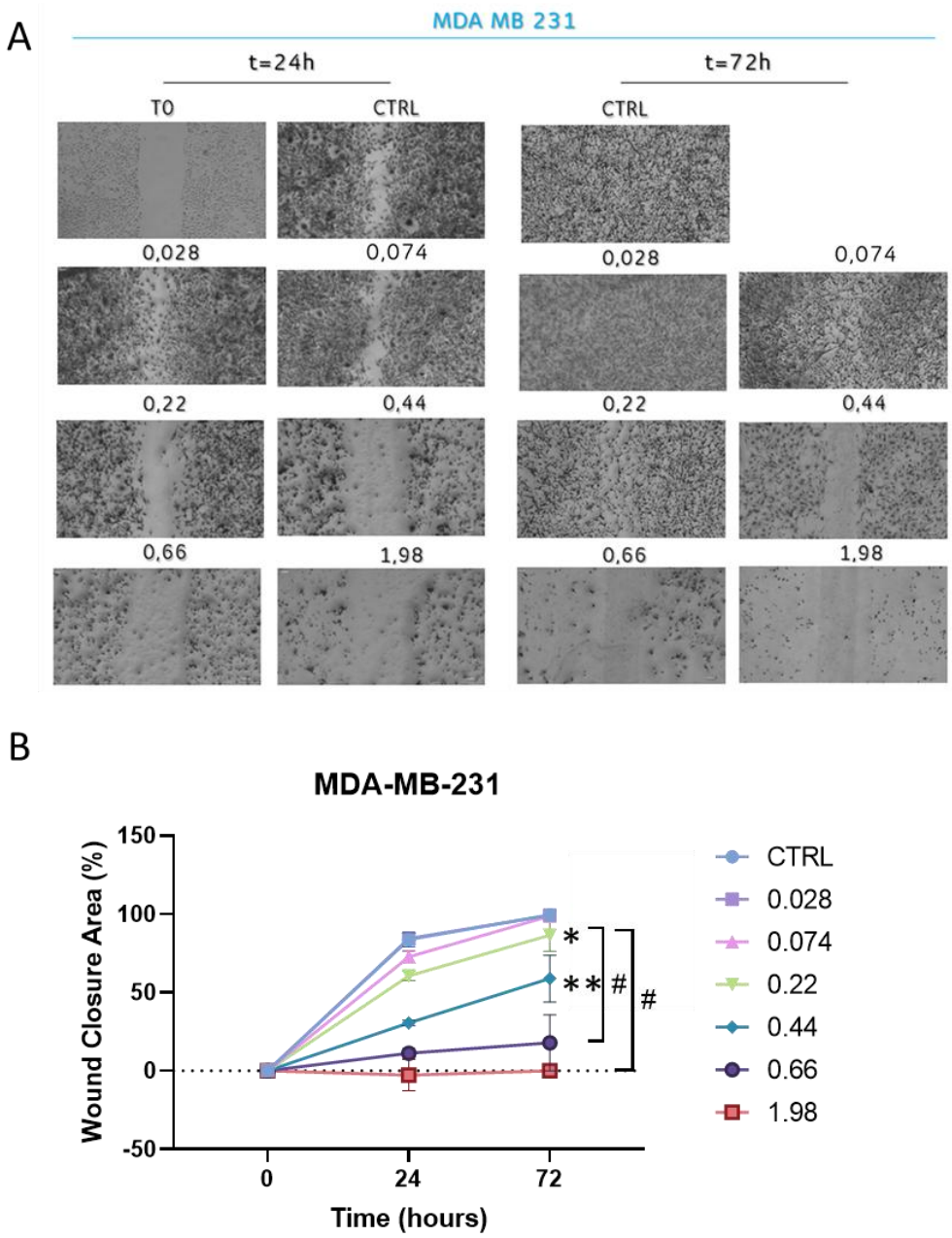

Figure 27. A1 treatment significantly reduces cell migration. *(A) MDA-MB-231 cells migration by scratch wound healing assay, performed as described in materials and methods. MDA-MB-231 cells were cultured without (CTRL) or with different A1 concentrations (0.028 - 1.98 mg/mL)*

*and subsequently migration was analysed at 24 and 72 hours. The image is a representative result. (B) Value bars in the graph represents the mean ± SEM of three independent experiments, in duplicate. The analysis was performed by two-way ANOVA with Dunnett's multiple comparisons test with *p < 0.05, **p < 0.01, and Bonferroni's test with #p < 0.05 A1 0.22 mg/mL vs 0.66 mg/mL. Scale bar = 100 µm.*

A consistent inhibitory trend was also observed in SUM-159PT cells (**Figure 28B**). Treatment with 0.22 mg/mL resulted in a wound closure of 49% at 24 hours and 58% at 72 hours. At 0.66 mg/mL, wound closure reached only 12%, while at the highest concentration tested (1.98 mg/mL), the wound area even increased. This value reflects extensive cell detachment and death rather than a decrease in active migration, directly correlating with the drastic reduction in cellular density observed at 72 hours (**Figure 28A**). Overall, these results demonstrate that A1 inhibits both cell viability and migratory capacity in MDA-MB-231 and SUM-159PT TNBC cell lines in a time-dependent manner. The lowest effective concentration identified across both assays was 0.22 mg/mL.

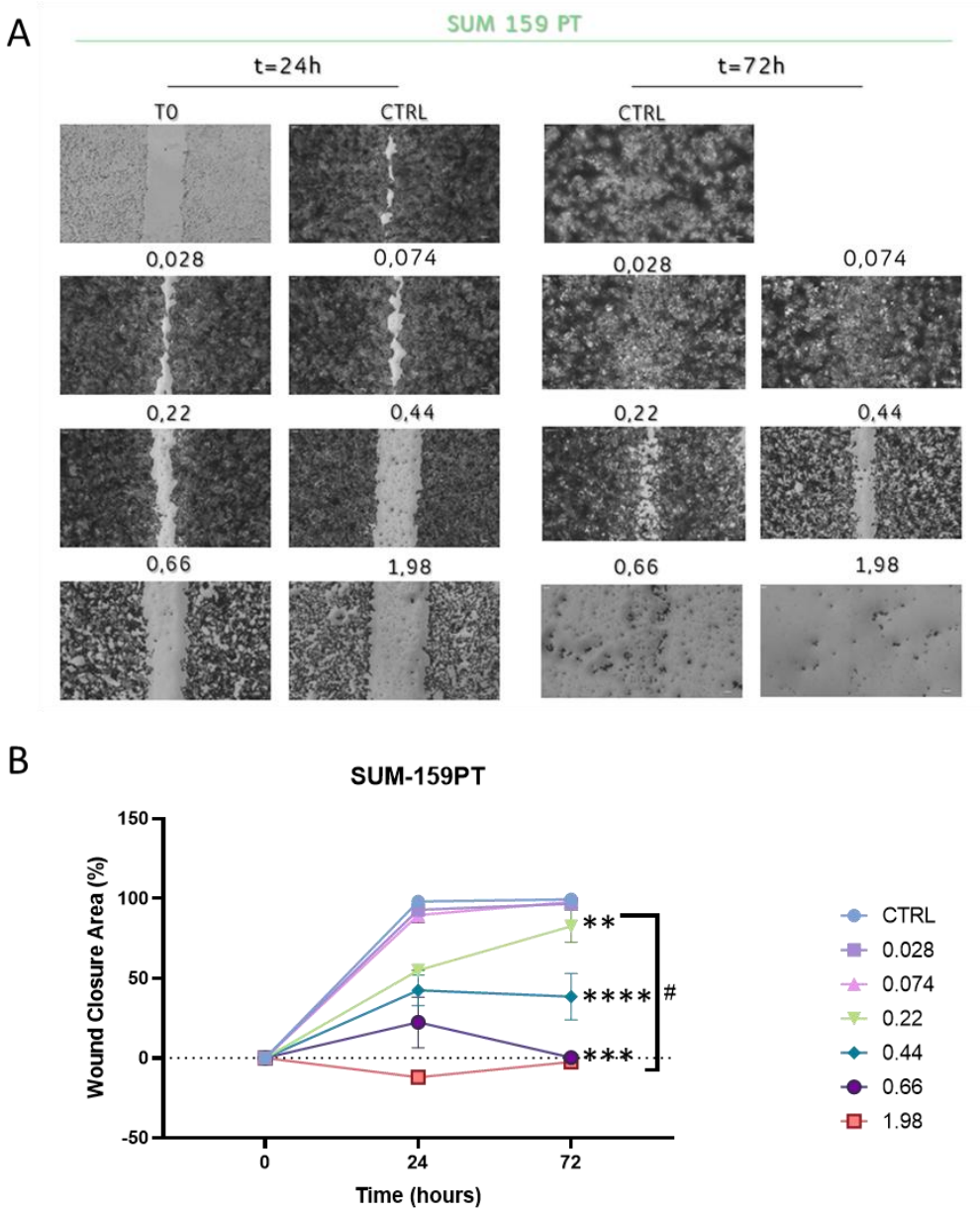

Figure 28. A1 treatment significantly reduces cell migration. *(A) SUM-159PT cells migration by scratch wound healing assay, performed as described in materials and methods. SUM-159PT cells were cultured without (CTRL) or with different A1 concentrations (0.028 - 1.98 mg/mL) and subsequently migration was analysed at 24 and 72 hours. The image is a representative result. (B) Value bars in the graph represents the mean ± SEM of three independent experiments, in duplicate. The analysis was performed by two-way ANOVA with Dunnett's multiple comparisons test with **p < 0.01, *** p < 0.001 and ****p < 0.0001, and Bonferroni's test with #p < 0.05 A1 0.22 mg/mL vs 1.98 mg/mL. Scale bar = 100 µm.*

Since migration and invasion represent sequential and closely related steps in the metastatic cascade, we next investigated A1 effect on the invasive capacity of TNBC cells using a Matrigel-coated *Transwell*® assay, which reproduces the physical barrier that tumour cells must overcome during tissue invasion *in vivo*. As demonstrated in **Figure 29**, control groups of both cells efficiently invaded the matrix, with an average of 2900 invading cells in MDA-MB-231 (**Figure 29A**) and 480 in SUM-159PT (**Figure 29B**) – consistent with the respective invasive behaviour previously described. In contrast, a 5 hours treatment with A1 reduced the number of invading cells in both lines (**Figure 29C**). In particular, treatment with 0.22 mg/mL A1 reduced invasion to 54% in MDA-MB-231 cells, and to 78% in SUM-159PT cells. The higher dose (0.66 mg/mL) produced a more pronounced effect, reducing invasion to 37% in MDA-MB-231 and to 47% in SUM-159PT. Although 0.66 mg/mL substantially impaired invasion in both cell lines, MDA-MB-231 cells displayed higher sensitivity to the lower concentration, showing a marked reduction already at 0.22 mg/mL. Conversely, SUM-159PT cells required the higher dose to achieve a comparable degree of invasion inhibition, suggesting cell line-specific differences in responsiveness to A1 treatment.

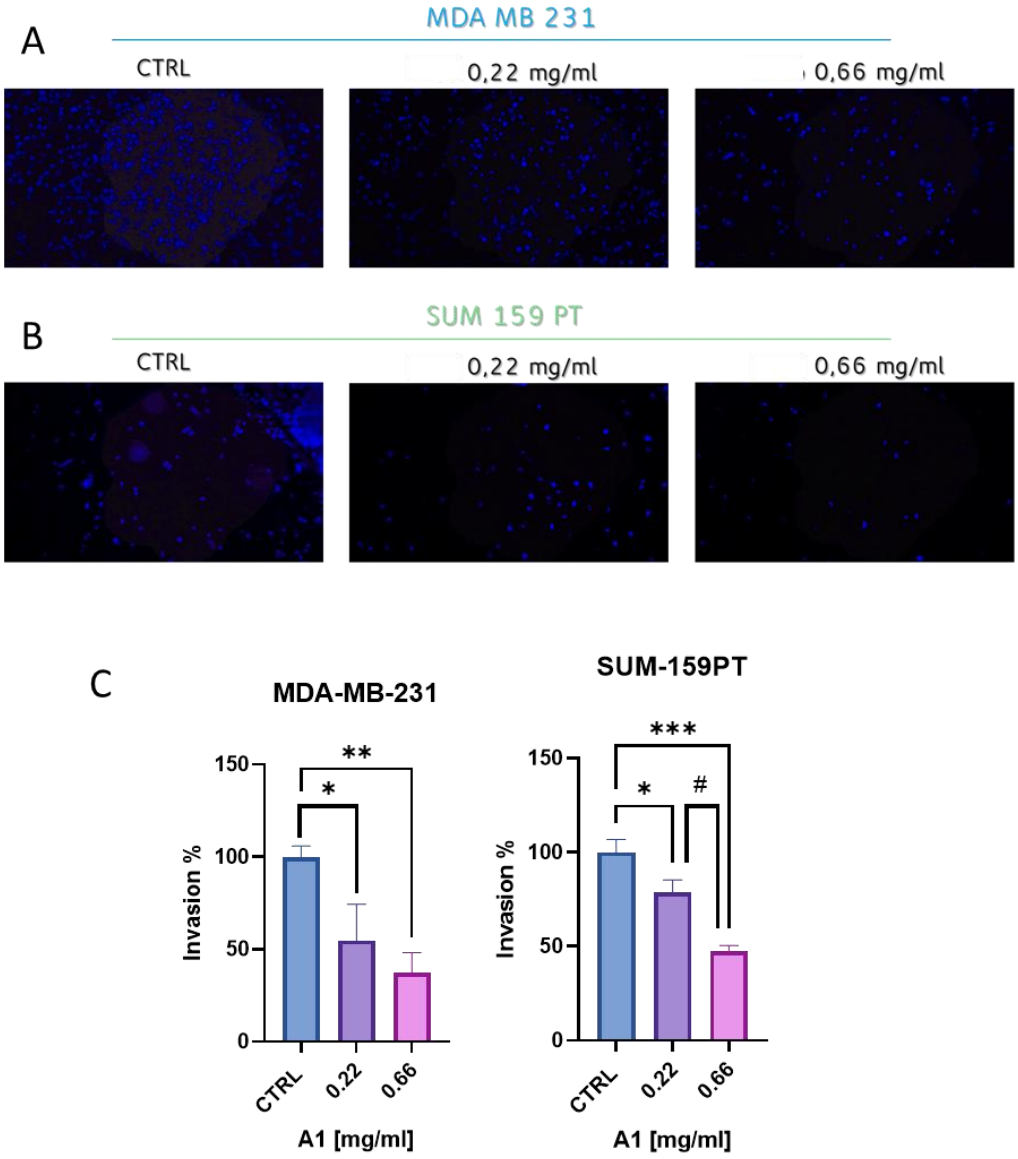

Figure 29. Transwell® invasion assay after five hours of migration. *Representative fluorescence images of invading nuclei (Hoecst) in (A) MDA-MB-231 and (B) SUM-159PT cells treated with increasing concentrations of A1. (C) Quantification of invasion, expressed as percentage relative to control. Value bars in the graph represents the mean ± SEM of three independent experiments, in duplicate. The analysis was performed by one-way ANOVA with Dunnett's multiple comparisons test with **p < 0.01, ***p < 0.001, and Bonferroni's test with #p < 0.05 A1 0.22 mg/mL vs 0.66 mg/mL. Scale bar = 100 µm.*

Taken together, these results confirm that A1 markedly impairs the invasive capacity of TNBC cells, along with its anti-migratory and cytotoxic effects thus prompting further investigation in 3D model. This further analysis is necessary as 3D models more closely mimic the *in vivo* tumour microenvironment compared to conventional 2D monolayer cultures, providing a more physiologically relevant context in which to validate these findings.

5.2. Impact of A1 on 3D spheroids viability and invasion

To assess the ability of A1 to affect cell viability within a 3D, compact cellular mass that better recapitulates the *in vivo* physiological conditions, the CellTiter-Glo® and the LIVE/DEAD assays were performed on both MDA-MB-231 and SUM-159PT spheroids.

The first assay (**Figure 30**) provided a complete overview of A1 cytotoxic effect at different concentrations on MDA-MB-231 and SUM-159PT spheroids. A noticeable reduction in spheroid viability was observed in both cell lines at 24 hours, with a significant decrease starting from 0.22 mg/mL (**Figure 30A and C**), reaching 65% in MDA-MB-231 cells and 55-60% in SUM-159PT cells. This inhibitory effect became markedly more pronounced at 72 hours in both cell lines (**Figure 30B and D**), with viability dropping to approximately 45% at 0.22 mg/mL and below 25% at 0.66 and 1.98 mg/mL in both cell lines.

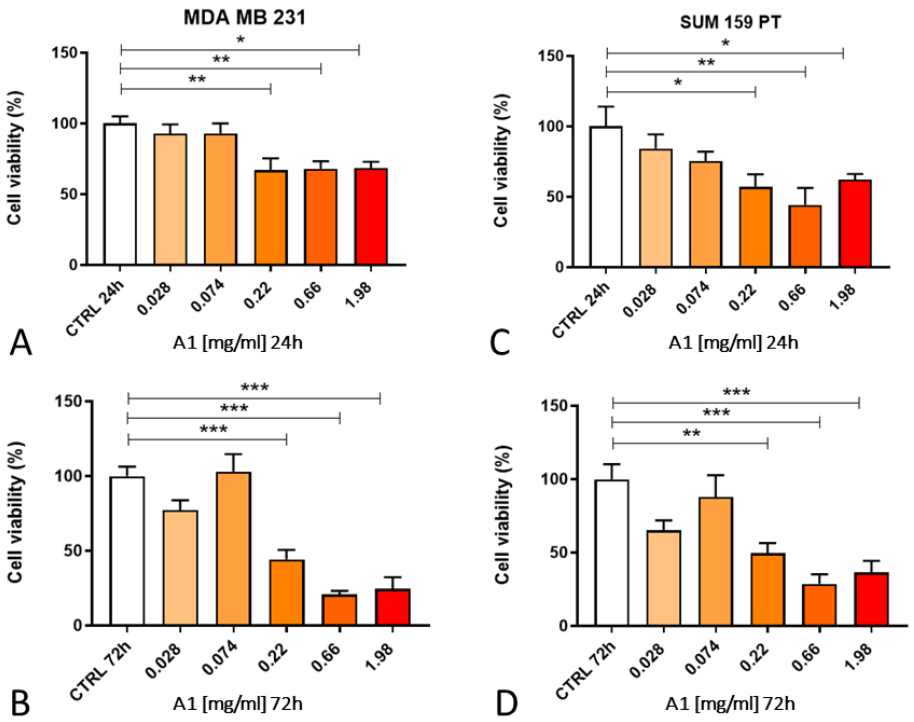

Figure 30. Cell viability on 3D spheroids of MDA-MB-231 and SUM-159PT treated with A1. *Cell viability analysis was assessed using the CellTiter-Glo® assay after treatment with different concentrations of A1 (from 0.028 to 1.98 mg/mL) after 24 and 72 hours in (A-B) MDA-MB-231, and (C-D) SUM-159PT. Value bars in the graph represents the mean ± SEM of three independent experiments, in duplicate. The analysis was performed by two-way ANOVA with Dunnett's multiple comparisons test with *p < 0.05, **p < 0.01, ***p < 0.001.*

Complementing the quantitative data obtained from the CellTiter-Glo® assay, the LIVE/DEAD assay offered a qualitative perspective of cell viability within the 3D spheroid structure. Specifically, control spheroids from both cell lines displayed a compact morphology with a predominantly green signal (living cells), confirming a high baseline viability. Treatment with A1, instead, induced a clear increase in PI-positive staining (dead cells) accompanied by a corresponding reduction and fragmentation of the Calcein-AM signal, indicating progressive loss of cell viability. This effect was already evident at 0.22 mg/mL and

became more pronounced at 0.66 mg/mL, where spheroids also showed a loss of structural compactness, particularly in MDA-MB-231 cells (**Figure 31A**). These results are consistent with the cytotoxicity data previously obtained through the MTT and ATP-based viability assays, further supporting the anti-tumour activity of A1 in TNBC spheroid models.

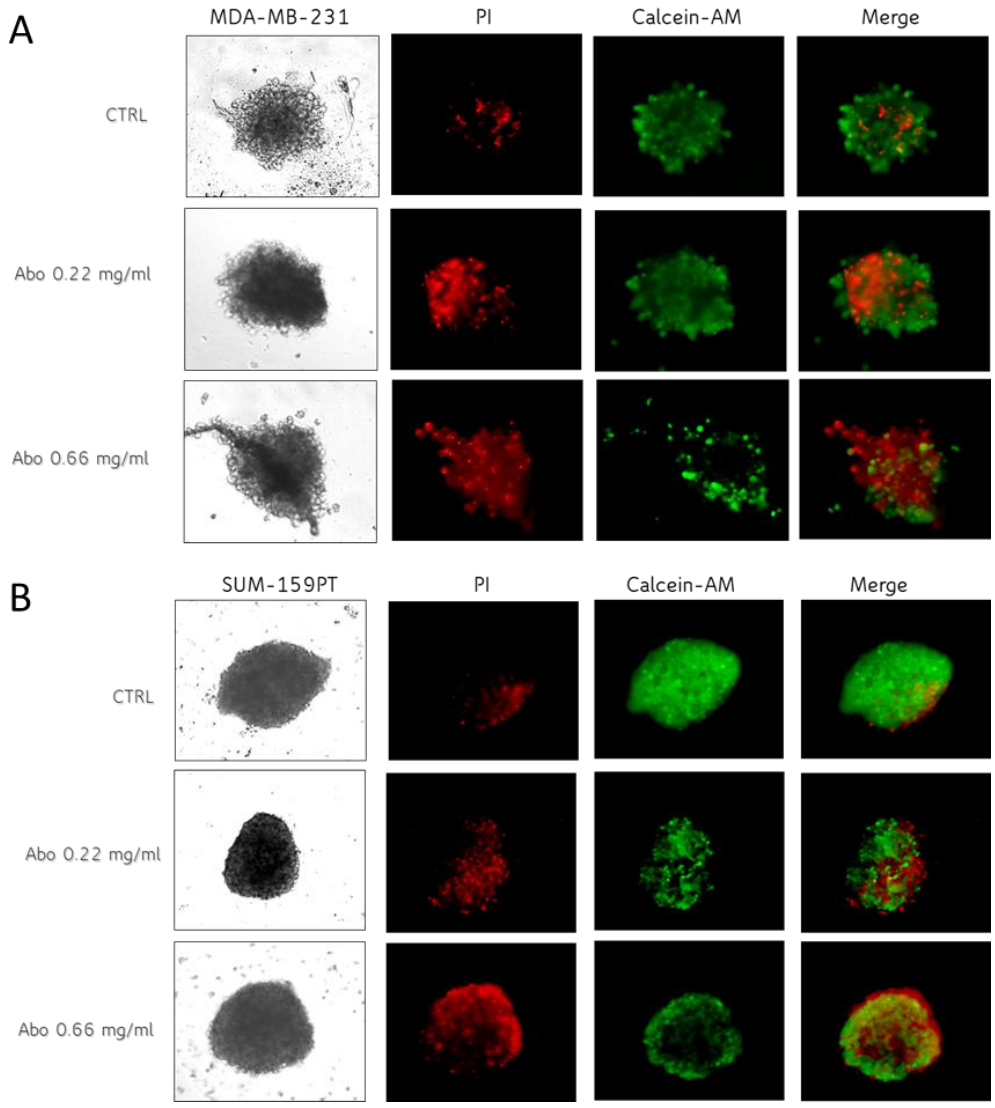

Figure 31. Cell death analysis in MDA-MB-231 and SUM-159PT 3D spheroids treated with A1. *Representative fluorescence microscopy images of 3D spheroids treated with A1 in MDA-MB-231 (A) and SUM-159PT (B) TNBC cells.*

These findings confirm that the cytotoxic activity of A1, initially observed in 2D assays, is successfully translated to a 3D spheroid model, reinforcing its relevance as a potential anti-tumour agent in a more physiologically representative context.

We next investigated whether A1 could also influence the invasive behaviour of MDA-MB-231 and SUM-159PT cells cultured as 3D spheroids. For this purpose, a 3D spheroids invasion assay was performed, and a direct correlation between A1 treatment and the formation of invasive protrusions emerged. After 72 hours, control MDA-MB-231 spheroids (CTRL) showed a marked invasive phenotype, as evidenced by the formation of branching structures into the extracellular matrix (**Figure 32A**). Conversely, SUM-159PT control spheroids displayed a proliferative phenotype (**Figure 33A**), characterized by a group of cells expanding outward from the spheroid core into the adjacent matrix, indicating migratory capacity. Treatment with A1 progressively suppressed this invasive front. Indeed, at lower concentrations (0.028 mg/mL and 0.074 mg/mL), no inhibitory effect was detected, with branching structures still clearly observable, similar to control. By contrast, a concentration of 0.22 mg/mL results in a partial decrease in the peripheral invasive front, but the effect is more notable at 0.66 and 1.98 mg/mL where the outer invasive front is no longer visible. To corroborate the qualitative observations, a quantitative image analysis was performed (**Figure 32B and 33B**). Our data showed a marked reduction starting from the intermediate concentrations and minimal invasion detected at 1.98 mg/mL. Interestingly, a lower invasive behaviour was observed in SUM-159PT spheroids compared to their MDA-MB-231 counterparts, a finding that aligns with the previously reported data by Westcott et al. (2015). Hence, the difference in invasive capacity between the two lines likely reflects the degree of intratumoral heterogeneity with respect to invasion

competence, with SUM-159PT spheroids being functionally constrained by the limited proportion of "trailblazer" cells capable of initiating collective invasion.

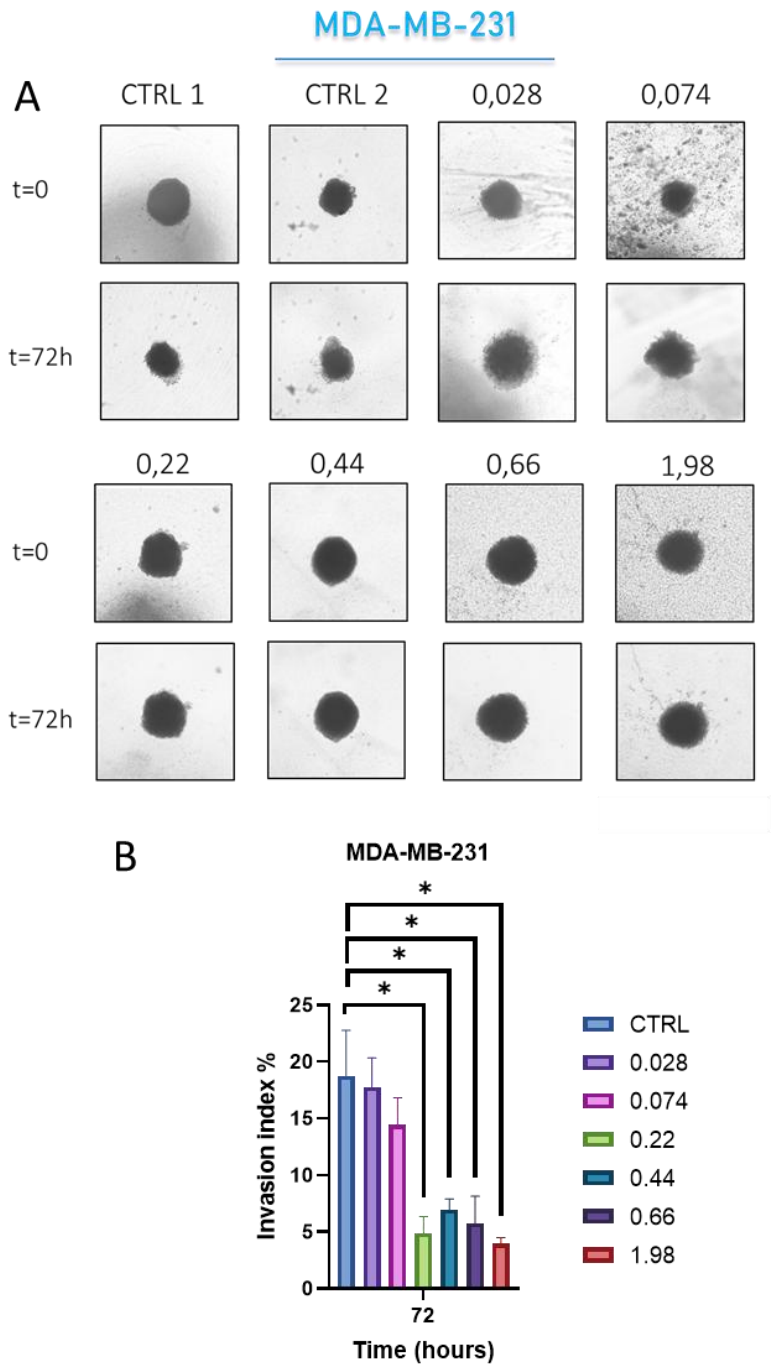

Figure 32. Effect of A1 on spheroid invasive morphology. *(A) MDA-MB-231 spheroids embedded within an extracellular matrix were monitored by brightfield microscopy immediately after embedding (T0) and*

*following a 72 hours exposure to A1, with untreated samples (CTRL) included for comparison. (B) The extent of spheroid invasion was measured across a range of A1 concentrations. Value bars in the graph represents the mean ± SEM of four independent experiments, in duplicate. The analysis was performed by one-way ANOVA with Dunnett's multiple comparisons test with *p < 0.05. Scale bar = 100 µm.*

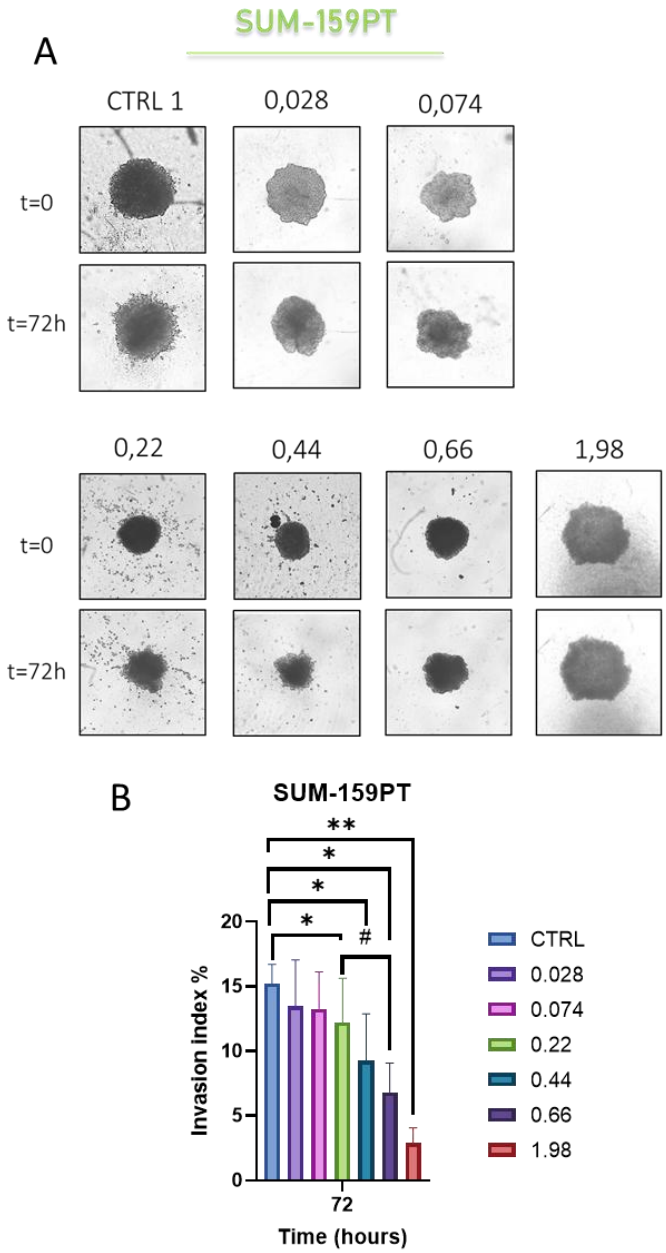

Figure 33. *Effect of A1 on spheroid invasive morphology. (A) SUM-159PT spheroids embedded within an extracellular matrix were monitored by brightfield microscopy immediately after embedding (T0) and following a*

*72 hours exposure to A1, with untreated samples (CTRL) included for comparison. (B) The extent of spheroid invasion was measured across a range of A1 concentrations. (B) Quantitative analysis of spheroid invasion at increasing concentrations. Value bars in the graph represents the mean ± SEM of three independent experiments, in duplicate. The analysis was performed by one-way ANOVA with Dunnett's multiple comparisons test with *p < 0.05 and **p < 0.01, and Bonferroni's test with #p < 0.05 A1 0.22 mg/mL vs 0.66 mg/mL. Scale bar = 100 µm.*

These results were further confirmed by the Apricell 3-in-1 Plate model (**Figure 34**), where spheroids were treated only with A1 at the optimal concentration of 0.22 mg/mL. In both MDA-MB-231 (**Figure 34A**) and SUM-159PT spheroids (**Figure 34B**), the control conditions showed numerous cells dispersed within the channel surrounding the spheroid core, consistent with an invasive phenotype. Following treatment with A1 (0.22 mg/mL), spheroids of both cell lines displayed a more compact, rounded morphology, with fewer cells detaching from the core and migrating into the surrounding channel. These observations closely align with the concentration-dependent inhibition of invasion described above, further supporting the quantitative analysis that demonstrated a progressive reduction in invasive and proliferative behaviour upon A1 treatment in both cell lines.

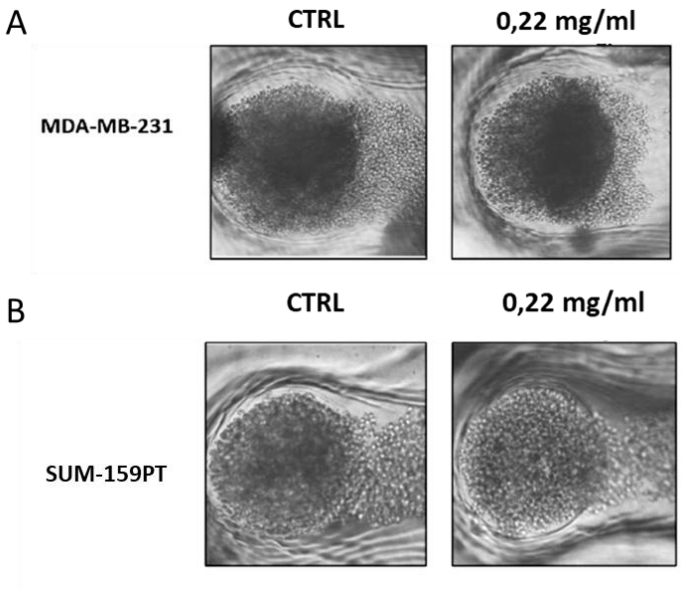

Figure 34. 3D invasion in MDA-MB-231 and SUM-159PT TNBC cells with Apricell technology. *Representative brightfield images showing spheroid invasion/proliferation of (A) MDA-MB-231 and (B) SUM-159PT cell lines at 72 hours, in control conditions (CTRL) and following treatment with A1 (0.22 mg/mL).*

5.3. Impact of A1 on RACK1 expression in TNBC cell lines

Considering the central role of RACK1 as a scaffold protein involved in the regulation of cell proliferation and migration of TNBC cells, we next investigated whether A1 treatment could modulate its expression in MDA-MB-231 and SUM-159PT cell lines. The western blot analysis showed a noticeable reduction of RACK1 expression in treated cells compared to the untreated control groups after 24 hours (**Figure 35**). In particular, both cell lines undergo a significant reduction starting from the lowest concentration tested (0.22 mg/mL). A more pronounced and statistically robust decrease was observed at 0.66 and 1.98 mg/mL, reaching a near-complete suppression of RACK1 expression at the highest dose. This analysis correlates with previous viability and migration data, and confirms the ability of A1 to impair key oncogenic processes in TNBC, further supporting its relevant anti-tumour activity.

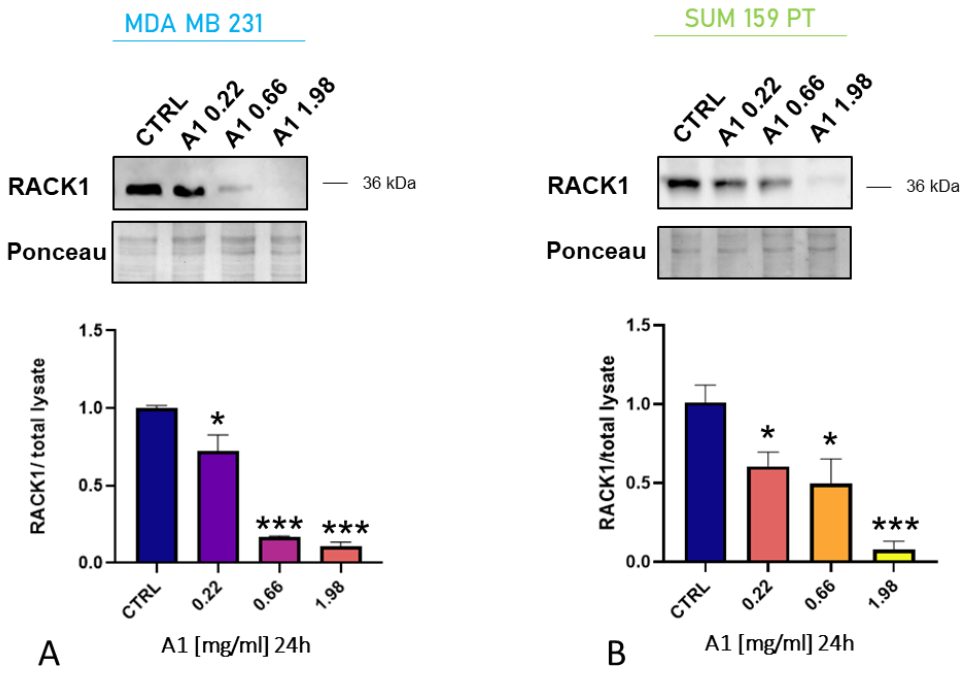

Figure 35. Western blot analysis of RACK1. *To evaluate whether A1 treatment affects RACK1 protein levels, MDA-MB-231 (A) and SUM-159PT (B) cells were treated with increasing concentrations of A1 (0.22, 0.66, and 1.98 mg/mL) for 24 hours, and RACK1 expression was assessed by western blot analysis. Value bars in the graph represents the mean ± SEM of three independent experiments, in duplicate. The analysis was performed with Dunnett's multiple comparisons test with *p < 0.05 and ***p < 0.001.*

5.4. Effect of A1 on THP-1 recruitment towards TNBC-conditioned medium

To verify that THP-1 cells were responsive to LPS stimulation, cells were treated with two different LPS concentrations (10 and 100 ng/mL), and activation of the NF-κB signalling pathway was assessed by western blot. As shown in **Figure 36**, nuclear translocation of NF-κB p50 was detected following LPS treatment at both concentrations, using Lamin as a nuclear loading control. It is evident that nuclear p50 levels increased following LPS treatment, with the highest concentration (100 ng/mL) inducing a significant increase in the p50/Lamin ratio compared to the control.

This confirmed that THP-1 cells correctly recognized and responded to the stimulus, supporting the assumption that THP-1 cells were not only viable but fully functional, providing a reliable basis for the subsequent migration assays.

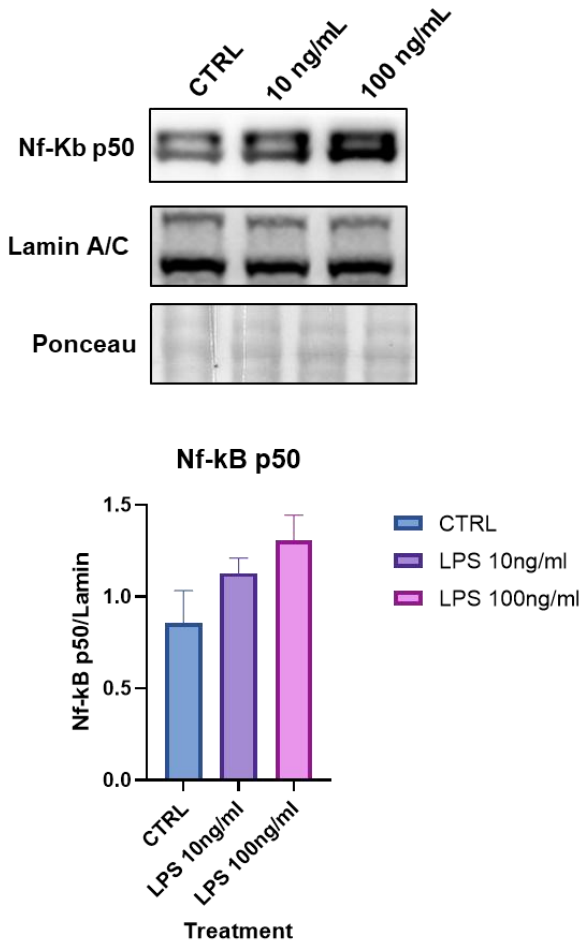

Figure 36. LPS induces nuclear translocation of NF-κB subunits p50 and p65. *Western blot analysis of nuclear (A) NF-κB p50 and (B) NF-κB p65 protein levels after 1.5 hours of treatment with LPS 10 ng/ml or LPS 100 ng/ml. Lamin was used as a nuclear loading control. Data represent a single experiment (n = 1 per condition); no statistical analysis was performed due to the absence of biological replicates.*

Then, a *Transwell*® invasion assay was performed to assess THP-1 recruitment towards the lower chamber, which contained conditioned

medium from control and A1-treated conditions. The conditioned medium was previously collected from the wound healing assays and used to specifically assess the contribution of paracrine signalling mediated by tumour cell-secreted soluble factors, which is independent of direct cell-cell contact. For this assay, only the A1 concentrations previously shown to exert a biologically relevant effect were included (0.22, 0.44, and 0.66 mg/mL). The lowest concentrations (0.028 and 0.074 mg/mL) were excluded as they had no detectable effect, whereas the highest concentration (1.98 mg/mL) was excluded due to excessive cytotoxicity. In the MDA-MB-231 setting (**Figure 37A**), representative images of Hoecst-stained invaded THP-1 cells showed a visibly dense population of nuclei in the control condition, which progressively decreased with increasing A1 concentrations, becoming markedly sparse at 0.44 and 0.66 mg/mL. This qualitative observation was confirmed by quantification (**Figure 37B**), with THP-1 invasion reduced from 100% in the CTRL condition to 55%, 41%, and 36% at 0.22, 0.44, and 0.66 mg/mL A1, respectively, indicating a clear inhibitory effect.

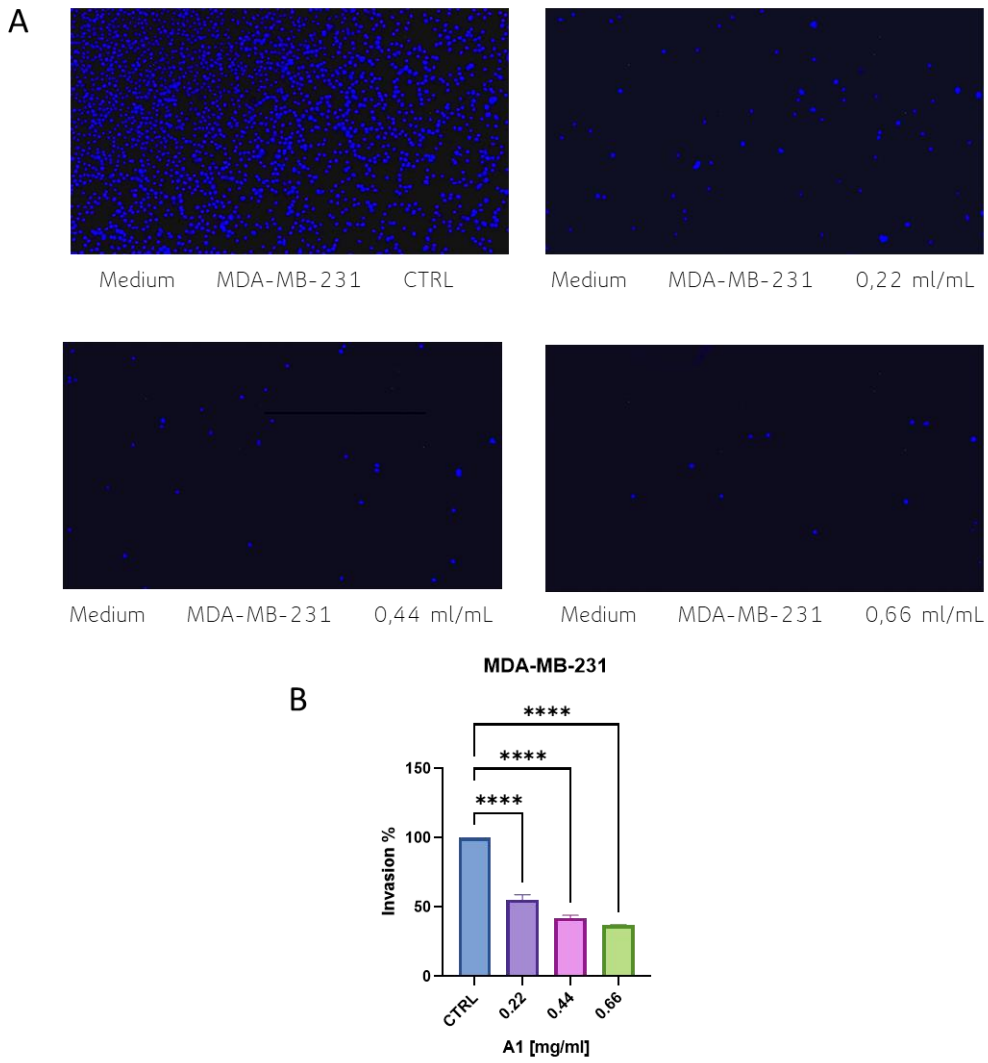

Figure 37. Representative fluorescence microscopy images of Hoecst-stained THP-1 nuclei after 24 hours of migration. *(A) A1 reduces THP-1 invasion towards MDA-MB-231 cells conditioned medium. (B) Quantification of THP-1 invasion, expressed as percentage relative to CTRL (set at 100%). Value bars in the graph represents the mean ± SEM of four independent experiments, in duplicate. The analysis was performed by one-way ANOVA with Dunnett's multiple comparisons test with ****p < 0.0001. Scale bar = 100 µm.*

A similar trend was observed in the SUM-159PT setting (**Figure 38A**), although the magnitude of the reduction was less pronounced compared to MDA-MB-231. Representative images showed a comparatively modest decrease in the density of invaded THP-1 nuclei across increasing A1

concentrations. Quantitatively (**Figure 38B**), invasion percentages decreased from 100% in the control condition to 74%, 67%, and 63% at 0.22, 0.44, and 0.66 mg/mL A1, respectively. Taken together, these results show that A1 treatment reduces THP-1 recruitment towards both TNBC cell lines, with a more pronounced inhibitory effect observed in the MDA-MB-231 model compared to SUM-159PT.

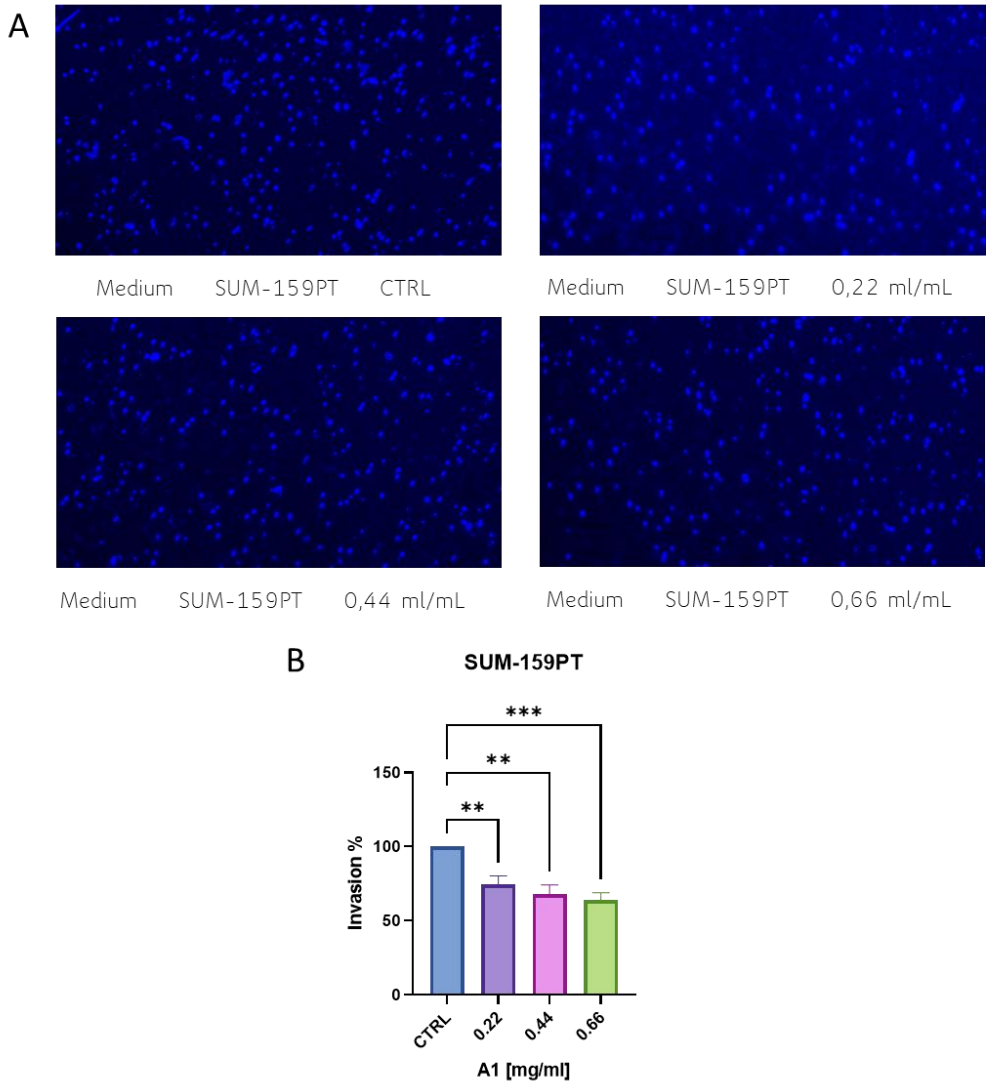

Figure 38. Representative fluorescence microscopy images of Hoecst-stained THP-1 nuclei after 24 hours of migration. *(A) A1 reduces THP-1 invasion towards SUM-159PT cells conditioned medium. (B) Quantification of THP-1 invasion, expressed as percentage relative to CTRL (set at 100%). Value bars in the graph represents the mean ± SEM of four independent experiments, in duplicate. The analysis was performed*

*by one-way ANOVA with Dunnett's multiple comparisons test with **p < 0.01 and ***p < 0.001. Scale bar = 100 µm.*

Comparable results were obtained by directly seeding MDA-MB-231 in the lower chamber, an experimental setup that further confirmed our previous findings. Specifically, a clear reduction was observed, with THP-1 cell recruitment progressively decreasing at 0.22 mg/mL and becoming drastically suppressed at the higher concentrations of 0.44 and 0.66 mg/mL (**Figure 39**). These findings should be considered preliminary, as they are based on initial experiments and require further validation with additional biological replicates.

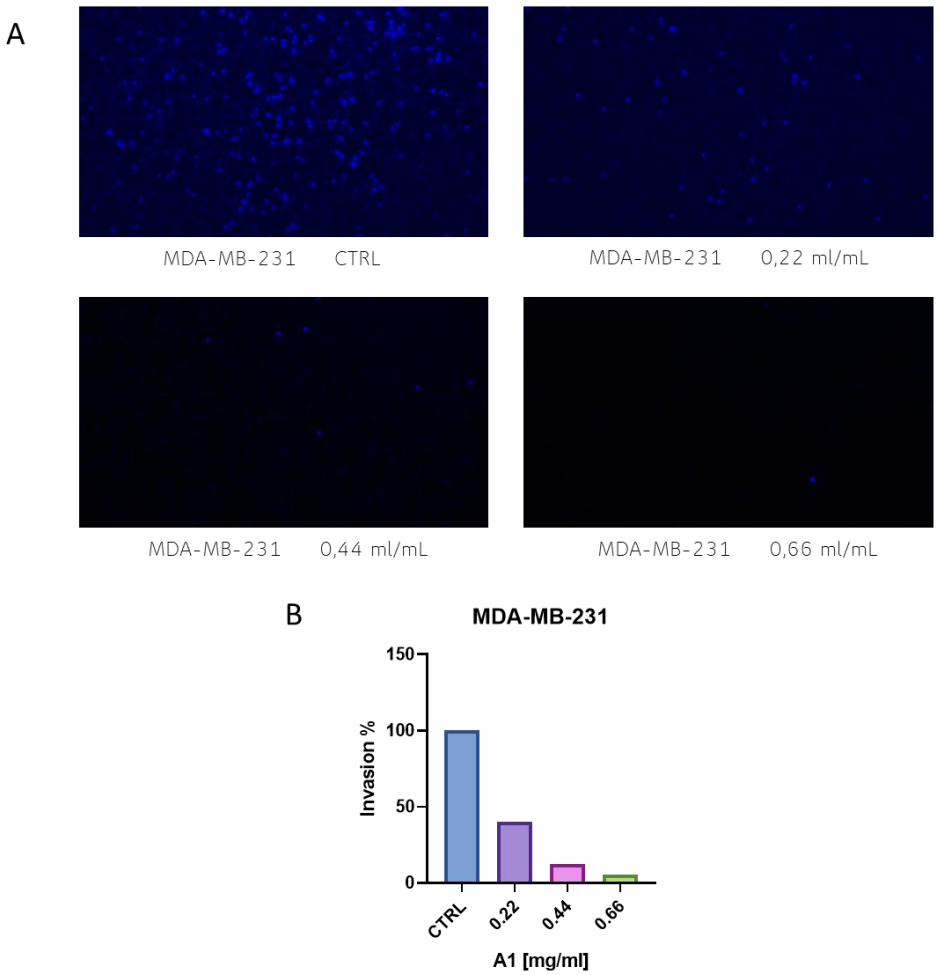

Figure 39. Representative fluorescence microscopy images of Hoecst-stained THP-1 nuclei after 24 hours of migration. *(A) A1 reduces THP-1 invasion towards TNBC cells. (B) Quantification of THP-1 invasion, expressed as percentage relative to CTRL (set at 100%). Data represent a single experiment (n = 1 per condition); no statistical analysis was performed due to the absence of biological replicates. Scale bar = 100 µm.*

We next investigated the effect of A1 on THP-1-derived macrophages (M0) to define if the treatment also reduced the recruitment of polarized macrophages. For this experiment, only MDA-MB-231 cells were used, as this cell line had shown the most consistent responsiveness to A1 treatment in the previous assays. Additionally, only an intermediate A1 concentration (0.44 mg/mL) was tested, and this choice was based on the

relevant anti-invasive effect observed at this concentration in earlier experiments, combined with the absence of significant cytotoxicity. To assess macrophage recruitment, THP-1-derived macrophages were exposed to fresh medium supplemented with LPS (1 μg/mL), used as a positive control, or to conditioned medium from untreated MDA-MB-231 cells (CTRL). Both control conditions induced a comparable degree of macrophage migration, indicating that tumour-derived factors attract macrophages as effectively as the LPS stimulus. When compared to both controls, representative images (**Figure 40A**) revealed a significantly lower number of migrated macrophages in the presence of conditioned medium from A1-treated MDA-MB-231 cells (0.44 mg/mL). Quantification of nuclei counts confirmed this observation, showing a reduction in macrophage migration to 42% relative to control upon treatment with A1 at 0.44 mg/mL (**Figure 40B**). These data suggest that A1 treatment of MDA-MB-231 cells reduces their ability to recruit macrophages, in addition to its previously observed anti-invasive effect on tumour cells themselves. As this experiment was performed once, these findings should be considered preliminary and would require confirmation in independent replicates.

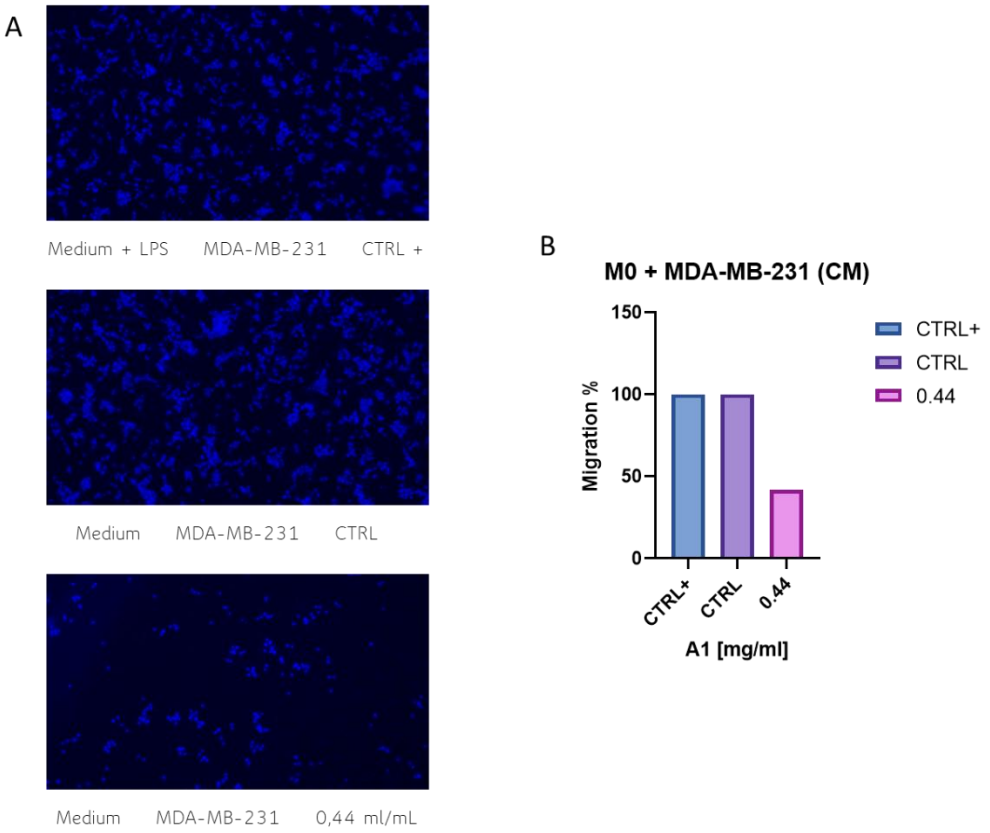

Figure 40. Recruitment of M0 macrophages by MDA-MB-231-conditioned medium and effect of A1 treatment. *(A) Representative fluorescence microscopy images of Hoecst-stained M0 macrophage nuclei that migrated through the Transwell® membrane in response to conditioned medium (CM) from untreated and treated MDA-MB-231 cells. (B) Quantification of macrophage migration, expressed as percentage relative to control (CTRL+ and CTRL set as 100%). Data represent a single experiment (n = 1 per condition); no statistical analysis was performed due to the absence of biological replicates. Scale bar = 100 µm.*

5.5. Effect of A1 on M0 macrophage polarization

Lastly, to determine whether A1 treatment influences the polarization state of THP-1-derived M0 macrophages, cells were analysed by flow cytometry for the expression of CD86 (M1-like marker) and CD206 (M2-like marker). Gates for CD86+ and CD206+ populations were defined within the P3 gate, and background positivity was assessed using an

unstained control (**Figure 41**), which showed 4.24% of events within the CD86 gate and 2.23% within the CD206 gate, reflecting the contribution of autofluorescence and non-specific signal to each gate.

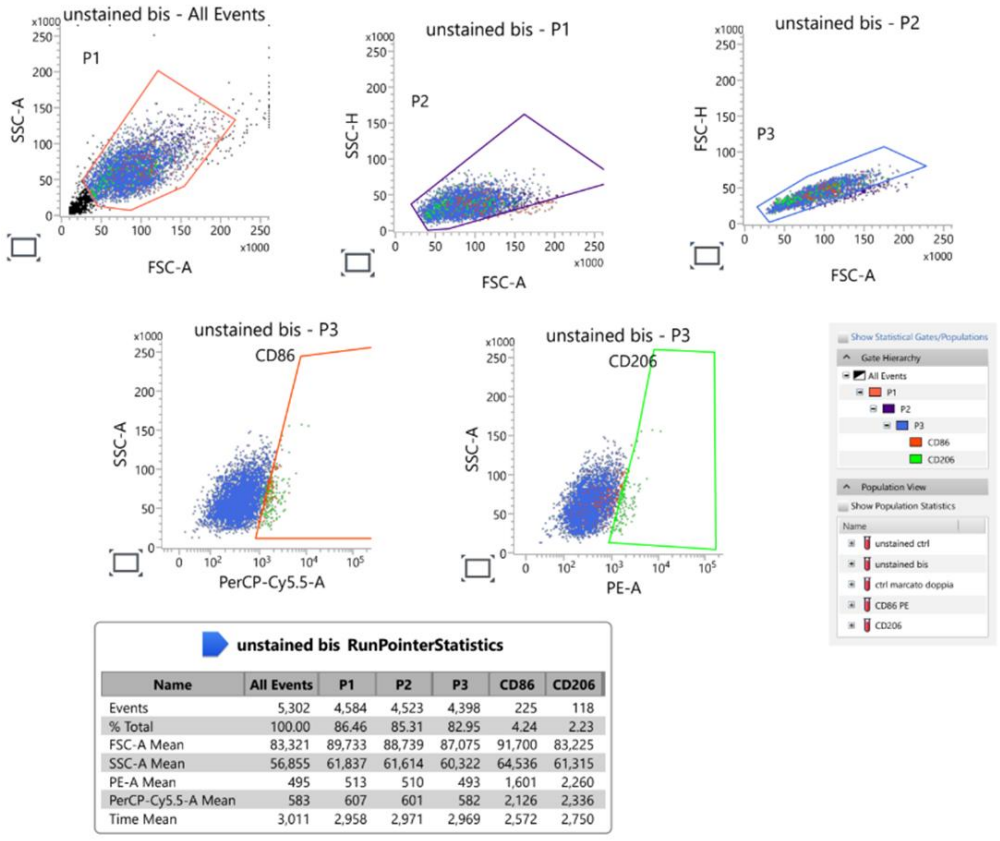

unstained bis RunPointerStatistics

Name	All Events	P1	P2	P3	CD86	CD206
Events	5,302	4,584	4,523	4,398	225	118
% Total	100.00	86.46	85.31	82.95	4.24	2.23
FSC-A Mean	83,321	89,733	88,739	87,075	91,700	83,225
SSC-A Mean	56,855	61,837	61,614	60,322	64,536	61,315
PE-A Mean	495	513	510	493	1,601	2,260
PerCP-Cy5.5-A Mean	583	607	601	582	2,126	2,336
Time Mean	3,011	2,958	2,971	2,969	2,572	2,750

Figure 41. Unstained control for flow cytometric analysis of M0 macrophage polarization markers. *Dot plot showing background positivity within the CD86 and CD206 gates in the absence of antibody staining, used to correct for autofluorescence and non-specific signal in the corresponding stained samples.*

In the untreated control (**Figure 42A**), 5.99% of events fell within the CD86 gate and 3.73% within the CD206 gate. Following A1 treatment (**Figure 42B**), the proportion of CD86+ events increased markedly to 13.42% of the total P3 population, representing a marked increase relative to the untreated control and reflecting a visible expansion of the CD86+ population in the corresponding dot plot. The CD206+ population, by

contrast, remained small in both conditions, increasing only marginally from 3.73% in the control to 4.08% in treated cells. Taken together, these preliminary data indicate that A1 treatment may promote a shift of M0 macrophages toward a CD86-dominant, M1-like phenotype, without a comparable induction of CD206 expression.

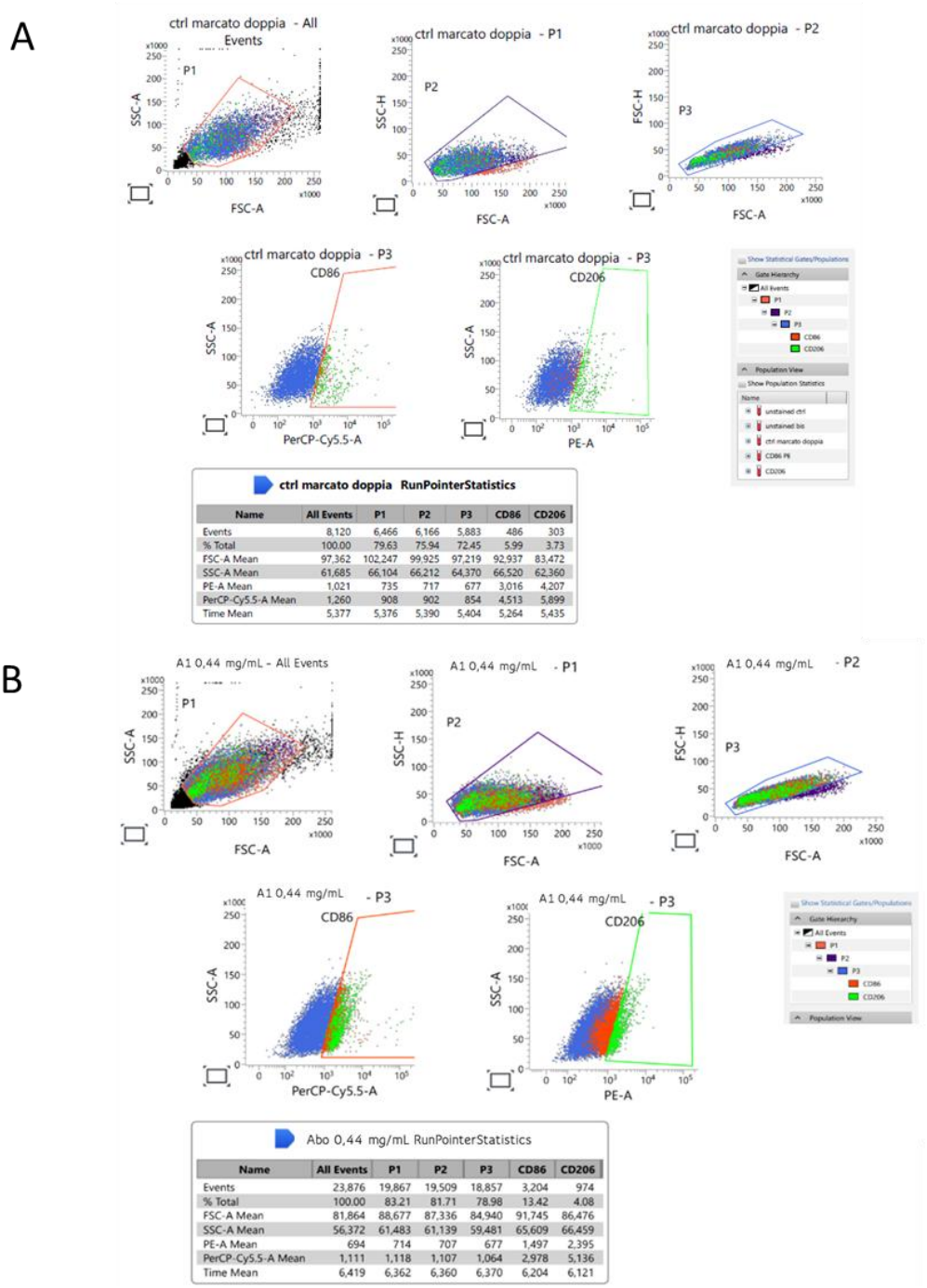

Name	All Events	P1	P2	P3	CD86	CD206
Events	8,120	6,466	6,166	5,883	486	303
% Total	100.00	79.63	75.94	72.45	5.99	3.73
FSC-A Mean	97,362	102,247	99,925	97,219	92,937	83,472
SSC-A Mean	61,685	66,104	66,212	64,370	66,520	62,360
PE-A Mean	1,021	735	717	677	3,016	4,207
PerCP-Cy5.5-A Mean	1,260	908	902	854	4,513	5,899
Time Mean	5,377	5,376	5,390	5,404	5,264	5,435

Name	All Events	P1	P2	P3	CD86	CD206
Events	23,876	19,867	19,509	18,857	3,204	974
% Total	100.00	83.21	81.71	78.98	13.42	4.08
FSC-A Mean	81,864	88,677	87,336	84,940	91,745	86,476
SSC-A Mean	56,372	61,483	61,139	59,481	65,609	66,459
PE-A Mean	694	714	707	677	1,497	2,395
PerCP-Cy5.5-A Mean	1,111	1,118	1,107	1,064	2,978	5,136
Time Mean	6,419	6,362	6,360	6,370	6,204	6,121

Figure 42. Flow cytometric analysis of CD86 and CD206 expression in control and A1-treated M0 macrophages. *(A) Dot plots showing CD86+ and CD206+ populations, expressed as a percentage of the P3 gate, in untreated (control) and (B) A1-treated (0.44 mg/mL) M0 macrophages. A1 treatment increased the proportion of CD86+ events compared to control, while the CD206+ population remained comparable between the two conditions.*

6. DISCUSSION AND CONCLUSION

The therapeutic management of TNBC remains an outstanding clinical challenge due to its intrinsic aggressiveness, high propensity for metastatic dissemination, and the lack of targeted therapeutic options. Consequently, the identification of novel compounds capable of simultaneously targeting tumour cell aggressiveness and TME is of considerable therapeutic interest.

In the present study, we demonstrated that the natural extract A1 exerts a broad anti-tumour activity across two distinct TNBC cell models, effectively disrupting multiple hallmarks of tumour progression, including cell viability, migration, invasion, and macrophage recruitment. Furthermore, our findings suggest that these biological effects are strictly associated with a marked downregulation of the scaffolding protein RACK1, a well-established master regulator of signalling pathways that drive cancer progression and metastatic cell motility. Beyond its direct inhibitory effects on tumour cells, A1 also targets tumour-immune interactions within the stroma. Conditioned medium derived from A1-treated TNBC cells significantly compromised THP-1 monocyte recruitment, suggesting that A1 actively modulates the secretome of tumour cells by downregulating specific tumour-derived chemoattractants involved in monocyte trafficking. Given that tumour-associated macrophages (TAMs) are major promoters of tumour progression, angiogenesis, immune suppression, and secondary dissemination, limiting their recruitment into the neoplastic niche may represent an additional, crucial mechanism contributing to the overall anti-tumour activity of A1. Furthermore, our preliminary experiments demonstrated a direct reduction in mature macrophage recruitment, alongside an intriguing phenotypic shift of resting M0 macrophages toward a CD86-positive, M1-like anti-tumour configuration. Although these immunological observations require

further validation in independent biological replicates, they raise the compelling hypothesis that A1 not only suppresses intrinsic tumour aggressiveness but may also reprogram the surrounding stroma to foster a more anti-tumour immune microenvironment. Several limitations should nevertheless be acknowledged. First, the molecular mechanisms linking A1 treatment to RACK1 downregulation remain to be elucidated.

Future studies should determine whether A1 directly regulates RACK1 transcription, protein stability, or upstream signalling pathways controlling its expression. Second, the immunological findings are preliminary and require confirmation using additional biological replicates together with a broader characterization of macrophage polarization through complementary markers and cytokine profiling. Finally, although 3D spheroid models provide a substantially improved representation of tumour biology compared with two-dimensional cultures, *in vivo* validation will be essential to determine whether the anti-tumour and immunomodulatory effects of A1 translate into reduced tumour growth and metastatic dissemination.

In conclusion, this study demonstrates that A1 exerts a multi-target anti-tumour activity against TNBC by simultaneously impairing cell proliferation, migration, invasion, and tumour-associated macrophage recruitment while reducing RACK1 expression. The ability of A1 to retain these effects in advanced three-dimensional models further supports its potential therapeutic relevance. Collectively, these findings identify A1 as a promising natural compound deserving further mechanistic investigation and *in vivo* validation, with RACK1 emerging as a potential molecular mediator of its anti-cancer activity.

BIBLIOGRAPHY

Adams DR, Ron D, Kiely PA. RACK1, a multifaceted scaffolding protein: structure and function. Cell Commun Signal. 2011;9:22. doi:10.1186/1478-811X-9-22. PMID: 21978545; PMCID: PMC3193196.

Barnabas N, Cohen D. Phenotypic and Molecular Characterization of MCF10DCIS and SUM Breast Cancer Cell Lines. Int J Breast Cancer. 2013;2013: 872743. doi: 10.1155/2013/872743. Epub 2013 Jan 16. PMID: 23401782; PMCID: PMC3562669.

Buoso E, Galasso M, Serafini MM, Ronfani M, Lanni C, Corsini E, Racchi M. Transcriptional regulation of RACK1 and modulation of its expression: Role of steroid hormones and significance in health and aging. Cell Signal. 2017 Jul;35:264-271. doi: 10.1016/j.cellsig.2017.02.010. Epub 2017 Feb 9. PMID: 28192162.

Buoso E, Masi M, Galbiati V, Maddalon A, Iulini M, Kenda M, Sollner Dolenc M, Marinovich M, Racchi M, Corsini E. Effect of estrogen-active compounds on the expression of RACK1 and immunological implications. Arch Toxicol. 2020 Jun;94(6):2081-2095. doi: 10.1007/s00204-020-02756-9. Epub 2020 Apr 23. PMID: 32328699.

Buoso E, Masi M, Racchi M, Corsini E. Endocrine-Disrupting Chemicals' (EDCs) Effects on Tumour Microenvironment and Cancer Progression: Emerging Contribution of RACK1. Int J Mol Sci. 2020 Dec 3;21(23):9229. doi: 10.3390/ijms21239229. PMID: 33287384; PMCID: PMC7729595.

Cao XX, Xu JD, Xu JW, Liu XL, Cheng YY, Wang WJ, Li QQ, Chen Q, Xu ZD, Liu XP. RACK1 promotes breast carcinoma proliferation and invasion/metastasis in vitro and *in vivo*. Breast Cancer Res Treat. 2010 Sep;123(2):375-86. doi: 10.1007/s10549-009-0657-x. Epub 2009 Nov 28. PMID: 19946739.

Cao XX, Xu JD, Liu XL, Xu JW, Wang WJ, Li QQ, Chen Q, Xu ZD, Liu XP. RACK1: a superior independent predictor for poor clinical outcome in breast cancer. Int J Cancer. 2010 Sep 1;127(5):1172-9. doi:10.1002/ijc.25120. PMID: 20143388.

Chanput W, Mes JJ, Wichers HJ. THP-1 cell line: an in vitro cell model for immune modulation approach. Int Immunopharmacol. 2014 Nov;23(1):37-45. doi: 10.1016/j.intimp.2014.08.002. Epub 2014 Aug 14. PMID: 25130606.

Chavez KJ, Garimella SV, Lipkowitz S. Triple negative breast cancer cell lines: one tool in the search for better treatment of triple negative breast cancer. Breast Dis. 2010;32(1-2):35-48. doi: 10.3233/BD-2010-0307. PMID: 21778573; PMCID: PMC3532890.

Conner S, Guarin JR, Le TT, Fatherree J, Kelley C, Payne S, Salhany K, McGinn R, Henrich E, Yui A, Parker S, Srinivasan D, Bloomer H, Borges H, Oudin MJ. Cell morphology best predicts tumourigenicity and metastasis *in vivo* across multiple TNBC cell lines of different metastatic potential. bioRxiv [Preprint]. 2023 Jun 14:2023.06.14.544969. doi: 10.1101/2023.06.14.544969. Update in: Breast Cancer Res. 2024 Mar 11;26(1):43. doi: 10.1186/s13058-024-01796-8. PMID: 37398306; PMCID: PMC10312673.

Corsini E, Galbiati V, Papale A, Kummer E, Pinto A, Serafini MM, Guaita A, Spezzano R, Caruso D, Marinovich M, Racchi M. Role of androgens in dhea-induced rack1 expression and cytokine modulation in monocytes. Immun Ageing. 2016 May 29;13:20. doi: 10.1186/s12979-016-0075-y. PMID: 27239218; PMCID: PMC4884617.

Cox EA, Bennin D, Doan AT, O'Toole T, Huttenlocher A. RACK1 regulates integrin-mediated adhesion, protrusion, and chemotactic cell

migration via its Src-binding site. Mol Biol Cell. 2003 Feb;14(2):658-69. doi: 10.1091/mbc.e02-03-0142. PMID: 12589061; PMCID: PMC149999.

Dan H, Liu S, Liu J, Liu D, Yin F, Wei Z, Wang J, Zhou Y, Jiang L, Ji N, Zeng X, Li J, Chen Q. RACK1 promotes cancer progression by increasing the M2/M1 macrophage ratio via the NF-κB pathway in oral squamous cell carcinoma. Mol Oncol. 2020 Apr;14(4):795-807. doi: 10.1002/1878-0261.12644. Epub 2020 Feb 20. PMID: 31997535; PMCID: PMC7138402.

Dass SA, Tan KL, Selva Rajan R, Mokhtar NF, Mohd Adzmi ER, Wan Abdul Rahman WF, Tengku Din TADA, Balakrishnan V. Triple Negative Breast Cancer: A Review of Present and Future Diagnostic Modalities. Medicina (Kaunas). 2021 Jan 12;57(1):62. doi: 10.3390/medicina57010062. PMID: 33445543; PMCID: PMC7826673.

Dias AS, Almeida CR, Helguero LA, Duarte IF. Metabolic Reprogramming of Breast Tumour-Educated Macrophages Revealed by NMR Metabolomics. Cancers (Basel). 2023 Feb 14;15(4):1211. doi: 10.3390/cancers15041211. PMID: 36831553; PMCID: PMC9954003.

Dogan BE, Turnbull LW. Imaging of triple-negative breast cancer. Ann Oncol. 2012 Oct;23 Suppl 6:vi23-vi29. doi:10.1093/annonc/mds191. PMID: 23012298.

Duff D, Long A. Roles for RACK1 in cancer cell migration and invasion. Cell Signal. 2017 Jul;35:250-255. doi:10.1016/j.cellsig.2017.03.005. PMID: 28373075.

Emara HM, Allam NK, Youness RA. A comprehensive review on targeted therapies for triple negative breast cancer: an evidence-based treatment guideline. Discov Oncol. 2025 Apr 17;16(1):547. doi: 10.1007/s12672-025-02227-6. PMID: 40244488; PMCID: PMC12006628.

Espinoza-Sánchez NA, Chimal-Ramírez GK, Mantilla A, Fuentes-Pananá EM. IL-1β, IL-8, and matrix metalloproteinases-1, -2, and -10 are enriched upon monocyte-breast cancer cell cocultivation in a Matrigel-based three-dimensional system. Front Immunol. 2017 Feb 24;8:205. doi:10.3389/fimmu.2017.00205. PMID: 28286555.

Farhadi P, Yarani R, Valipour E, Kiani S, Hoseinkhani Z, Mansouri K. Cell line-directed breast cancer research based on glucose metabolism status. Biomed Pharmacother. 2022 Jan;145:112526. doi:10.1016/j.biopha.2021.112526. PMID: 34923213.

Gionfriddo G, Plastina P, Augimeri G, Catalano S, Giordano C, Barone I, Morelli C, Giordano F, Gelsomino L, Sisci D, Witkamp R, Andò S, van Norren K, Bonofiglio D. Modulating Tumour-Associated Macrophage Polarization by Synthetic and Natural PPARγ Ligands as a Potential Target in Breast Cancer. Cells. 2020 Jan 10;9(1):174. doi: 10.3390/cells9010174. PMID: 31936729; PMCID: PMC7017381.

Guido LP, Gomez-Fernandez C. Advances in the Molecular Taxonomy of Breast Cancer. Arch Med Res. 2020 Nov;51(8):777-783. doi: 10.1016/j.arcmed.2020.08.001. Epub 2020 Aug 21. PMID: 32839004.

Jiang H, Yun H, Wang X, Shen Z, Liu G, Zou T, Guo T, Wu M, Lu Y, Deng L, Miao J, Deng H, Yuan Z, Zhang J. RACK1 promotes the development and function of alveolar macrophages through directly binding to and stabilizing PPARγ. Proc Natl Acad Sci U S A. 2025 Jun 17;122(24):e2421672122. doi:10.1073/pnas.2421672122. PMID: 40490934.

Hao M, Huang B, Wu R, Peng Z, Luo KQ. The Interaction between Macrophages and Triple-negative Breast Cancer Cells Induces ROS-Mediated Interleukin 1α Expression to Enhance Tumourigenesis and Metastasis. Adv Sci (Weinh). 2023 Oct;10(29):e2302857. doi:

10.1002/advs.202302857. Epub 2023 Aug 8. PMID: 37551997; PMCID: PMC10582438.

Kim J, Harper A, McCormack V, Sung H, Houssami N, Morgan E, Mutebi M, Garvey G, Soerjomataram I, Fidler-Benaoudia MM. Global patterns and trends in breast cancer incidence and mortality across 185 countries. Nat Med. 2025 Apr;31(4):1154-1162. doi: 10.1038/s41591-025-03502-3. Epub 2025 Feb 24. PMID: 39994475.

Lee JS, Lero MW, Mercado-Matos J, Zhu S, Jo M, Tocheny CE, Morgan JS, Shaw LM. The insulin and IGF signaling pathway sustains breast cancer stem cells by IRS2/PI3K-mediated regulation of MYC. Cell Rep. 2022 Dec 6;41(10):111759. doi: 10.1016/j.celrep.2022.111759. PMID: 36476848; PMCID: PMC9793643.

Luck AA, Evans AJ, Green AR, Rakha EA, Paish C, Ellis IO. The influence of basal phenotype on the metastatic pattern of breast cancer. Clin Oncol (R Coll Radiol). 2008 Feb;20(1):40-5. doi: 10.1016/j.clon.2007.10.002. Epub 2007 Nov 5. PMID: 17981444.

Masi M, Garattini E, Bolis M, Di Marino D, Maraccani L, Morelli E, Grolla AA, Fagiani F, Corsini E, Travelli C, Govoni S, Racchi M, Buoso E. OXER1 and RACK1-associated pathway: a promising drug target for breast cancer progression. Oncogenesis. 2020 Dec 15;9(12):105. doi:10.1038/s41389-020-00291-x. PMID: 33319774.

Mazan A, Marusiak AA. Protocols for Co-Culture Phenotypic Assays with Breast Cancer Cells and THP-1-Derived Macrophages. J Mammary Gland Biol Neoplasia. 2024 Feb 10;29(1):4. doi: 10.1007/s10911-024-09556-2. PMID: 38340231; PMCID: PMC10858929.

Nascimento RG do, Otoni KM. Histological and molecular classification of breast cancer: what do we know? Mastology. 2020;30:1-8. doi:10.29289/25945394202020200024. PMID: 34078974.

Neasta J, Fiorenza A, He DY, Phamluong K, Kiely PA, Ron D. Activation of the cAMP pathway induces RACK1-dependent binding of β-actin to BDNF promoter. PLoS One. 2016 Aug 11;11(8):e0160948. doi:10.1371/journal.pone.0160948. PMID: 27509068.

Nedeljković M, Damjanović A. Mechanisms of Chemotherapy Resistance in Triple-Negative Breast Cancer-How We Can Rise to the Challenge. Cells. 2019 Aug 22;8(9):957. doi: 10.3390/cells8090957. PMID: 31443516; PMCID: PMC6770896.

Obeagu EI, Obeagu GU. Breast cancer: A review of risk factors and diagnosis. Medicine (Baltimore). 2024 Jan 19;103(3):e36905. doi: 10.1097/MD.0000000000036905. PMID: 38241592; PMCID: PMC10798762.

Padzińska-Pruszyńska I, Kucharzewska P, Matejuk A, Górczak M, Kubiak M, Taciak B, Król M. Macrophages: key players in the battle against triple-negative breast cancer. Int J Mol Sci. 2024 Oct 8;25(19):10781. doi:10.3390/ijms251910781. PMID: 39408774.

Pe KCS, Saetung R, Yodsurang V, Chaotham C, Suppipat K, Chanvorachote P, Tawinwung S. Triple-negative breast cancer influences a mixed M1/M2 macrophage phenotype associated with tumour aggressiveness. PLoS One. 2022 Aug 12;17(8):e0273044. doi: 10.1371/journal.pone.0273044. PMID: 35960749; PMCID: PMC9374254.

Pinilla K, Drewett LM, Lucey R, Abraham JE. Precision Breast Cancer Medicine: Early Stage Triple Negative Breast Cancer-A Review of Molecular Characterisation, Therapeutic Targets and Future Trends. Front Oncol. 2022 Aug 8;12:866889. doi: 10.3389/fonc.2022.866889. PMID: 36003779; PMCID: PMC9393396.

Qian BZ, Li J, Zhang H, Kitamura T, Zhang J, Campion LR, Kaiser EA, Snyder LA, Pollard JW. CCL2 recruits inflammatory monocytes to facilitate breast-tumour metastasis. Nature. 2011 Jun 8;475(7355):222-5. doi: 10.1038/nature10138. PMID: 21654748; PMCID: PMC3208506.

Racchi M, Buoso E, Ronfani M, Serafini MM, Galasso M, Lanni C, Corsini E. Role of Hormones in the Regulation of RACK1 Expression as a Signaling Checkpoint in Immunosenescence. Int J Mol Sci. 2017 Jul 6;18(7):1453. doi: 10.3390/ijms18071453. PMID: 28684670; PMCID: PMC5535944.

Sarvari P, Sarvari P, Ramírez-Díaz I, Mahjoubi F, Rubio K. Advances of Epigenetic Biomarkers and Epigenome Editing for Early Diagnosis in Breast Cancer. Int J Mol Sci. 2022 Aug 23;23(17):9521. doi: 10.3390/ijms23179521. PMID: 36076918; PMCID: PMC9455804.

Schimek V, Strasser K, Beer A, Göber S, Walterskirchen N, Brostjan C, Müller C, Bachleitner-Hofmann T, Bergmann M, Dolznig H, Oehler R. Tumour cell apoptosis modulates the colorectal cancer immune microenvironment via interleukin-8-dependent neutrophil recruitment. Cell Death Dis. 2022 Feb 4;13(2):113. doi: 10.1038/s41419-022-04585-3. PMID: 35121727; PMCID: PMC8816934.

Seyfoori A, Liu K, Caruncho HJ, Walter PB, Akbari M. Tumouroid-On-a-Plate (ToP): Physiologically Relevant Cancer Model Generation and Therapeutic Screening. Adv Healthc Mater. 2025 Jan;14(1):e2402060. doi: 10.1002/adhm.202402060. Epub 2024 Nov 13. PMID: 39538973; PMCID: PMC11694087.

Steenbrugge J, Breyne K, Demeyere K, De Wever O, Sanders NN, Van Den Broeck W, Colpaert C, Vermeulen P, Van Laere S, Meyer E. Anti-inflammatory signaling by mammary tumour cells mediates prometastatic macrophage polarization in an innovative intraductal mouse model for

triple-negative breast cancer. J Exp Clin Cancer Res. 2018 Aug 15;37(1):191. doi: 10.1186/s13046-018-0860-x. PMID: 30111338; PMCID: PMC6094904.

Stewart DA, Yang Y, Makowski L, Troester MA. Basal-like breast cancer cells induce phenotypic and genomic changes in macrophages. Mol Cancer Res. 2012 Jun;10(6):727-38. doi: 10.1158/1541-7786.MCR-11-0604. Epub 2012 Apr 24. PMID: 22532586; PMCID: PMC3640417.

Taherian-Fard A, Srihari S, Ragan MA. Breast cancer classification: linking molecular mechanisms to disease prognosis. Brief Bioinform. 2015 May;16(3):461-74. doi: 10.1093/bib/bbu020. Epub 2014 Jun 20. PMID: 24950687.

Teichgraeber DC, Guirguis MS, Whitman GJ. Breast Cancer Staging: Updates in the AJCC Cancer Staging Manual, 8th Edition, and Current Challenges for Radiologists, From the AJR Special Series on Cancer Staging. AJR Am J Roentgenol. 2021 Aug;217(2):278-290. doi: 10.2214/AJR.20.25223. Epub 2021 Feb 17. PMID: 33594908.

Tian R, Tian J, Zuo X, Ren S, Zhang H, Liu H, Wang Z, Cui Y, Niu R, Zhang F. RACK1 facilitates breast cancer progression by competitively inhibiting the binding of β-catenin to PSMD2 and enhancing the stability of β-catenin. Cell Death Dis. 2023 Oct 18;14(10):685. doi:10.1038/s41419-023-06191-3. PMID: 37848631.

Ullah, H., Ahsan, N., & Dakshanamurthy, S. (2021). Scaffold protein RACK1 inhibitor compounds prevent the focal adhesion kinase mediated breast cancer cell migration and invasion potential. bioRxiv. https://doi.org/10.1101/2021.06.13.448244

Urra FA, Muñoz F, Córdova-Delgado M, Ramírez MP, Peña-Ahumada B, Rios M, Cruz P, Ahumada-Castro U, Bustos G, Silva-Pavez E, Pulgar R, Morales D, Varela D, Millas-Vargas JP, Retamal E, Ramírez-Rodríguez

O, Pessoa-Mahana H, Pavani M, Ferreira J, Cárdenas C, Araya-Maturana R. FR58P1a; a new uncoupler of OXPHOS that inhibits migration in triple-negative breast cancer cells via Sirt1/AMPK/β1-integrin pathway. Sci Rep. 2018 Sep 4;8(1):13190. doi: 10.1038/s41598-018-31367-9. PMID: 30181620; PMCID: PMC6123471.

Valeta-Magara A, Gadi A, Volta V, Walters B, Arju R, Giashuddin S, Zhong H, Schneider RJ. Inflammatory Breast Cancer Promotes Development of M2 Tumour-Associated Macrophages and Cancer Mesenchymal Cells through a Complex Chemokine Network. Cancer Res. 2019 Jul 1;79(13):3360-3371. doi: 10.1158/0008-5472.CAN-17-2158. Epub 2019 May 1. PMID: 31043378; PMCID: PMC7331114.

Wang YH, Shen CY, Lin SC, Kuo WH, Kuo YT, Hsu YL, Wang WC, Lin KT, Wang LH. Monocytes secrete CXCL7 to promote breast cancer progression. Cell Death Dis. 2021 Nov 17;12(12):1090. doi: 10.1038/s41419-021-04231-4. PMID: 34789744; PMCID: PMC8599470.

Wang Q, Jiang S, Wu Y, Zhang Y, Huang M, Qiu Y, Luo X. Prognostic and clinicopathological role of RACK1 for cancer patients: a systematic review and meta-analysis. PeerJ. 2023 Nov 21;11:e15873. doi:10.7717/peerj.15873. PMID: 37981572.

Ward R, Sims AH, Lee A, Lo C, Wynne L, Yusuf H, Gregson H, Lisanti MP, Sotgia F, Landberg G, Lamb R. Monocytes and macrophages, implications for breast cancer migration and stem cell-like activity and treatment. Oncotarget. 2015 Jun 10;6(16):14687-99. doi: 10.18632/oncotarget.4189. PMID: 26008983; PMCID: PMC4546497.

Westcott JM, Prechtl AM, Maine EA, Dang TT, Esparza MA, Sun H, Zhou Y, Xie Y, Pearson GW. An epigenetically distinct breast cancer cell subpopulation promotes collective invasion. J Clin Invest. 2015

May;125(5):1927-43. doi: 10.1172/JCI77767. Epub 2015 Apr 6. PMID: 25844900; PMCID: PMC4463195.

Xiao Y, Ma D, Zhao S, Suo C, Shi J, Xue MZ, Ruan M, Wang H, Zhao J, Li Q, Wang P, Shi L, Yang WT, Huang W, Hu X, Yu KD, Huang S, Bertucci F, Jiang YZ, Shao ZM; AME Breast Cancer Collaborative Group. Multi-Omics Profiling Reveals Distinct Microenvironment Characterization and Suggests Immune Escape Mechanisms of Triple-Negative Breast Cancer. Clin Cancer Res. 2019 Aug 15;25(16):5002-5014. doi: 10.1158/1078-0432.CCR-18-3524. Epub 2019 Mar 5. PMID: 30837276.

Xu B, Sun H, Song X, Liu Q, Jin W. Mapping the tumour microenvironment in TNBC and deep exploration for M1 macrophages-associated prognostic genes. Front Immunol. 2022 Jul 7;13:923481. doi:10.3389/fimmu.2022.923481. PMID: 35898012.

Yang, J.-C., Du, Y.-Y., Zuo, W.-Q., Yao, J.-Y., Ma, K., Liang, Y., Zhao, M.-G., & Li, Z.-M. (2026). RACK1: A multifunctional scaffold protein involved in signal transduction, ribosomal regulation, and cancer pathogenesis. Cellular Signalling, 144, 112519. https://doi.org/10.1016/j.cellsig.2026.112519

Yarwood SJ, Steele MR, Scotland G, Houslay MD, Bolger GB. The RACK1 signaling scaffold protein selectively interacts with the cAMP-specific phosphodiesterase PDE4D5 isoform. J Biol Chem. 1999 May 21;274(21):14909-17. doi: 10.1074/jbc.274.21.14909. Erratum in: J Biol Chem 2001 Mar 2;276(9):6879. PMID: 10329691.

Yin L, Duan JJ, Bian XW, Yu SC. Triple-negative breast cancer molecular subtyping and treatment progress. Breast Cancer Res. 2020 Jun 9;22(1):61. doi: 10.1186/s13058-020-01296-5. PMID: 32517735; PMCID: PMC7285581.

Zhang X, Zhang S, Han Y. FGF4 drives tumour progression in triple-negative breast cancer via IL6/STAT3-mediated macrophage M2 polarization and immune suppression. Cell Div. 2025 Jun 10;20:22. doi:10.1186/s13008-025-00164-y. PMID: 40487131.

Zhao S, Zuo WJ, Shao ZM, Jiang YZ. Molecular subtypes and precision treatment of triple-negative breast cancer. Ann Transl Med. 2020 Apr;8(7):499. doi: 10.21037/atm.2020.03.194. PMID: 32395543; PMCID: PMC7210152.

Zhu SY, Ma D, Shao ZM, Yu KD. Prognostic Effect of Microenvironment Phenotype in Triple-Negative Breast Cancer: Biomarker Analysis of a Prospective Trial. Front Mol Biosci. 2021 Sep 21;8: 752154. doi: 10.3389/fmolb.2021.752154. PMID: 34621789; PMCID: PMC8490613.